



*Supplement of*

## **Indicators of Global Climate Change 2025: annual update of key indicators of the state of the climate system and human influence**

**Piers M. Forster et al.**

*Correspondence to:* Piers M. Forster ([p.m.forster@leeds.ac.uk](mailto:p.m.forster@leeds.ac.uk))

The copyright of individual parts of the supplement might differ from the article licence.

## S1. Context

The IPCC Special Report on Global Warming of 1.5°C (SR1.5), published in 2018, provided an assessment of the level of human-induced warming and cumulative emissions to date (Allen et al., 2018) and the remaining carbon budget (Rogelj et al., 2018) to support the evidence base on how the world is progressing in terms of meeting aspects of the Paris Agreement. The AR6 WGI Report, published in 2021, assessed past, current and future changes of these and other key global climate indicators, as well as undertaking an assessment of the Earth’s energy budget. It also updated its approach for estimating the human-induced warming and global warming level. In AR6 WGI and here, reaching a level of global warming is defined as the global surface temperature change, averaged over a 20-year period, exceeding a particular level of global warming, e.g. 1.5°C global warming. Given the current rates of change and the likelihood of reaching 1.5°C of global warming in the first half of the 2030s (Lee J.-Y. et al., 2021; Lee et al., 2023; Riahi et al., 2022), it is important to have robust, trusted, and also timely climate indicators in the public domain to form an evidence base for effective science-based decision making.

## S2. Emissions

### S2.1 Influence of the assessment approach and system boundaries on anthropogenic GHG emissions

There are important differences in reporting conventions and system boundaries between assessments of total anthropogenic GHG emissions. These differences relate to the fact that emissions datasets vary in their coverage of sources and sectors; that there are different approaches to determining the “anthropogenic” component of LULUCF emissions and removals (particularly between bookkeeping and national inventory accounts); and that the Paris Agreement does not cover all relevant sources of emissions such as ozone depleting substances (ODS F-gases) and cement carbonation (Lamb et al., 2026). Table S1 documents the datasets used for three assessment approaches presented in the main text, with further underlying detail on these approaches described in Lamb et al. 2026.

Table S1 The three GHG emissions estimates and their underlying datasets.

<b>Estimate</b>	<b>Source</b>	<b>Datasets</b>	<b>Reference</b>
WGIII update	CO <sub>2</sub> -FFI and CO <sub>2</sub> -LULUCF	GCB v2025	Friedlingstein et al., 2025

	CH <sub>4</sub> , N <sub>2</sub> O, UNFCCC F-gases	EDGAR v2025	Crippa et al. 2025
WGIII update + additional sources	CO <sub>2</sub> -FFI, CO <sub>2</sub> -LULUCF, CH <sub>4</sub> , N <sub>2</sub> O and UNFCCC F-gases	As for WGIII update	Friedlingstein et al., 2025, Crippa et al. 2025
	Biomass fires (CH <sub>4</sub> and N <sub>2</sub> O)	GFED v5.1	van der Werf et al., 2025
	ODS F-gases	CIP v2025: Climate Indicators Project (this article), with underlying data from NOAA and AGAGE inversions (see Sect. 3 main manuscript)	Lan et al., 2025; Dutton et al., 2024; Prinn et al., 2018
	Cement carbonation	GCB v2025	Friedlingstein et al., 2025
Inventory aligned	CO <sub>2</sub> -FFI, CH <sub>4</sub> , N <sub>2</sub> O and UNFCCC F-gases	PRIMAP Hist-CR v2.7	Gütschow et al., 2025
	CO <sub>2</sub> -LULUCF	JRC-NGHGI v2024	Melo et al. 2025

## S2.2 Changes to CO<sub>2</sub>-LULUCF in the Global Carbon Budget (GCB) v2025

As in prior versions of the GCB, estimates of CO<sub>2</sub>-LULUCF are informed by bookkeeping models that track historical land use changes and apply empirical response curves to account for their impact on carbon stocks over time (Hansis et al. 2015). There were two substantial changes to the GCB in 2025. First, as part of a methodological update towards a consistent terrestrial carbon budget, it is now a precondition that each underlying bookkeeping model uses transient carbon densities, i.e., they consider the effects of environmental changes, such as atmospheric CO<sub>2</sub> increase and impacts of climate change, on vegetation and soil carbon densities (Gasser et al., 2020; Dorgeist et al., 2024). The inclusion of transient carbon densities increases gross fluxes for all gross CO<sub>2</sub>-LULUCF emission and removal terms. (For example, deforestation emissions are increased due to a larger standing biomass at the time of clearing because the transient effect of the rise in atmospheric CO<sub>2</sub> on plant growth is now considered in the CO<sub>2</sub>-LULUCF estimates.) For the net flux of CO<sub>2</sub>-LULUCF, this methodological change causes estimates to be slightly higher in the last three decades and the multi-decadal downward trend in net emissions

to be smaller. A second and related change is that while GCB v2024 was based on four bookkeeping models (BLUE, OSCAR, H&C2023, LUCE), GCB v2025 is based only on three, because H&C2023 does not consider transient carbon densities and it only provides data up to 2020. H&C2023 was thus no longer used. This change in model ensemble causes estimates of CO<sub>2</sub>-LULUCF emissions to be somewhat lower.

### S2.3 Calculation of uncertainties and CO<sub>2</sub> equivalent emissions in Section 2

We follow the same approach for estimating uncertainties and CO<sub>2</sub>-equivalent emissions as in AR6: CO<sub>2</sub>-equivalent emissions were calculated using global warming potentials with a 100-year time horizon (GWP100 henceforth) from AR6 WGI Chap. 7 (Forster et al., 2021). Uncertainty ranges were based on a comparative assessment of available data and expert judgment, corresponding to a 90 % confidence interval (Minx et al., 2021):  $\pm 8\%$  for CO<sub>2</sub>-FFI,  $\pm 70\%$  for CO<sub>2</sub>-LULUCF,  $\pm 30\%$  for CH<sub>4</sub> and F-gases, and  $\pm 60\%$  for N<sub>2</sub>O (note that the GCB assesses 1 standard deviation uncertainty for CO<sub>2</sub>-FFI as  $\pm 5\%$  and for CO<sub>2</sub>-LULUCF as  $\pm 2.6$  GtCO<sub>2</sub>; Friedlingstein et al., 2025). The total uncertainty was summed in quadrature, assuming independence of estimates per species/source. Reflecting these uncertainties, AR6 WGIII reported emissions to two significant figures only. Uncertainties in GWP100 metrics of roughly  $\pm 10\%$  were not applied (Minx et al., 2021).

### S3. Greenhouse gas concentrations

Naming conventions and details for Sect. 3 of the main paper and herein follow AR6 WGI Chapter 2 (Gulev et al., 2021).

**Table S2 Annual mean concentrations of well-mixed greenhouse gases in 2025, 2024, 2023, 2019, 1850 and 1750. Except for CO<sub>2</sub>, CH<sub>4</sub> and N<sub>2</sub>O, concentrations all are in parts per trillion by volume [ppt]. For halogenated gases, concentrations are stated for each gas, with equivalents for HFCs, PFCs and Montreal gases given as the radiative equivalent of the most abundant gas in each category.**

Greenhouse gas	1750	1850	2019	2023	2024	2025
CO <sub>2</sub> [ppm]	278.4	285.6	410.1	419.4	422.8	425.6
CH <sub>4</sub> [ppb]	729.2	807.6	1866.1	1921.2	1928.8	1936.3
N <sub>2</sub> O [ppb]	270.1	272.1	332.1	336.9	338.0	339.4
NF <sub>3</sub>	0.0	0.0	2.1	3.2	3.5	3.7
SF <sub>6</sub>	0.0	0.0	9.9	11.4	11.8	12.2
SO <sub>2</sub> F <sub>2</sub>	0.0	0.0	2.5	2.9	3.0	3.1
<b>HFCs as HFC-134a-eq</b>	<b>0.0</b>	<b>0.0</b>	<b>237.4</b>	<b>303.5</b>	<b>321.4</b>	<b>338.2</b>

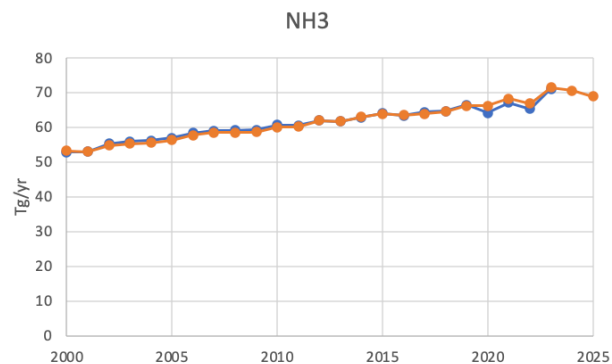
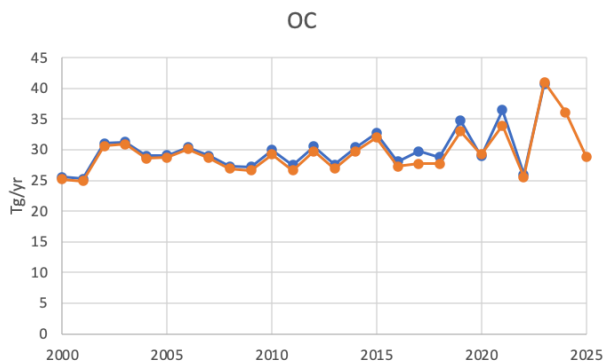
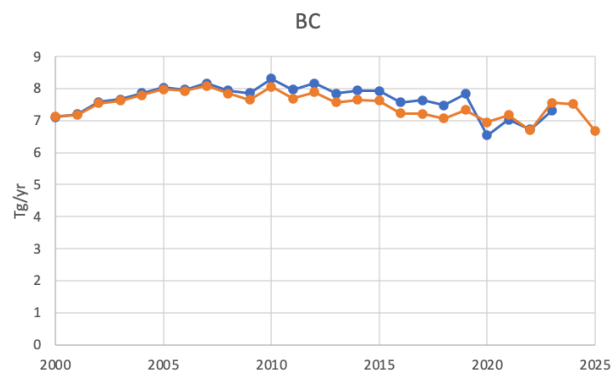
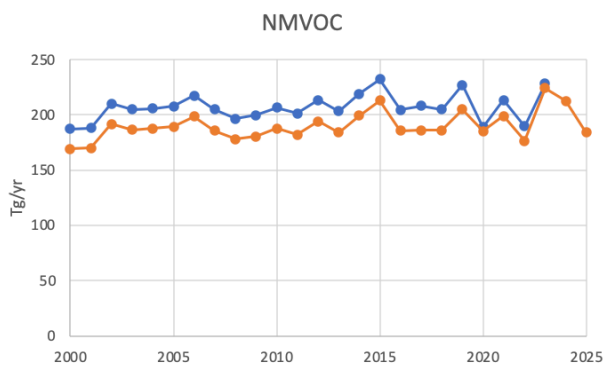
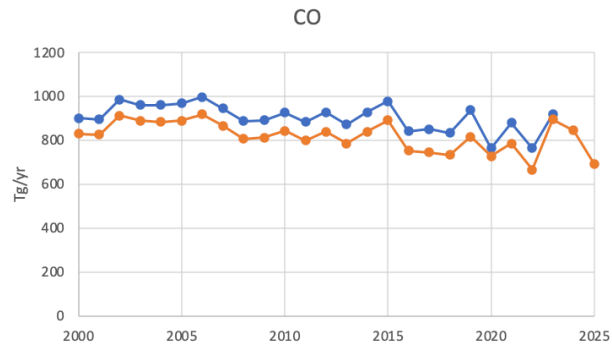
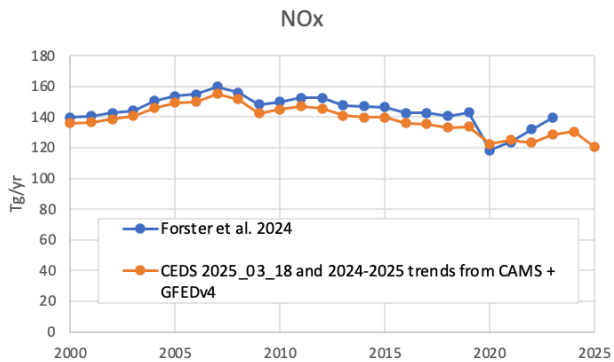
HFC-134a	0.0	0.0	107.6	129.5	134.7	140.3
HFC-23	0.0	0.0	32.8	37.0	37.8	38.9
HFC-32	0.0	0.0	19.4	33.9	38.7	42.3
HFC-125	0.0	0.0	29.6	44.2	48.6	52.3
HFC-143a	0.0	0.0	24.0	30.9	32.7	34.5
HFC-152a	0.0	0.0	7.1	7.4	7.7	7.8
HFC-227ea	0.0	0.0	1.6	2.3	2.5	2.6
HFC-236fa	0.0	0.0	0.2	0.2	0.3	0.3
HFC-245fa	0.0	0.0	3.1	3.7	3.8	3.9
HFC-365mfc	0.0	0.0	1.1	1.1	1.1	1.1
HFC-43-10mee	0.0	0.0	0.3	0.3	0.3	0.3
<b>PFCs as CF<sub>4</sub>-eq</b>	<b>34.1</b>	<b>34.1</b>	<b>109.7</b>	<b>115.8</b>	<b>117.3</b>	<b>118.9</b>
CF <sub>4</sub>	34.0	34.0	85.5	89.4	90.4	91.3
C <sub>2</sub> F <sub>6</sub>	0.0	0.0	4.8	5.2	5.3	5.4
C <sub>3</sub> F <sub>8</sub>	0.0	0.0	0.7	0.8	0.8	0.8
c-C <sub>4</sub> F <sub>8</sub>	0.0	0.0	1.8	2.0	2.1	2.1
n-C <sub>4</sub> F <sub>10</sub>	0.0	0.0	0.2	0.2	0.2	0.2
n-C <sub>5</sub> F <sub>12</sub>	0.0	0.0	0.1	0.2	0.2	0.2
n-C <sub>6</sub> F <sub>14</sub>	0.0	0.0	0.2	0.2	0.2	0.2
i-C <sub>6</sub> F <sub>14</sub>	0.0	0.0	0.1	0.1	0.1	0.1
C <sub>7</sub> F <sub>16</sub>	0.0	0.0	0.1	0.1	0.1	0.1
C <sub>8</sub> F <sub>18</sub>	0.0	0.0	0.1	0.1	0.1	0.1
<b>Montreal gases as CFC-12-eq</b>	<b>8.5</b>	<b>8.5</b>	<b>1031.8</b>	<b>1004.0</b>	<b>995.6</b>	<b>988.9</b>
CFC-12	0.0	0.0	503.0	487.3	483.1	479.4
CFC-11	0.0	0.0	226.2	216.8	214.4	212.1

CFC-113	0.0	0.0	69.8	67.2	66.6	66.0
CFC-114	0.0	0.0	16.0	16.0	16.0	16.0
CFC-115	0.0	0.0	8.7	8.9	8.9	9.0
CFC-13	0.0	0.0	3.3	3.4	3.4	3.4
CFC-112	0.0	0.0	0.4	0.4	0.4	0.4
CFC-112a	0.0	0.0	0.1	0.1	0.1	0.1
CFC-113a	0.0	0.0	0.9	1.3	1.4	1.5
CFC-114a	0.0	0.0	1.0	1.0	1.0	1.0
HCFC-22	0.0	0.0	246.7	247.2	245.2	245.5
HCFC-141b	0.0	0.0	24.4	24.5	24.4	24.4
HCFC-142b	0.0	0.0	22.2	21.2	21.0	20.7
HCFC-133a	0.0	0.0	0.4	0.4	0.4	0.4
HCFC-31	0.0	0.0	0.1	0.1	0.1	0.1
HCFC-124	0.0	0.0	1.0	0.9	0.9	0.9
CH3CCI3	0.0	0.0	1.6	1.0	0.9	0.7
CCI4	0.0	0.0	78.0	73.9	73.0	72.0
CH3Cl	457.0	457.0	541.4	536.5	544.1	538.9
CH3Br	5.3	5.3	6.5	6.4	6.5	6.4
CH2Cl2	6.9	6.9	40.6	45.3	48.9	49.9
CHCl3	4.8	4.8	8.8	7.6	7.8	7.5
Halon-1211	0.0	0.0	3.3	2.9	2.8	2.7
Halon-1301	0.0	0.0	3.3	3.3	3.3	3.3
Halon-2402	0.0	0.0	0.4	0.4	0.4	0.4

#### S4. Short-Lived Climate Forcers (SLCFs)

**Table S3 Emissions of the major SLCFs in 1750, 2019, 2022, 2023, 2024 and 2025 from a combination of CEDS and GFED and CAMS for the 2024-2025 trend. Provisional estimates used in Forster et al. (2023) and Forster et al. (2024) are shown. Emissions of SO<sub>2</sub>+SO<sub>4</sub> use SO<sub>2</sub> molecular weights. Emissions of NO<sub>x</sub> use NO<sub>2</sub> molecular weights. VOCs are for the total mass.**

Compound	1750	2019 (WGI)	2019 (updated with CEDS v 2025_03-18 and GFEDv4)	2022 (Forster et al., 2023)	2022 (updated with CEDS v 2025_03-18 and GFEDv4)	2023 (Forster et al., 2024)	2023 (updated with CEDS v 2025_03-18 and GFEDv4)	2024 (CEDS v 2025_03-18 and GFEDv4)	2025 (CEDS v 2025_03-18 and GFEDv4)
Sulphur dioxide (SO <sub>2</sub> ) + sulphate (SO <sub>4</sub> <sup>2-</sup> )	2.8	84.2	80.9	75.3	70.6	79.1	72.7	71.2	69.1
Black carbon (BC)	2.1	7.5	7.3	6.8	6.7	7.3	7.6	7.5	6.7
Organic carbon (OC)	15.5	34.2	33.0	25.8	25.6	40.7	41.0	36.1	28.9
Ammonia (NH <sub>3</sub> )	6.6	67.6	66.3	67.3	66.8	71.1	72.7	70.6	68.9
Oxides of nitrogen (NO <sub>x</sub> )	19.4	141.7	133.6	130.4	123.2	139.4	128.4	130.4	120.4
Volatile organic compounds (VOCs)	60.9	217.3	204.8	183.9	176.4	228.1	224.1	212.7	184
Carbon monoxide (CO)	348.4	853.8	816.1	686.4	665.4	917.5	896.0	845.3	693.2



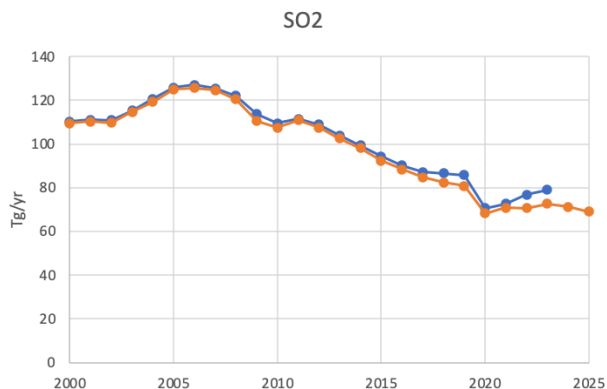


**Figure S1 Comparison of short-lived climate forcer emissions from Forster et al. (2024) (blue) and the most recent update of CEDS and GFED through 2023, with 2024-2025 trend from CAMS (orange). (Granier et al., 2019; Jalkanen et al. 2012, 2016; Johansson et al., 2017).**

## S5. Effective radiative forcing (ERF)

### S5.1 Well-mixed greenhouse gas ERF methods

Radiative forcing (RF) from CO<sub>2</sub>, CH<sub>4</sub>, and N<sub>2</sub>O use the simplified formulas from concentrations in Meinshausen et al. (2020), derived from an updated functional fit to Etminan et al. (2016) line-by-line radiative transfer results. These formulas are, to first order, logarithmic with CO<sub>2</sub> concentrations and a square-root dependence for CH<sub>4</sub> and N<sub>2</sub>O, with additional corrections and radiative band overlaps between gases. RF is converted to ERF using scaling factors (1.05, 0.86 and 1.07 for CO<sub>2</sub>, CH<sub>4</sub>, N<sub>2</sub>O respectively) that account for tropospheric and land-surface rapid adjustments (Smith et al., 2018a; Hodnebrog et al., 2020a). ERF from other GHGs is assumed to scale linearly with their concentration based on their radiative efficiencies expressed in W m<sup>-2</sup> ppb<sup>-1</sup> (Hodnebrog et al., 2020b, Smith et al., 2021b). A scaling factor translating RF to ERF is implemented for CFC-11 (1.13) and CFC-12 (1.12) (Hodnebrog et al., 2020a), whereas no model evidence exists to treat ERF differently to RF for other halogenated gases.

Relative uncertainties in the ERF for CO<sub>2</sub> (± 12%), CH<sub>4</sub> (± 20%) and N<sub>2</sub>O (± 14%) are unchanged from AR6. These stem from a combination of spectroscopic uncertainties and uncertainties in the adjustment terms converting RF to ERF; uncertainties in the volume mixing concentrations themselves are assessed to be small (Sect. 2). Uncertainties in the ERF

from halogenated gases are treated individually and are assessed as  $\pm 19\%$  for gases with a lifetime of 5 or more years and  $\pm 26\%$  for shorter lifetime gases. In AR6, a  $\pm 19\%$  uncertainty was applied to the sum of the ERF from all halogenated gases. To maintain a consistent uncertainty range across the sum of ERF from halogenated gases with AR6, we inflate the uncertainty in each individual gas by a factor of 2.05. Uncertainties are applied by scaling the full ERF time series for each gas.

## **S5.2 Aerosol ERF methods**

Aerosol ERF is a combination of contributions from aerosol-radiation interactions (ERFari) and aerosol-cloud interactions (ERFaci).

### **S5.2.1 Aerosol-radiation interactions**

Contributions to ERFari are assumed to scale linearly with certain SLCF emissions in Sect. 3 ( $\text{SO}_2$ , BC, OC,  $\text{NH}_3$ ,  $\text{NO}_x$  and VOC) or concentrations ( $\text{CH}_4$ ,  $\text{N}_2\text{O}$  and ozone-depleting halocarbons) of primary aerosols and chemically active precursor species. The coefficients converting emissions or concentrations of each SLCF into ERF and its uncertainty come from Chapter 6 of AR6 WGI (Szopa et al., 2021), originally from CMIP6 AerChemMIP models (Thornhill et al., 2021a). We scale these coefficients to reproduce the headline AR6 WGI ERFari assessment of  $-0.3 \text{ W m}^{-2}$  from 1750 to 2005-2014. Uncertainties are applied as a scale factor for each species and applied to the whole time series.

The inclusion of more species that affect ERFari differs from the AR6 WGI calculation of ERFari in Chapter 7, which only used  $\text{SO}_2$ , BC, OC and  $\text{NH}_3$  (Smith et al., 2021b). In the update, these four species remain the dominant aerosol and aerosol precursors. Additionally, these coefficients have changed slightly due to switching to CMIP6 era data. In AR6, the coefficients scaling emissions to ERF for  $\text{SO}_2$ , BC, OC and  $\text{NH}_3$  were provided by CMIP5-era models (Myhre et al., 2013a). The additional coefficients and slight changes to their magnitude had an imperceptible effect on the results but have been included to align with current best practice. This might be important in future years as  $\text{NO}_x$  and VOC precursors might make up a larger fraction of ERFari.

### **S5.2.2 Aerosol-cloud interactions**

ERFaci is estimated by assuming a logarithmic relationship with the change in cloud droplet number concentration (CDNC) as

$$\text{ERFaci} = \beta \log (1 + \Delta\text{CDNC}) \quad (\text{S1})$$

$$\Delta\text{CDNC} = s_{\text{SO}_2}\Delta E_{\text{SO}_2} + s_{\text{BC}}\Delta E_{\text{BC}} + s_{\text{OC}}\Delta E_{\text{OC}} \quad (\text{S2})$$

where  $s_{\text{SO}_2}$ ,  $s_{\text{BC}}$  and  $s_{\text{OC}}$  are sensitivities of the change in CDNC with the change in emissions of  $\text{SO}_2$ , BC and OC respectively ( $\Delta E$ ). This relationship is fit to estimates of ERFaci in 13 CMIP6 models contributing results to the piClim-histaer and histSST-piAer experiments of RFMIP and AerChemMIP, respectively, to CMIP6 (Smith et al., 2024). The ERFaci in these 13 models is estimated using the Approximate Partial Radiative Perturbation (APRP) method (Taylor et al., 2007; Zelinka et al., 2014; Zelinka et al., 2023).

The  $s_{\text{SO}_2}$ ,  $s_{\text{BC}}$  and  $s_{\text{OC}}$  values from each model are combined into a kernel density estimate and sampled 100,000 times to provide a CMIP6-informed distribution of these parameters. To obtain  $\beta$  for each sample given ( $s_{\text{SO}_2}$ ,  $s_{\text{BC}}$ ,  $s_{\text{OC}}$ ) a target ERFaci value for 1750 to 2005-2014 is drawn from the headline AR6 distribution of -1.0 [-1.7 to -0.3]  $\text{W m}^{-2}$  and eq. (S1) rearranged. This follows a very similar procedure to AR6 and is based on Smith et al. (2021a) with three updates. Firstly, the relationships in eqs. (S1) and (S2) are slightly updated and simplified (Smith et al., 2024). Secondly, an additional two CMIP6 models have become available since the AR6 WG1 assessment which expands the sampling pool for coefficients from 11 to 13. Thirdly, a slight error in computing ERFaci from APRP from the CMIP6 models in Smith et al. (2021a) has been corrected (Zelinka et al., 2023).

### S5.3 Ozone ERF methods

In AR6 WGI Chapter 7, the ozone ERF is derived from CMIP6 model-based estimates (Skeie et al., 2020) from 1850 to 2014, to infer the sensitivity of ozone RF to emissions of  $\text{NO}_x$ , VOC and CO, concentrations of  $\text{CH}_4$ ,  $\text{N}_2\text{O}$  and ozone-depleting halogens, and global mean surface temperature (GMST) anomaly. These factors can be found in Table 7.SM.3 of AR6. In CMIP6, experimental results that vary CO and VOC emissions separately are not available, so individual contributions from CO and VOC to the CO+VOC total are based on their fractional contributions from ACCMIP (CMIP5-era) models in Stevenson et al. (2013). To compute the ozone ERF we thus use the radiative efficiencies for ozone ERF and the scale factor to  $\text{CH}_4$ ,  $\text{N}_2\text{O}$  and ozone-depleting halogens concentration changes discussed in the paper and CO, NMVOC and  $\text{NO}_x$  emission changes discussed in the paper. For the global mean temperature contribution to ozone forcing (in terms of  $\text{W m}^{-2} \text{K}^{-1}$ ), we use the model responses to ozone forcing per degree warming in chemistry-enabled models in

abrupt-4xCO<sub>2</sub> experiments (Thornhill et al., 2021b), and apply this factor to the observed GMST anomaly from Sect. 7. Following AR6, we do not differentiate between stratospheric and tropospheric ozone, and we also assume that ERF is the same as RF as there is limited model evidence to suggest otherwise.

#### **S5.4 ERF from land use change and irrigation**

In Forster et al., (2024), ERF from land use and irrigation was scaled with cumulative CO<sub>2</sub> emissions from AFOLU from 1750, as the IPCC AR6 assessment from Ghimire et al. (2014) did not extend beyond 2005, and the IPCC assessment used cumulative AFOLU CO<sub>2</sub> emissions to estimate land use and irrigation ERF from 2005 to 2019. In Forster et al.(2025) onwards, we use land use transitions from the Land Use Harmonization v2 (LUH2) dataset (Hurtt et al., 2020) updated for the Global Carbon Budget (GCB) 2024 (Chini et al., 2021; Friedlingstein et al., 2025) using cropland and grazing land data from HYDE3.4 (Klein Goldewijk et al., 2017) that itself merges the latest FAO state-level data with MapBiomas satellite-based estimates for Brazil and Indonesia (Souza et al., 2020) and another recent estimate for China (Yu et al., 2022). This constitutes an update to the Ghimire et al. (2014) data that used LUH1, using the satellite-derived albedo-related parameters of Ouyang et al. (2022) and providing data for 1750-2023, which we extrapolate one year to 2024. The resulting global ERF is scaled by a factor of 1.28 to recover the Ghimire et al. (2014) surface reflectance assessment of -0.15 W m<sup>-2</sup> in 2005 relative to 1750 to ensure consistency with the AR6. For irrigation, we assume the forcing scales with the area of land irrigated. We create a timeseries of this irrigated land area, using FAOSTAT (FAO, 2024) from 1961-2022, and Angelakis et al. (2021) to extend back to 1750. Angelakis et al. (2021) provide data points from 1900 in their Figure 21, and give a value for 1800 in the text. We assume the 1800 value (8 megahectares as compared to 354 megahectares in 2022) applies to 1750 and apply a cubic spline fit to produce a time series of irrigated area from 1750 to 1961 which is scaled to match the 1961 FAOSTAT irrigated area. The irrigated area in 2019 is assumed to result in the AR6 assessment of irrigation forcing of -0.05 W m<sup>-2</sup> in 2019 (having its roots in Sherwood et al., 2018), and irrigation forcing is linear with irrigated area relative to this benchmark. We note that since the publication of AR6, more Earth System models incorporating transient historical irrigation are available (Yao et al., 2025), and could be used to provide an assessment of the ERF of irrigation in future.

#### **S5.5 ERF from other anthropogenic forcers**

Minor categories of anthropogenic forcers include contributions from land use and land use change other than via GHG emissions, aviation contrails and contrail-induced cirrus, stratospheric water vapour from methane oxidation, and light absorbing particles on snow and ice.

The methodology to estimate ERF from land use and land-use change, including irrigation, has been updated to be more consistent with AR6 (Sect. 5). We anchor the 1750-2019 assessment to be the same as AR6 at  $-0.15$  [ $-0.25$  to  $-0.05$ ]  $\text{W m}^{-2}$  for the ERF from surface albedo changes and  $-0.05$  [ $-0.10$  to  $+0.05$ ]  $\text{W m}^{-2}$  for irrigation under this updated methodology. Stratospheric water vapour from methane oxidation was assessed to be  $0.05$  [ $0.00$  to  $0.10$ ]  $\text{W m}^{-2}$  in AR6 for 1750-2019, and is assumed to change linearly with changes in methane concentration.

The ERF from light absorbing particles on snow and ice (LAPSI) is assumed to scale with emissions of black carbon. As in AR6, the contribution from brown carbon is assumed to be negligible. We align the coefficient that converts BC emissions to ERF from LAPSI to match the  $0.08$  [ $0.00$  to  $0.18$ ]  $\text{W m}^{-2}$  assessment in AR6 for 1750-2019.

To estimate ERF from aviation contrails and contrail-induced cirrus in AR6, emissions of  $\text{NO}_x$  from the aviation sector in CEDS were scaled to reproduce an ERF of  $0.0574$  [ $0.019$  to  $0.098$ ]  $\text{W m}^{-2}$  for 1750-2018 as assessed in Lee D. S. et al. (2021). We more closely follow the original methods of Lee D. S. et al. (2021) in this update to base our ERF estimates as closely as possible on aviation activity data. The Lee D.S. et al. (2021) ERF time series is extended to 2022 based on aviation fuel consumption from the International Energy Agency's (IEA) World Oil Statistics (2024). For 2023 and 2024, we use fuel consumption data from the International Air Transport Association (IATA, 2024).

## **S5.6 Methods for estimating natural forcing**

Natural forcing is composed of solar irradiance and volcanic eruptions.

### **S5.6.1 Solar irradiance**

The method to compute solar forcing is unchanged from AR6, using a composite time series prepared for PMIP4 (Jungclaus et al., 2017) and CMIP6 (Matthes et al., 2017). The headline assessment of solar ERF is based on the most recent solar cycle (2009-2019), which is unchanged from AR6. Solar ERF estimates are computed relative to complete solar cycles encompassing the full “pre-industrial” period where proxy data exists (6754 BCE to 1745 CE). The CMIP7 solar forcing time series for the historical period (1850–2023) is now available (Funke et al., 2024). However, it has changed from the CMIP6 time series and does not seamlessly transition to the pre-1850 period including the last several thousand years, nor does it extend forward to include 2024. In future editions of IGCC, the CMIP7 solar forcing product could be used if the data spans the appropriate periods.

## S5.6.2 Volcanic

Volcanic ERF consists of contributions from stratospheric sulphate aerosol optical depth (sAOD; a negative forcing) and stratospheric water vapour (sWV, a positive forcing). The sAOD time series (at a nominal wavelength of 550 nm) is constructed from a combination of four datasets which have temporal overlap. We use ice-core deposition data from HolVol v1.0 (Sigl et al., 2022) for 9500 BCE to 1749 CE. For 1750 to 2023 we use the CMIP7 volcanic sAOD dataset (Durack et al., 2025) using the 550 nm spectral band, which is an update from IGCC 2023 that used the CMIP6 volcanic sAOD dataset. There is a seamless transition between HolVol and CMIP7 in 1750, so no blending of datasets was required. In previous editions of IGCC, we used the Global Space-based Stratospheric Aerosol Climatology (GloSSAC) product of sAOD which provided data until the penultimate year (Thomason et al., 2018), however, with the availability of the CMIP7 dataset to 2023, GloSSAC is not required directly in this year's IGCC. Additionally, the CMIP7 dataset incorporates GloSSAC from 1979 to 2023. For 2024, we use the Ozone Mapping and Profiling Limb Profiler (OMPS LP) Level 3 aerosol optical depth at 745 nm, which is scaled to achieve the same time mean sAOD as GloSSAC v2.22 (Kovilakam et al., 2020) in the overlapping 2013-2023 period as a single Ångstrom exponent is not suggested for this conversion. The 745 nm band from OMPS-LP is used as this is reported to be more stable than the bands closer to 550 nm from OMPS LP (Taha et al., 2021). For comparison we estimate the 550 nm sAOD from GloSSAC v2.22 using the 525 nm band and an Ångstrom exponent of -2.33, and we find good correspondence to the CMIP7 sAOD time series for the 1979-2023 common period. Therefore, while GloSSAC is not used directly this year, it is used as an anchor and reference for both the CMIP7 and OMPS-LP datasets. sAOD is converted to a radiative effect using a scaling factor of  $-20 \pm 5$  as in AR6 (Smith et al., 2021b) that is representative of CMIP5 and CMIP6 models. ERF is calculated with reference to the change in this radiative effect since “pre-industrial”, defined as the mean of all available years before 1750 CE. In other words, the mean of the pre-1750 period is defined as zero forcing.

The January 2022 eruption of Hunga Tonga-Hunga Ha'apai (HTHH) was an exceptional episode in that it emitted large amounts of water vapour into the stratosphere (Millán et al., 2022; Sellitto et al., 2022). Jenkins et al. (2023) determined the HTHH eruption increased volcanic ERF in 2022 by  $+0.12 \text{ W m}^{-2}$  due to sWV. In IGCC 2024 we update this value from Jenkins et al. (2023), which used an idealised injection of water vapour, to use direct satellite retrievals of water vapour from the Microwave Limb Sounder (MLS) data on board the Aura platform. Using the MLS data in place of the Jenkins et al. (2023) spatial distribution, we update the 2022 volcanic sWV ERF to  $+0.14 \text{ W m}^{-2}$ , and find that in the MLS data the stratospheric water vapour plume persists into 2023 ( $+0.18 \text{ W m}^{-2}$ ) and 2024 ( $+0.15 \text{ W m}^{-2}$ ) (Fig. S2). These water vapour forcings are calculated in a similar fashion to in Jenkins et al. (2023), by implementing the stratospheric water vapour in

2022, 2023 and 2024 from MLS against a climatology derived from MLS using the 2004-2021 years. The instantaneous radiative forcing at the tropopause is calculated using the SOCRATES radiative transfer model (Edwards and Slingo, 1996), against a background climatology (atmospheric temperatures, humidity, cloud profiles, ozone profiles, surface albedo and surface temperature) taken from ECMWF ERA5 reanalysis (Hersbach et al., 2020). From the CMIP7 and GloSSAC data the peak addition of stratospheric aerosols was around 0.007 optical depth units in the global mean, resulting in a peak volcanic aerosol forcing of  $-0.14 \text{ W m}^{-2}$  in mid-2022 relative to the pre-HTHH baseline that decayed away with an e-folding lifetime of around 18 months. We conclude using this analysis that the net HTHH ERF from both sAOD and sWV was positive (but small) in 2022, 2023 and 2024, and attempting to back out HTHH from other small eruptions gives a best estimate ERF for HTHH in isolation of  $+0.03 \text{ W m}^{-2}$  in 2022,  $+0.10 \text{ W m}^{-2}$  in 2023 and  $+0.10 \text{ W m}^{-2}$  in 2024. This is in contrast to other studies that assess a net negative (Gupta et al., 2025) or zero (Schoeberl et al., 2024) impact of HTHH, using different methods.

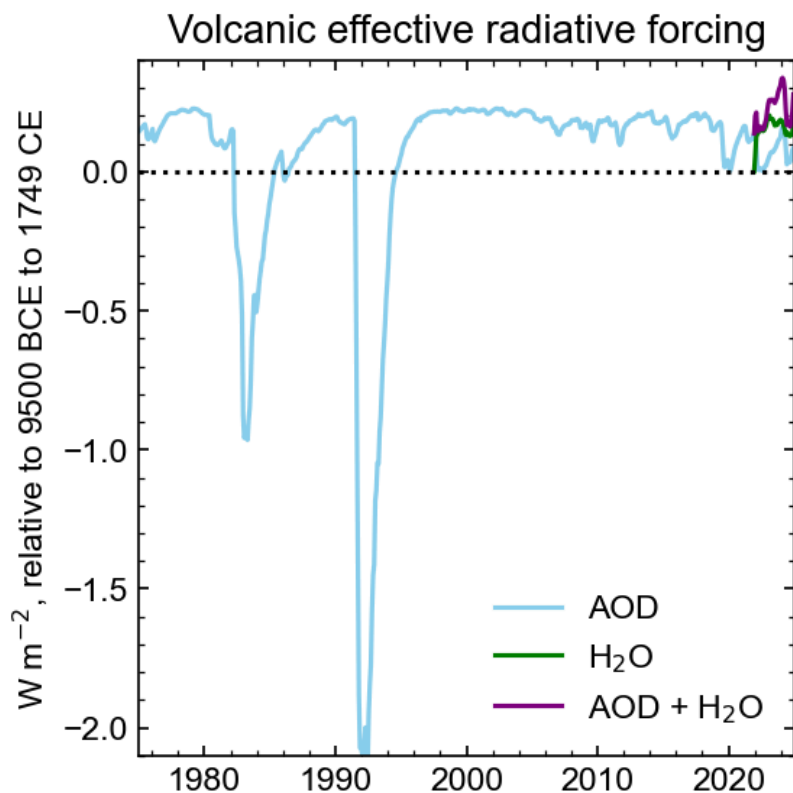


**Figure S2 Volcanic effective radiative forcing from 1975 to present relative to the pre-1750 baseline. The impact of including stratospheric water vapour from Hunga Tonga-Hunga Ha’apai (green) can be observed in 2022, 2023 and 2024 by increasing the net volcanic ERF above the background level (purple).**

Following the approach of Shine et al. (1990, see their Figure 2.3), we display (Fig. S3) the decadal contributions to radiative forcing (computed as the difference from decade to decade of the decadal mean ERF, per species, in Wm<sup>-2</sup>) between the 1960s and 2020s. Over those decades, while the overall forcing continues to be dominated by CO<sub>2</sub>, this analysis points in particular to the recent positive and increasing (compared to the previous respective decades) impact of aerosol decline. This is directly related to the changes in emissions over the last two decades (Section 2 of main paper). In addition, this analysis clearly shows that the climate forcing from halogens has almost peaked. In addition, over the last three decades, the rate of increase of N<sub>2</sub>O forcing has become commensurate with CH<sub>4</sub> and O<sub>3</sub>, reflecting its recent rapid growth. Consistent with the

findings of Figure 8 (also S13), we see a slight recent decrease in the total anthropogenic forcing trend over the 2020s compared to the 2010s.

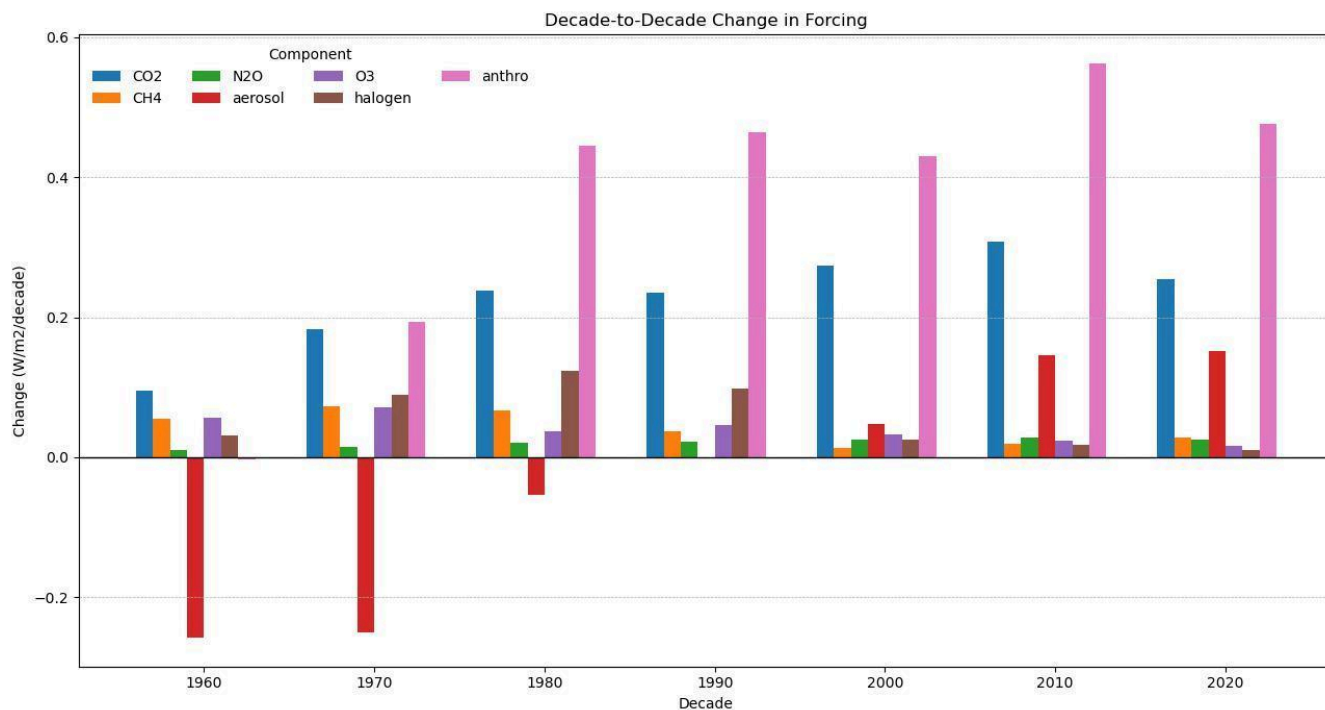


**Figure S3 Decade to decade change in ERF.**

### S5.7 Emissions-driven ERF and temperature assessment

When generating Figure 6 in the main text, a number methodological adjustments were applied to the base FaIR 1.45 parameterizations to make it more consistent with the AR6 WG1 Figure 6.12 approach. The CO lifetime sensitivity of CH<sub>4</sub> was set to 0.0002 based on multi-model estimates (Fiore et al., 2009; Wild et al., 2001), enabling the model to capture the CO-OH-CH<sub>4</sub> pathway. Oxidation CO<sub>2</sub> from the atmospheric conversion of CH<sub>4</sub>, CO, and VOCs to CO<sub>2</sub> (~2.0 Gt CO<sub>2</sub>/yr) was injected as additional emissions in each scenario, following the convention in AR6 of attributing this secondary CO<sub>2</sub> to the emitting species rather than to the CO<sub>2</sub> row. For aerosol compounds (SO<sub>2</sub>, BC, OC), the decomposition of aerosol-cloud

interactions used fixed median parameter-based fractions rather than individual counterfactuals, and temperature contributions were derived from ERF scaled by each ensemble member's transient climate response to forcing, in both cases to avoid propagating poorly constrained aerosol-cloud interaction parameters. Results are broadly consistent with the AR6 assessed values, with the largest differences arising from the longer effective methane lifetime in FaIR's calibrated constrained ensemble (which is required to make emissions match historical concentrations) that results in a negative NO<sub>x</sub> ozone forcing due to the NO<sub>x</sub>-OH-CH<sub>4</sub> feedback, as well as the inclusion of some additional feedbacks (e.g. temperature effects on ozone and CO<sub>2</sub>, black carbon albedo effects on snow and ice) that were not assessed in the AR6 Figure 6.12.

## **S6. Earth energy imbalance**

While changes in EEI have been effectively monitored at the top of the atmosphere by satellites since the mid-2000s, we rely on estimates of OHC change to determine the absolute magnitude of EEI and its evolution on inter-annual to multi-decadal time series. The AR6 assessment of ocean heat content change for the 0–2000 m layer was based on global annual mean time series from five ocean heat content datasets: IAP (Cheng et al., 2017), Domingues et al. (2008), EN4 (Good et al., 2013), JMA (Ishii et al., 2017) and NCEI (Levitus et al., 2012). Four of these datasets routinely provide updated OHC time series for the BAMS State of the Climate report, and all are used for the GCOS Earth heat inventory (von Schuckmann et al., 2020, 2023a) and the annual WMO State of the Global Climate report. The uncertainty assessment for the 0–2000 m layer used the ensemble method described by Palmer et al. (2021) that separately accounts for parametric (referred to in the plots below as “mapping uncertainty”) and structural uncertainty. The OHC change >2000 m and associated uncertainty were assessed based on trend analysis of the available hydrographic data following Purkey and Johnson (2010). A full propagation of uncertainties across all heat inventory components depends on the specific choice of time period, and different estimates are not directly comparable. Therefore, we take a simple pragmatic approach, using the total ocean heat content uncertainty as a proxy for the total uncertainty, since this term is 2 orders of magnitude larger than the other terms (Forster et al., 2021). To provide estimates of the EEI up to the year 2024, we scale up the values of OHC change in 2021, 2022, 2023, 2024 and 2025 to reflect the 91 % contribution of the ocean to changes in the Earth heat inventory (Forster et al., 2021). The EEI is then simply computed as the difference in global energy inventory over each period, converted to units of watts per square metre ( $\text{W m}^{-2}$ ) using the surface area of the Earth and the elapsed time. The uncertainties in the global energy inventory for the end-point years are assumed to be independent and added in quadrature, following the approach used in AR6 (Forster et al., 2021). Estimates of EEI should also account for the other elements of the Earth heat inventory, i.e. the atmospheric warming,

the latent heat of global ice loss and heating of the continental land surface (Forster et al., 2021; Cuesta-Valero et al., 2021, 2023; Steiner et al., 2020; Nitzbon et al., 2022; Vanderkelen et al., 2020; Adusumilli et al., 2022). Some of these components of the Earth heat inventory are routinely updated by a community-based initiative reported in von Schuckmann et al. (2020, 2023a). However, in the absence of annual updates to all heat inventory components, a pragmatic approach is to use recent OHC change as a proxy for EEI, scaling the value up as required based on historical partitioning between Earth system components (Fig S4 and S5). The CERES EBAF-TOA Ed4.2.1 data presented in the manuscript were downloaded from [https://ceres-tool.larc.nasa.gov/ord-tool/jsp/EBAF\\_TOA421Selection.jsp](https://ceres-tool.larc.nasa.gov/ord-tool/jsp/EBAF_TOA421Selection.jsp) on 25th March 2026. Since OHC timeseries were computed from annual means and therefore centred on the year mid-points, we computed the average heating rates from CERES based on July-to-June averages.

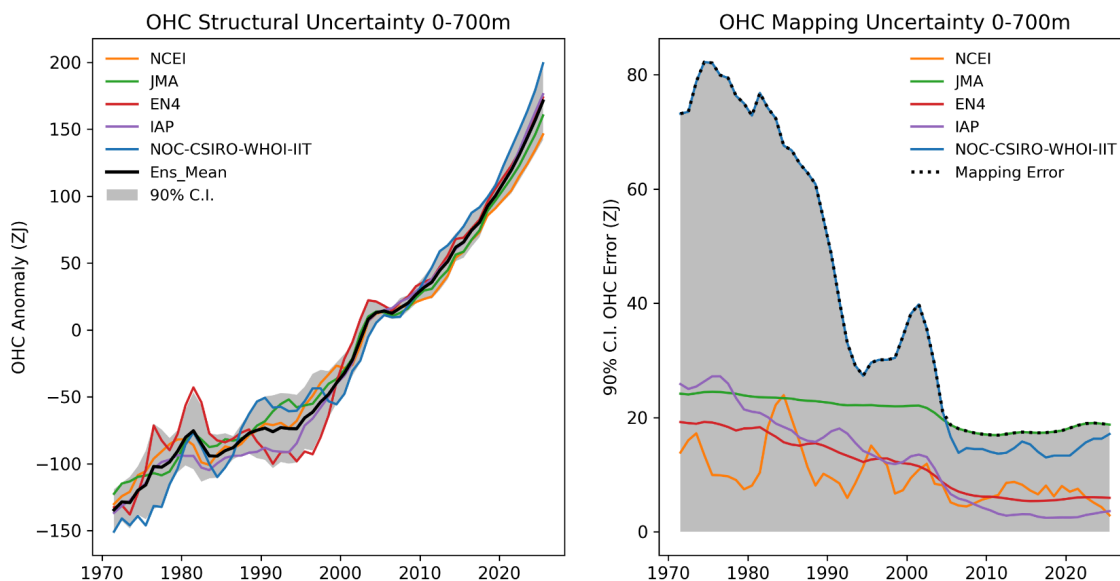


**Figure S4 (Left)** Ocean heat content timeseries for the 0-700 m layer with the estimate of structural uncertainty indicated by the grey shaded region and expressed as a 90% confidence interval (*very likely* range) in units of Zetta Joules ( $1 \text{ ZJ} = 10^{21}$  Joules). **(Right)** Individual estimates of the mapping uncertainty with the ensemble mapping uncertainty (the maximum across all available estimates) shown by the dotted line and grey shaded region. Mapping uncertainty is expressed as a 90% confidence interval (*very likely* range) in units of Zetta Joules ( $1 \text{ ZJ} = 10^{21}$  Joules).

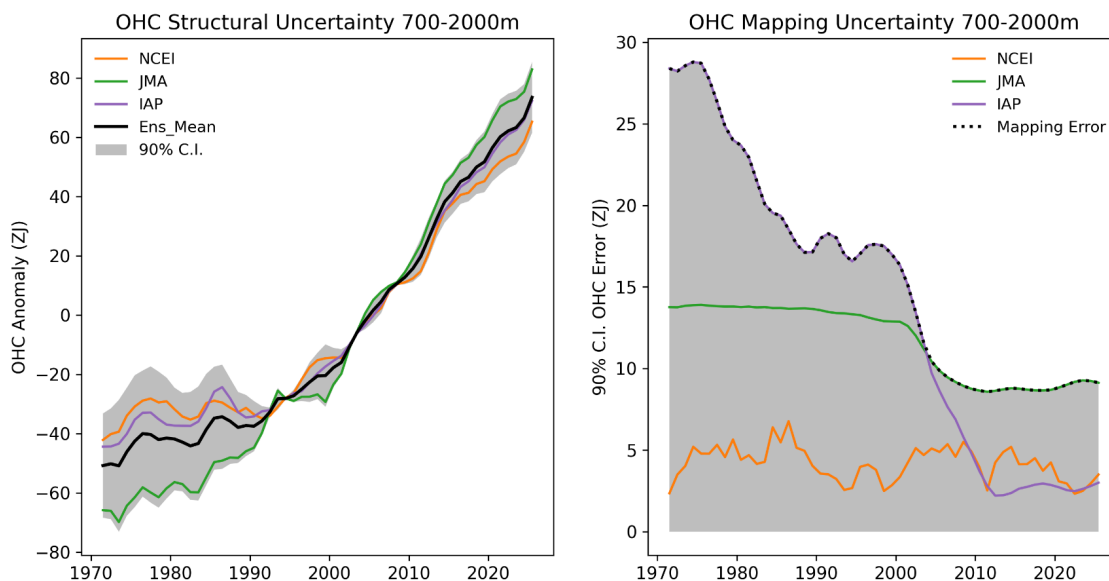


**Figure S5** As Fig. S4 but for ocean heat content in the 700-2000 m layer.

## S7. Global surface temperature

Surface temperature information on land and sea is available with low latency through WMO distribution channels, with monthly station data from a substantial number of stations reported within a few days of the end of the month. Sea-surface temperature data from ships and buoys are gathered from the Global Telecommunication System with a short delay. These are consolidated into global data sets by a number of institutions, making it feasible to report GMST updates within a few weeks of the end of the period of interest. The number of reporting locations on land with near-real time data available for reporting for the most recent periods is typically less than that available for historical data, as not all observation sites report recent data reliably, but this lower observation density only slightly increases the uncertainty in estimates of recent annual GMST compared with the past 20-30 years (Trewin et al., 2021).

The GMST assessment in AR6 was largely based on four datasets: HadCRUT5 (Morice et al., 2021), Berkeley Earth (Rohde and Hausfather, 2020), NOAA GlobalTemp - Interim (Vose et al., 2021) and Kadow et al. (2020). The four GMST datasets

were chosen by virtue of being quasi globally complete, having data back to 1850, using the most recent generation of SST analyses and using analysed (rather than climatological) values over sea ice. The first two of these are routinely updated operationally, with data for each year becoming available in the first few weeks of the following year. NOAA GlobalTemp - Interim was not updated operationally at the time AR6 was published, became NOAA's main operational GMST dataset (under the name NOAA GlobalTemp 5.1) as of January 2023, but has now been superseded by NOAA GlobalTemp 6.0.0 (Yin et al., 2024), which is used in this paper. All three datasets are updated and published monthly. The dataset by Kadow et al. is updated on an ad hoc basis by the authors (Kadow et al., 2025). A fifth data set, China - Mean Surface Temperature (China-MST) (Sun et al., 2021), which meets all the GMST dataset criteria except for treatment of sea ice areas, is used both in AR6 and here for global temperatures over land areas only. Although the version of the Kadow et al. (2020) dataset reported in that paper used HadCRUT4 as its base, the version used in AR6 and subsequently used HadCRUT5 as its base (Kadow et al., 2025)..

NOAA GlobalTemp 6.0.0 uses a new artificial neural network approach to reconstruct temperatures over land (Huang et al., 2022) in place of the empirical orthogonal teleconnection approach used in version 5.1. This change has little impact on long-term trends at global scale since the low-frequency component in the land surface air temperature (LSAT) reconstruction has not changed, but has a substantial impact on spatial and short-term temporal variability. Version 6.0.0 shows approximately 0.01 °C less warming from 1850-1900 to recent time periods (such as 2013-2022) than version 5.1, principally due to differences in the early part of the 1850-1900 baseline period. A new version of the NOAA GlobalTemp dataset (6.1.0), using the newly-developed ERSST sea surface temperature analysis (v6) (Huang et al., 2025), became the operational NOAA data set as of January 2026 but is not used in this paper.

During 2025, Berkeley Earth transitioned to a new data set version, with 0.25° resolution compared with the previous 1°, and with the interpolation approach now trained on the spatial structure and relationship of ERA5 fields, rather than kriging (Rohde et al., in prep). The new data set version is somewhat warmer over land in the early part of the record than its predecessor, and hence is warmer over the 1850-1900 period. As a result, the new version of the Berkeley Earth dataset (as implemented in this paper) shows 1.73 °C of warming over land from 1850-1900 to 2015-2024, compared with 1.82 °C in the previous version. Changes in warming over the ocean between the two versions are negligible. For GMST the warming over this period for the old and new versions is 1.26 °C and 1.22 °C respectively. The GMST impact of this version change is the largest of any version change in the data sets used in this paper since AR6, and contributes approximately -0.01 °C to the overall GMST assessment.

To date, all four GMST datasets remain supported.. Version changes to date since AR6 have resulted in the warming from 1850-1900 to 2011-2020 being 0.01 °C less in the most recent dataset versions than that reported in AR6 (Table S4), with warming of land areas being 0.02 °C less than in AR6 and warming of ocean areas being identical. .

**Table S4. Observed warming (central estimate) from 1850-1900 to various time periods in current dataset editions, AR6, and earlier IPCC Assessment Reports (where applicable)**

Time period	Observed warming from 1850-1900 (central estimate, °C)		
	Current datasets	AR6	Earlier Assessment Reports
2011-2020	1.08	1.09	
2006-2015	0.93	0.94	0.87 (SR1.5)
2003-2012	0.89	0.90	0.78 (AR5)
1981-2010	0.68	0.69 (not formally reported)	

A new version of the China-MST dataset (v3.0) has been developed and is used as part of the land component of the assessment of this paper. The land component of this uses the C-LSAT 2.1 dataset (Xu et al., 2025). Compared with earlier versions, C-LSAT 2.1 has substantially more stations and a substantially greater areal data coverage, as well as new homogenisation methods. China-MST v3.0 shows more warming over the common 1850-1900 to 2014-2023 period than the v2.0 version used in 2023 and earlier, with warming of 1.61 °C in v3.0 compared with 1.53 °C in v2.0. This change brings China-MST into closer alignment with the other four datasets although it still shows the least amount of warming of the five.

The key differences between the AR6 datasets and those used in the annual WMO and BAMS State of the Climate reports are that WMO and BAMS also incorporate reanalyses (ERA5 and JRA-3Q, which superseded JRA-55 during 2024). These reports also include the GISTEMP (Lenssen et al., 2019) dataset (excluded by AR6 because it starts in 1880) but do not include the dataset by Kadow et al. (as that is not updated operationally). In its 2025 State of the Climate report, WMO also

incorporated the China-MST dataset for GMST, and two additional datasets which have been published in the last two years, CMA-GMST (Chen et al., 2025) and DCENT-I (Chan et al., 2026). WMO also, rather than calculating values directly with respect to a 1850-1900 baseline, initially calculates values with respect to a 1981-2010 baseline and then adds to that the 0.69 °C change from 1850-1900 to 1981-2010 assessed by AR6 (WMO, 2026). This approach allows the inclusion of reanalyses, and other data sets which do not extend back to 1850.

The GMST values used in AR6 were calculated from the gridded data sets produced by the data providers, using a consistent methodology - calculating the mean anomaly for each of the northern and southern hemisphere as a latitude-weighted mean of available gridpoint values, then defining the global mean anomaly as the mean of the two hemispheric values. (This is equivalent to the method used by the Met Office Hadley Centre to report global values from HadCRUT5). The values thus calculated may differ from those reported by the data providers themselves, due to different averaging methodologies and treatment of missing data. This difference was most evident historically for the Berkeley Earth dataset although it is less pronounced for the latest version of the dataset than for previous versions. Although the difference is less pronounced in the AR6 datasets than in earlier generations of datasets, there are more gridpoints with missing data in the Southern Hemisphere than the Northern (particularly before an observation network was established on Antarctica in the 1950s), and using hemispheric means ensures that the two hemispheres are equally weighted.

The uncertainty assessment in AR6 combines the spread of the individual datasets with uncertainties derived from ensembles for HadCRUT5 and an earlier version of NOAA GlobalTemp, with the other two datasets assumed to have the same uncertainty as HadCRUT5. HadCRUT5 is the only one of the datasets for which regularly updated ensembles are currently produced, limiting the extent to which uncertainty assessments can be regularly updated from those used in AR6. In this update it was assumed that the width of the confidence interval for each individual dataset was the same as that used in AR6.

There is an ongoing review of the datasets used in global temperature assessment, both in forthcoming versions of this publication (and ultimately the IPCC AR7) and in WMO reporting.

## S7.2 2023-2025 global mean temperature anomalies

2023 set a new global annual-mean surface temperature change record, with a best estimate of 1.44 °C, beating 2016 by 0.16 °C. 2024 surpassed this, reaching 1.52 +/- 0.13 °C; 2024, becoming the first calendar year on record more likely than not exceeding 1.5 °C (Fig. 7 main paper). The assessed uncertainty range is based on that in AR6 WGI (Gulev et al., 2021). All four individual datasets are well inside the range (ranging from 1.46 to 1.56 °C). Natural drivers and internal variability are expected to modulate human-caused warming at interannual-to-decadal timescales. These values are not inconsistent with AR6, which estimated the effect of internal variability in any single year be +/- 0.25 °C based on CMIP6 models.

The probability of seeing an observed temperature of 1.51 °C in 2024 considering a human-induced warming equal to 1.36 °C is about 1 chance out of 6 (Fig. S6b). The methodology to calculate this probability consists in comparing the GSAT observed anomaly to those expected from CMIP6 models following the framework adopted in AR6 in Chapter 3 (Eyring et al., 2021) for decadal trends and adapted here for interannual time scale issues. The same probability but conditional to the fact that 2024 followed an El Niño year and that the Atlantic Multidecadal Variability (AMV) was in a positive phase, rises to 1 chance out of 2. Even if 2024 has been perceived as “extreme”, it can in fact be treated as a “normal” year, i.e. very much expected at the actual human-caused global warming level when the internal modes of variability are taken into account and when assessed from a very large number of simulations from large ensembles. Based on the same calculation, we estimate that a year as warm as 2023 would occur once in 4 years at human-induced warming equal to 1.31 °C (Fig. S6b). It drops to 1-in-14 [10-20, CI 5-95%] year event, i.e. a rare-to-exceptional event, when considering that 2023 followed a La Nina year and despite persistent positive AMV. Note that the probability of the large jump in global temperatures was increased by the fact that the El Niño followed an extended La Niña over 2020-2022 (Raghuraman et al., 2024, Mex et al. 2026). Within such a framework, 2022, that was colder than human-induced warming, could be interpreted as a normal/expected year considering that 2021 was a La Nina year and AMV positive (Fig. S6b). These results show that human induced warming combined with particular modes of natural variability shifts the odds of global surface temperatures passing 1.5 °C, making it more likely in presence of El Nino.

GSAT interannual anomalies distribution from CMIP6 for evolutive anthropogenically-forced warming (ANT\_GWL) and conditional to the combined phases of OND [yr-1] ENSO and AMV modes of variability

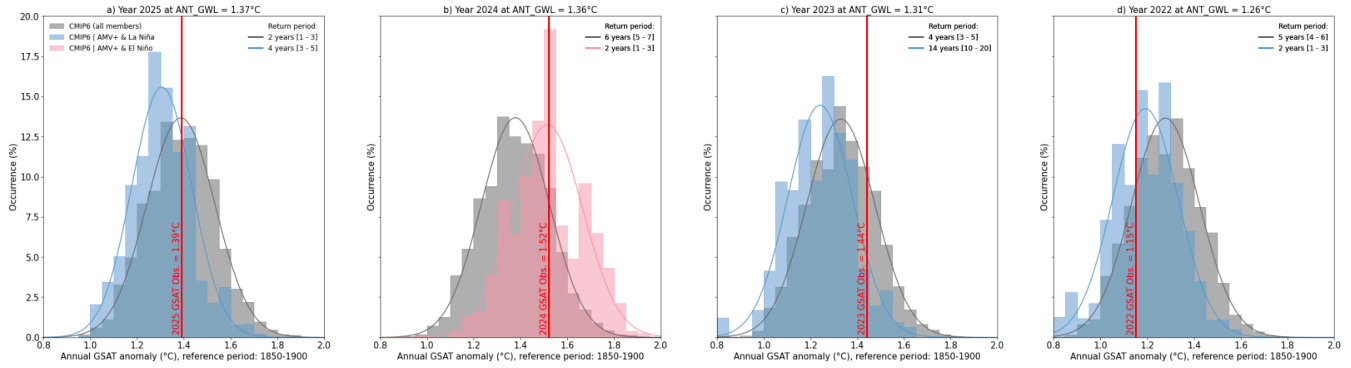


**Figure S6 a) Gray histograms of global surface air temperature (GSAT) interannual anomalies estimated from 15 CMIP6 models extracted from all available SSP scenarios (~700 members) at anthropogenic global warming levels (ANT\_GWL) corresponding to a) 2025 b) 2024, c) 2023, d) 2022. The red vertical bar stands for the observational consolidated GSAT annual anomalies (Sect. 7.1). The return period of the observed annual GSAT event estimated from the CMIP6 distribution is provided (upper-corner). Associated [5-95%] likely range is assessed through bootstrapping. Interannual anomalies are obtained following Trewin (2022) method over 10-yr sliding windows. Only models providing large-ensembles (n members >5) and having at least one member whose interannual variance of GSAT is compatible with observational estimates, are selected. Colored histograms stand for the same distribution but conditional to the combined phase of El Niño Southern Oscillation (ENSO) and Atlantic Multidecadal Variability (AMV). SST Anomalies for the modes of variability are calculated from the residual of SST obtained after removing the modelled forced response estimated as model ensemble mean. A year is considered as an El Niño/La Niña year if the (October-December) relative Oceanic Niño Index (RONI) index of the previous year is greater/lower than one standard deviation. A year is considered as an AMV+ year if the annual North Atlantic average SST is greater than one standard deviation. Light pink represents years when RONI and AMV are concomitantly positive and light-blue when RONI is negative.**

The increase in global temperature between 2022 and 2023 and in particular in global sea surface temperature is exceptional based on model estimates accounting for projected known human and natural forcings plus internal variability (Rantanen and Laaksonen, 2024; Terhaar et al., 2025, Cattiaux et al., 2024). The La Niña-to-El Niño sequence is of key importance and has been likely reinforced by enhanced energy uptake due to multi-year persistence in the preceding La Niña. The temporal synchronicity between the modes of variability in all basins is hypothesized to have played a role in the jump (Minobe et al.,

2025) with the North Atlantic being record warm (Guinaldo et al., 2025) and the austral sea ice extent being record low (Purich and Doddridge, 2023).

Possible specific causes beyond internal variability, many of which are already accounted for in the estimated human-induced warming level, have been postulated e.g.: International Maritime Organization rules on shipping fuel sulphur content that came into force in January 2021; the eruption of Hunga Tonga Hunga Ha'apai in January 2022 and other subsequent smaller volcanic activity; and a faster-than-expected onset of Solar Cycle 25. A key diagnostic of these changes including both external forcing and internal variability was the exceptional magnitude of the net energy increase into the Earth system from mid-2022 to mid-2023, driven in large part by the reduced reflectance and greater absorption of solar radiation (Hodnebrog et al., 2024; Goessling et al., 2025; Minobe et al. 2025; Allan and Merchant, 2025), which may be influenced by cloud feedbacks (Tselioudis et al., 2024) as well as surface reflectance and atmospheric composition change (see also Sect. 6 main paper).

We provide an updated estimate of the contribution of different factors to anomalous global mean surface temperatures in 2023, 2024, and 2025 (Fig. S7) by combining the results of recent studies with paired FaIR climate model simulations (Leach et al., 2021). Temperature residuals are calculated relative to an expected warming trend estimated by fitting a locally weighted regression (LOWESS, smoothing fraction = 0.2) to the IGCC composite GMST dataset through 2022, then extrapolating to 2023-2025 using a 20-year quadratic trend. This yields residuals of +0.22 °C in 2023, +0.27 °C in 2024, and +0.13 °C in 2025. These residuals differ from the approach taken in Fig. S6, as it is intended to exclude the forced response from recent changes in aerosol, solar, and volcanic outputs and allow for an explicit accounting of their role in recent warming. This is not a full attribution study; the results are presented with associated caveats to provide a possible explanation of the anomalous temperatures in 2023-2025 relative to prior years. A similar analysis formed part of the WMO 2024 State of the Global Climate report (WMO, 2025).

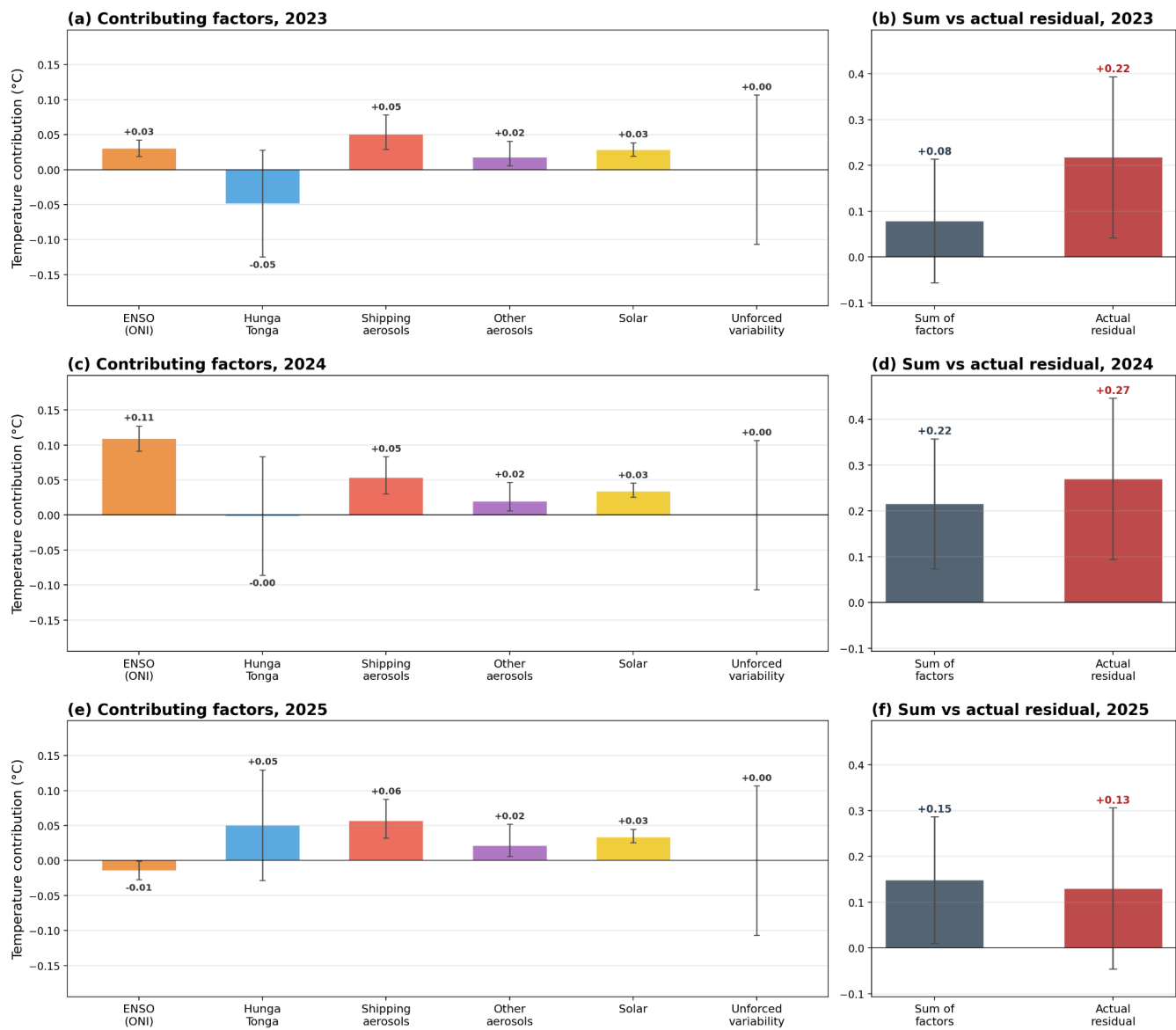


**Figure S7 Assessed contributions to 2023, 2024, and 2025 global mean surface temperature anomalies above the smoothed expected trend. Left panels (a, c, e): Individual factor contributions (°C) with 5-95% uncertainty ranges for ENSO (ONI-based regression), the Hunga Tonga–Hunga Ha'apai eruption, IMO 2020 shipping aerosol reductions, non-shipping SO<sub>2</sub> emission changes (since 2019), solar cycle 25 (since 2019 minimum), and the climatological range of unforced internal variability. Right**

**panels (b, d, f): Comparison of the sum of the five estimated forced factors (dark, with combined uncertainty added in quadrature) against the observed temperature anomaly (red). Aerosol-related factors (shipping and non-shipping SO<sub>2</sub>) reflect declines in emissions that were previously masking warming. Error bars represent 5-95% confidence intervals.**

The impact of ENSO on the temperatures can be estimated in multiple ways. Here we estimate it using a quadratic regression of FaIR-detrended GMST (e.g. GMST minus expected warming from a FaIR model run using historical emissions data) against the Oceanic Niño Index (ONI) over the 1951-2022 training period, following a 3-month optimal lag (Foster and Rahmstorf 2026). This suggests an impact of +0.03 °C, +0.11 °C and -0.01 °C for 2023, 2024 and 2025 respectively (95% CI, ±0.013 °C). In addition, we calculate the residual unforced variability in annual GMST not attributable to ENSO effects (e.g. modes of variability in other basins like AMV and other internal climate variability) in Fig. S7 (labelled “Unforced variability”). The generalized ENSO signal produced by this approach may not reflect the dynamics of any individual event, and there is some indication in the literature that the 2023 El Niño had somewhat unique characteristics that led to earlier GMST increases than is typically seen (Mex et al., 2026). Results from pre-industrial control climate model simulations (Raghuraman et al., 2024) suggest a transition from triple-dip La Niña to El Niño can produce an anomalous jump of up to 0.25 °C in the year of transition, though it is unclear how to apply this to 2023 since one would need to condition the effect on the ENSO change that was actually experienced.

The IMO regulation change in 2020 led to a rapid reduction of approximately 8.4 TgSO<sub>2</sub>/yr and a step change in radiative forcing. Using a random-effects meta-analysis of eight studies – Gettelman et al., 2024; Jordan and Henry, 2024; Quaglia and Visoni, 2024; Yoshioka et al., 2024; Yuan et al., 2024; Watson-Parris et al., 2024; Skeie et al., 2024; and Hansen et al., 2025 – the pooled central forcing is 0.14 W/m<sup>2</sup>, with individual study estimates ranging from 0.075 W/m<sup>2</sup>, (Skeie et al.) to 0.50 W/m<sup>2</sup>, (Hansen et al., something of an outlier at approximately four times the median of other studies). The estimated temperature impacts using FaIR are +0.05 °C (5–95% CI: +0.03 to +0.08 °C) in 2023, +0.05 °C (+0.03 to +0.08 °C) in 2024, and +0.06 °C (+0.03 to +0.09 °C) in 2025, with Hansen et al. accounting for the upper tail. Excluding Hansen et al., estimates are approximately one-third lower (+0.03–0.04 °C).

Global non-shipping SO<sub>2</sub> emissions have declined substantially, driven primarily by Chinese coal regulation, US and EU clean air policies, and industrial efficiency improvements (CEDS 2025). This long-term decline has already been partially absorbed into the background warming trend. Using a since-2019 baseline to isolate the contribution most relevant to the 2023–2025 anomaly (and to avoid double-counting with the shipping aerosol estimate), paired FaIR simulations yield

additional warming of +0.02 °C (5–95% CI: +0.005 to +0.04 °C) in 2023, +0.02 °C (+0.006 to +0.05 °C) in 2024, and +0.02 °C (+0.006 to +0.05 °C) in 2025 from continued land-based SO<sub>2</sub> reductions. The larger long-running decline since the mid-2000s peak (~0.09 °C by 2025) is not included in the primary estimate as it is largely captured by the LOWESS trend baseline.

The Hunga Tonga-Hunga Ha'apai (HTHH) eruption injected both SO<sub>2</sub> (~0.4 Tg) and an unprecedented ~150 Tg of water vapor into the stratosphere up to 56 km altitude (Schoeberl et al., 2024). Unlike typical eruptions, HTHH transitions from net cooling (SO<sub>2</sub> aerosol-dominated) to net warming (stratospheric H<sub>2</sub>O-dominated) over multi-year timescales. Based on a 30-member WACCM6-MAM coupled-ocean ensemble (APARC 2025 HTHH Atmospheric Impacts Report, Bednarz et al., 2026), the estimated surface temperature impact is -0.05 °C (±0.15 °C, 5–95% CI) in 2023, near-zero at -0.001 °C (±0.17 °C) in 2024, and +0.05 °C (±0.16 °C) in 2025. The sign change from 2023 to 2025 reflects the growing dominance of the stratospheric water vapor greenhouse effect as aerosol cooling wanes. Multi-model structural uncertainty is approximately ±50% based on comparisons across available models (APARC 2025, Table 7.4).

Solar cycle 25 has been significantly stronger than initial forecasts, with sunspot numbers reaching ~155 in 2024 compared to predictions of ~120 and leading to total solar irradiance values that substantially exceed earlier projections. Using the NOAA TSI CDR calibrated against FaIR's solar forcing over 2000-2015, and paired FaIR runs relative to a cycle-neutral 2015–2019 baseline, the estimated surface warming contribution since the 2019-2020 solar minimum is +0.03 °C (5–95% CI: +0.02 to +0.04 °C) in 2023, +0.03 °C (+0.03 to +0.05 °C) in 2024, and +0.03 °C (+0.03 to +0.04 °C) in 2025.

In total, the sum of identified factors – ENSO (ONI-based), Hunga Tonga, shipping aerosol reductions, non-shipping SO<sub>2</sub> reductions, and solar cycle 25 – falls within the 5–95% uncertainty range of the observed residual anomaly for all three years: the combined estimate is +0.08 °C in 2023 (observed: +0.22 °C), +0.22 °C in 2024 (observed: +0.27 °C), and +0.15 °C in 2025 (observed: +0.13 °C). The smaller unexplained residual in 2024 and 2025 compared to 2023 partly reflects the large positive ENSO contribution in 2024 and the onset of La Niña in 2025. The gap remaining in 2023 likely reflects unusual behavior of the 2023 El Niño (Raghuraman et al., 2024; Minobe et al., 2025; Mex et al., 2026) as well as unforced internal variability beyond ENSO, including the record-warm North Atlantic (Guinaldo et al., 2025) and anomalously low Antarctic sea ice extent. While ENSO, solar, and volcanic effects are expected to be transient, the warming unmasked by declining shipping and land-based aerosol emissions will persist as a sustained contribution to global temperatures in coming years.

## **S8 Human-induced global warming**

### **S8.1 Defining of warming**

#### **S8.1.2 Definitions of global warming in the IPCC sixth assessment cycle**

Tracking progress towards the long-term global goal to limit warming, in line with the Paris Agreement, requires the assessment of both what the current level of global surface temperatures are and whether a level of global warming, such as 1.5 °C, is being reached (Thorne et al., 2026). Definitions for these were not specified in the Paris Agreement, and several ways of tracking levels of global warming are in use. When determining whether warming thresholds have been passed, both AR6 and SR1.5 adopted definitions that depend on future warming; in practice, levels of current warming were therefore reported in AR6 and SR1.5 using additional definitions that circumvented the need to wait for observations of the future climate.

AR6 defined crossing-time for a level of global warming as the midpoint of the first 20-year period during which the average observed warming for that period exceeds that level of warming (see AR6 WGI Chapter 2 Box 2.3) (the level of warming for a given year defined in this way is therefore not known until 10 years after that year). AR6 therefore reported current levels of both observed and human-induced warming as their averages over just the most recent 10 years (which gives warming that lags by only 5 years instead of 10 years) (see AR6 WGI Chapter 3 their Sect. 3.3.1.1.2); we refer to this definition as the “AR6 decade-average” warming.

SR1.5 defined the level of warming in a given year as the average human-induced warming, in GMST, of a 30-year period centred on that year; when the given year is the current year, SR1.5 specified that the future 15 years (required for the mean) are revealed by extrapolating the multidecadal trend (see SR1.5 Chapter 1, their Sect. 1.2.1); we refer to this definition as the “SR1.5 trend-based” warming. If the multidecadal trend is interpreted as being linear (which it has been very close to over recent decades), this definition of current warming is equivalent to the end-point of the trend line through the most recent 15 years of human-induced warming, and therefore provides a definition of warming for the current year that only depends on historical warming and does not lag. This interpretation produces results that in recent years have been identical (or extremely close) to the current annual mean value of human-induced warming (see results in Sect. 8.2, and Supplement Sect.

S8.3), so in practice the attribution assessment in SR1.5 was based not on the trend-based definition, but on the simple annual-year attributed warming; we refer to this definition as the “SR1.5 annual-mean” warming.

A diagram of these three definitions is given in Fig. S12.

### **S8.1.2 Estimates of global surface temperature: GMST and GSAT in attributed warming assessments**

AR6 WGI (Chap. 2 Cross-Chap. Box 2.3, Gulev et al., 2021) described how global mean surface air temperature (GSAT), as is typically diagnosed from climate models, is physically distinct from the global mean surface temperature (GMST) estimated from observations, which generally combine measurements of near-surface temperature over land, with measurements of sea surface temperature over the ocean. Gulev et al. (2021) assessed with high confidence that long-term trends in the two indicators differ by less than 10%. However, based on conflicting lines of evidence from climate models and direct observations, the former showing stronger warming of GSAT compared to GMST, the latter tending to show the opposite, there is low confidence in the sign of the difference in trends. Therefore, with medium confidence, in AR6 WGI Chap. 3 (Eyring et al., 2021), the best estimates and likely ranges for attributable warming expressed in terms of GMST were assessed to be equal to those for GSAT, which means that the AR6 attributable warming assessment does not distinguish between GMST and GSAT. As such, while WGI Chap. 3 (Eyring et al., 2021) treated estimates of attributable warming in GSAT and GMST from the literature together without any rescaling, we note that climate-model-based estimates of attributable warming in GSAT are expected to be systematically higher than corresponding estimates of attributable warming in GMST (see e.g. Cowtan et al., 2015; Richardson et al., 2018; Beusch et al., 2020; Gillett et al., 2021). Therefore, given an opportunity to update these analyses from AR6, it is more consistent and more comparable with observations of GMST to report attributable changes in GMST using all three methods (described in Sect. S7). The SR1.5 assessment of attributable warming was given in terms of GMST, which is continued here. Therefore, in line with Sect. 7, AR6 WGI, and SR1.5, we adopt GMST as the estimate of global surface temperature. Findings are presented in Figs. S7, S9 and S9 and Tables S5 and S6.

## **S8.2 Methods to estimate human-induced warming**

Both SR1.5 and AR6 drew on evidence from a range of literature for their assessments of human-induced warming, before selecting results from a smaller subset to produce a quantified estimate. While both the SR1.5 and AR6 assessments used the latest Global Warming Index (GWI) results (Haustein et al., 2017), AR6 also incorporated results from two other methods, regularised optimal fingerprinting (ROF) (as in Gillett et al., 2021) and kriging for climate change (KCC) (as in Ribes et al., 2021). In AR6, all three methods gave results consistent not only with each other but also results from AR6 WGI Chap. 7 (see WGI Chap. 7 Supplementary Material (Smith et al., 2021b), Fig. 3.8 of AR6 WGI Chap. 3 (Eyring et al., 2021), and Figs. S7, S8 and S9). Note that the results from Chap. 7 were not included in the AR6 WGI final calculation because they were not statistically independent of other methods. Of the methods used, two (Gillett et al., 2021; Ribes et al., 2021) relied on CMIP6 DAMIP (Gillett et al., 2016) simulations which ended in 2020 and hence require modifications to update to the most recent years. The other two methods (Haustein et al., 2017; Smith et al., 2021b) are fully updatable and can also be made consistent with other aspects of the AR6 assessment and methods. The three methods used in the final assessment of contributions to warming in AR6 are used again with revisions for this annual update and are presented here along with any updates to their approaches.

### **S8.2.1 Global Warming Index**

Introduced in Otto et al. (2015), and refined with full uncertainty assessment in Haustein et al. (2017), the Global Warming Index (GWI) quantifies anthropogenic warming by using an established “multi-fingerprinting” approach to decompose total warming into its various components; preliminary anthropogenic and natural warming time series are first estimated from radiative forcings, and a multivariate linear regression is then taken between these preliminary GMST contributions and observed GMST, with the best fit providing the attributed anthropogenic and natural contributions to warming. As such, the GWI attribution method is directly tied to observations and therefore the resulting central estimate for human-induced warming has a relatively small dependence on the size of the uncertainties in climate sensitivity and forcing.

Substantive annual updates to the GWI assessment depend on annual updates for effective radiative forcings (ERFs) and observed temperature (GMST), both of which are provided as a part of this update (Sects. 5 and 7 respectively). The remaining inputs to the GWI assessment are updated at the less-frequent CMIP cadence; however, these contributions only weakly influence the GWI results. Further, by recomputing a “historical-only” GWI time series based only on data up to a given year, it can be shown that GWI is relatively insensitive to end-date or short-term fluctuations in observed GMST,

minimising potential confusion about the current level of warming, such as the perception of a hiatus or acceleration (see AR6 WGI Chapter 3 Cross-Chapter Box 3.1, Eyring et al., 2021), due to short-term internal variability. This, combined with the conceptual simplicity of the method, makes the GWI a relatively transparent and robust method for attributing anthropogenic warming and well-suited to providing reliable annual updates.

Where the GWI method previously separated warming contributions into two components, “anthropogenic” and “natural”, and independently attributed them, this update further separates and independently attributes contributions within the Anthropogenic component, adopting the groupings from AR6: “well-mixed greenhouse gases”, “other human forcings” and “natural forcings”. The climate response model used to estimate (pre-regression) warming from radiative forcing is updated from the AR5 Impulse Response model (AR5-IR; from AR5 Chapter 8 Supplement (Myhre et al., 2013b)) used in Haustein et al. (2017) to the Finite-amplitude Impulse Response model (FaIR; Leach et al., 2021; Smith et al., 2018b; Millar et al., 2017), which was used in SR1.5 and AR6; climate response uncertainty is included by using around 30 sets of parameters that correspond to FaIR emulating the CMIP6 ensemble, as provided in Leach et al. (2021). The updated historical ERF input to FaIR is given in Sect. 5, with uncertainty accounted for using a representative 1000-member probabilistic ensemble. Observed GMST and its uncertainty are provided by the 200-member ensemble of the annually updated HadCRUT5 (Morice et al., 2021; see Sect. 7). Uncertainty from internal variability is accounted for by using between 100-200 realisations of internal variability sampled from the CMIP6 piControl simulations (Nicholls et al., 2021). Since some CMIP6 models may have unrealistically high decadal variability, our estimates of uncertainty may be conservative (Eyring et al., 2021). Here, to partly address this, piControl timeseries are first filtered, removing simulations that drift by more than 0.15 °C per decade or exhibit unrealistic variability amplitudes. The parameters for FaIR (given in Leach et al., 2021) are tuned to GSAT outputs from CMIP6; the outputs from FaIR are not rescaled to account for the difference between GSAT and GMST in the tuning since any rescaling would be immediately and completely regressed out in the next step of the attribution process; this lack of rescaling is additionally broadly consistent with the AR6 assessment which concluded with medium confidence that GSAT and GMST are representative of each other – see Sect. S8.1. In future, FaIR could be re-tuned to GMST estimates from CMIP6 in addition to GSAT outputs to examine potential differences in the response that cannot be accounted for through a linear rescaling, though differences in the final attribution results from such a study are expected to be minimal; the regression onto HadCRUT5 provides the strongest constraint.

Producing the GWI ensemble with ~1 billion members is computationally expensive; therefore an ensemble with ~20 million members is randomly subsampled to obtain results, and repeated three times. Uncertainty converges at this scale, and repeat random samplings at the same scale lead to variation in the results of on the order of 0.01 °C.

Compared to Forster et al. (2025), the GWI calculation remains largely the same, differing only by (i) using ERFs and observed temperatures updated to 2025, (ii) averaging results across five random ~10 million member sub-samplings instead of three ~20 million member sub-samplings (due to a reduced availability of very high memory compute nodes), and (iii) constraining the total forced warming to be zero for 1850-1900 in regression, where previously (only) total forced was granted an extra degree of freedom (this could lead to a very small non-zero offset in the 1800s of < 0.02°C in total forced warming, the influence of which decreased towards the current year; changing this has a negligible effect on current total forced warming, but avoids potential complications of interpretation if the Tot timeseries is re-baselined during external applications). Collectively these changes have led to a downward revision of GWI human-induced warming for the year 2024 (between this 2025 assessment and last year's 2024 assessment) of ~0.005°C, which is less than 1/5th of the current annual warming rate, though is smaller than the expected variation from re-sampling the Monte Carlo ensemble.

### **S8.2.2 Kriging for climate change**

The kriging for climate change method was originally introduced by Ribes et al. (2021), and subsequently extended in Qasmi and Ribes (2022), to attribute past warming and constrain temperature projections over the 21st century. This statistical method is very similar to ensemble Kalman filtering or kriging. In the original publication (Ribes et al., 2021), a subset of 22 CMIP6 models was considered. For each of them, a statistical procedure was applied to estimate the warming induced by GHG, ANT (temporal smoothing procedure) or NAT (using an Energy Balance Model) forcings, respectively. This subset of models was subsequently used to form an a priori distribution (in a Bayesian sense) of past attributable warming. Then the posterior distribution of past attributable warming given observations was derived. This application was based on HadCRUT4-CW GMST observations (Cowtan and Way, 2014), inflated by 6% to account for the assessment at that time of stronger warming of GSAT relative to GMST.

Results from this calculation were quoted in Eyring et al. (2021). The update made here uses the same subset of 22 CMIP6 models. However, HadCRUT5 observations are used, instead of previous datasets, over an extended 1850-2024 period. Consistent with the AR6 assessment about GMST to GSAT warming ratio, no scaling correction is applied; i.e. the global mean value from HadCRUT5 is assumed to be representative of GSAT changes (see Sect. S8.1). As it relies on available

CMIP6 simulations, this update assumes that the world has followed a SSP2-4.5 pathway since 2015. Emissions in the SSP scenarios are similar in the period up until 2024 and close to those which have occurred (e.g. Chen et al., 2021); therefore this is a reasonable approximation. Future updates with this method will incorporate new observations. In parallel, we will try to replace the CMIP6 models by emulators, thus allowing the latest available estimates of radiative forcings to be considered, instead of the SSP2-4.5 scenario.

### **S8.2.3 Regularized optimal fingerprinting**

Optimal fingerprinting is the name given to optimal regression-based approaches to attribution, in which observed anomalies are regressed onto the simulated response to individual forcings from climate models, with the regression coefficients used to infer attributable contributions to observed changes (e.g. Allen and Stott, 2003; Eyring et al., 2021). Ribes et al. (2013) proposed an improved version of the standard total least squares regression, known as regularised optimal fingerprinting, which exhibited improved accuracy in perfect model tests. Gillett et al. (2021) applied this approach to regress observed 5-year mean observed GMST onto the simulated response to individual forcings from the DAMIP simulations (Gillett et al., 2016) of 13 CMIP6 models. In order to ensure a like-for-like comparison, Gillett et al. (2021) regressed observations of GMST, derived from gridded non-infilled near-surface air temperature over land and sea ice, and sea surface temperature over oceans, onto GMST derived from CMIP6 model output in the same way (Cowtan et al., 2015). However, since globally complete GSAT is usually used in the climate impact literature which served as a basis for global warming goals, Gillett et al. (2021) used regression coefficients to infer attributable warming in globally complete GSAT.

Gillett et al. (2021) used CMIP6 DAMIP simulations which generally finished in 2020 and therefore cannot directly be used to infer attributable warming in subsequent years. However, some modelling centres ran single-forcing DAMIP simulations into the future under the SSP2-4.5 scenario (Gillett et al., 2016). Data from concatenated historical and ssp245, hist-nat and ssp245-nat, and hist-GHG and ssp245-GHG were taken from CanESM5 (50, 10, 10), IPSL-CM6A-LR (11, 10, 6) and MIROC6 (3, 50, 50), where numbers in brackets indicate the respective ensemble sizes. Our approach assumes that observed drivers have evolved as in the SSP2-4.5 scenario over the period since 2015, which is a reasonable assumption to the present (e.g. Chen et al., 2021). As in Gillett et al. (2021), internal variability was estimated from intra-ensemble anomalies. Whereas the Gillett et al. (2021) results assessed by Eyring et al. (2021) were based on HadCRUT4, this dataset is no longer being updated, and therefore we use the non-infilled version of HadCRUT5 here (Morice et al., 2021). As shown by Gillett et al. (2021), using HadCRUT5 in place of HadCRUT4 results in a 7% increase in the best estimate of anthropogenic warming for 2010-2019, as a result of the difference in warming between the two observation datasets. Gillett et al. (2021)

regressed 34 5-year means of GMST over the period 1850-2019 onto simulated GMST over the same period. Here we extend the analysis using 35 5-year means, with the latter based on observations from January 2020 to December 2024 and the model output masked in the same way. In order to be consistent with the Global Warming Index and kriging for climate change approaches described above, and for comparison with GMST observations, we primarily report attributable warming in globally complete GMST here, rather than GSAT (see Sect. S8.1). Calculated anthropogenic warming in GSAT in 2010-2019 computed using HadCRUT5 with this approach of 1.16 (1.04-1.29) °C can be compared with the same quantity reported in Gillett et al. (2021) (their Supplementary Table 1) of 1.18 (1.09-1.27) °C, indicating good consistency.

The method described above is easily updatable into the future using the same set of simulations, simply by updating observations to a later date and masking model output accordingly. As in the KCC method, a caveat to this approach is that it relies on SSP2-4.5 simulations from which actual anthropogenic forcing might be expected to gradually diverge and from which actual natural forcing could rapidly diverge, for example, were a major volcanic eruption to occur.

**Table S5 Estimates of global mean surface air temperature (GSAT) warming attributable to multiple influences (in °C) relative to the 1850–1900 baseline period. Values are given as the median, with the 5-95 percentile range in brackets, provided to 0.01°C precision. GSAT results here are only provided for regularised optimal fingerprinting (ROF) because the GSAT results for the other attribution methods (the Global Warming Index (GWI) and kriging for climate change (KCC)) are identical to the GMST results for those methods.**

<b>variable</b>	<b>2010-2019 (decade average)</b>	<b>2016-2025 (decade average)</b>	<b>2017 (trend-based)</b>	<b>2025 (trend-based)</b>
<i>Human-induced</i>	1.15 (1.02 to 1.28)	1.36 (1.20 to 1.52)	1.19 (1.06 to 1.33)	1.51 (1.33 to 1.70)
<i>Well-mixed greenhouse gases</i>	1.43 (1.23 to 1.64)	1.59 (1.36 to 1.82)	1.48 (1.26 to 1.70)	1.71 (1.46 to 1.96)
<i>Other human forcings</i>	-0.25 (-0.45 to -0.06)	-0.23 (-0.41 to -0.05)	-0.26 (-0.47 to -0.06)	-0.21 (-0.39 to -0.04)
<i>Natural</i>	0.02 (-0.02 to 0.05)	0.01 (-0.03 to 0.05)	0.02 (-0.02 to 0.05)	0.00 (-0.04 to 0.05)

### S8.3 Results from each Attribution Method

Results for each attribution method, including headline results and timeseries, are available in csv form in the Climate Indicator repository: <https://github.com/ClimateIndicator/anthropogenic-warming-assessment/>.

**Table S6 Estimates of global mean surface temperature (GMST) warming attributable to multiple influences (in °C) relative to the 1850–1900 baseline period, provided for each warming attribution method and the overall multi-method assessment. Values for individual attribution methods are given as the median, with the 5–95 percentile range in brackets, provided to 0.01 °C precision. Values for the assessment are calculated as defined in Sect. S8.4 and given as best estimates with likely ranges in brackets.**

Variable	Method	2010-2019 (decade average)	2016-2025 (decade average)	2017 (single year annual mean )	2025 (single year annual mean )	2017 (single year trend-base d)	2025 (single year trend-base d)
<i>Human-induced</i>	<i>GWI</i>	1.05 (0.97 to 1.13)	1.21 (1.11 to 1.31)	1.12 (1.03 to 1.21)	1.33 (1.20 to 1.45)	1.10 (1.01 to 1.19)	1.33 (1.21 to 1.45)
	<i>KCC</i>	1.06 (0.92 to 1.18)	1.22 (1.07 to 1.35)	1.12 (0.98 to 1.25)	1.34 (1.18 to 1.49)	1.12 (0.98 to 1.24)	1.33 (1.17 to 1.49)
	<i>ROF</i>	1.10 (0.97 to 1.22)	1.29 (1.14 to 1.44)	1.16 (1.01 to 1.32)	1.47 (1.25 to 1.70)	1.13 (1.00 to 1.26)	1.44 (1.26 to 1.62)
	<i>Assessment</i>	1.07 (0.9 to 1.3)	1.24 (1.0 to 1.5)	1.14 (0.9 to 1.4)	1.38 (1.1 to 1.7)	1.12 (0.9 to 1.3)	1.37 (1.1 to 1.7)
<i>Well-mixed greenhouse gases</i>	<i>GWI</i>	1.30 (1.01 to 1.57)	1.43 (1.11 to 1.72)	1.35 (1.05 to 1.63)	1.52 (1.19 to 1.83)	1.35 (1.05 to 1.62)	1.52 (1.18 to 1.83)
	<i>KCC</i>	1.48 (1.16 to 1.79)	1.62 (1.26 to 1.96)	1.54 (1.20 to 1.86)	1.73 (1.34 to 2.09)	1.54 (1.20 to 1.86)	1.73 (1.34 to 2.09)
	<i>ROF</i>	1.37 (1.18 to 1.57)	1.52 (1.30 to 1.74)	1.43 (1.22 to 1.65)	1.64 (1.40 to 1.89)	1.42 (1.21 to 1.63)	1.64 (1.40 to 1.88)
	<i>Assessment</i>	1.39 (1.0 to 1.8)	1.52 (1.1 to 2.0)	1.44 (1.0 to 1.9)	1.63 (1.1 to 2.1)	1.44 (1.0 to 1.9)	1.63 (1.1 to 2.1)
<i>Other human forcings</i>	<i>GWI</i>	-0.25 (-0.50 to 0.02)	-0.21 (-0.48 to 0.07)	-0.23 (-0.48 to 0.04)	-0.19 (-0.48 to 0.11)	-0.24 (-0.50 to 0.03)	-0.18 (-0.47 to 0.11)
	<i>KCC</i>	-0.42 (-0.71 to -0.14)	-0.41 (-0.71 to -0.10)	-0.42 (-0.71 to -0.12)	-0.39 (-0.70 to -0.07)	-0.42 (-0.72 to -0.13)	-0.39 (-0.71 to -0.07)
	<i>ROF</i>	-0.25 (-0.44 to -0.06)	-0.23 (-0.40 to -0.05)	-0.25 (-0.45 to -0.05)	-0.19 (-0.38 to -0.01)	-0.26 (-0.46 to -0.06)	-0.21 (-0.38 to -0.04)
	<i>Assessment</i>	-0.31 (-0.8 to 0.1)	-0.28 (-0.8 to 0.1)	-0.30 (-0.8 to 0.1)	-0.26 (-0.8 to 0.2)	-0.31 (-0.8 to 0.1)	-0.26 (-0.8 to 0.2)

<i>Natural</i>	<i>GW1</i>	0.07 (0.01 to 0.12)	0.06 (0.01 to 0.12)	0.07 (0.01 to 0.13)	0.08 (0.02 to 0.14)	0.07 (0.01 to 0.13)	0.06 (0.01 to 0.13)
	<i>KCC</i>	0.06 (0.04 to 0.08)	0.05 (0.03 to 0.07)	0.06 (0.04 to 0.08)	0.04 (0.03 to 0.06)	0.06 (0.04 to 0.08)	0.04 (0.03 to 0.05)
	<i>ROF</i>	0.02 (-0.02 to 0.05)	0.01 (-0.03 to 0.05)	0.01 (-0.03 to 0.05)	0.01 (-0.04 to 0.05)	0.02 (-0.02 to 0.05)	0.00 (-0.04 to 0.05)
	<i>Assessment</i>	0.05 (-0.1 to 0.2)	0.04 (-0.1 to 0.2)	0.05 (-0.1 to 0.2)	0.04 (-0.1 to 0.2)	0.05 (-0.1 to 0.2)	0.04 (-0.1 to 0.2)

Validation of updated lines of evidence for assessing contributions to observed warming

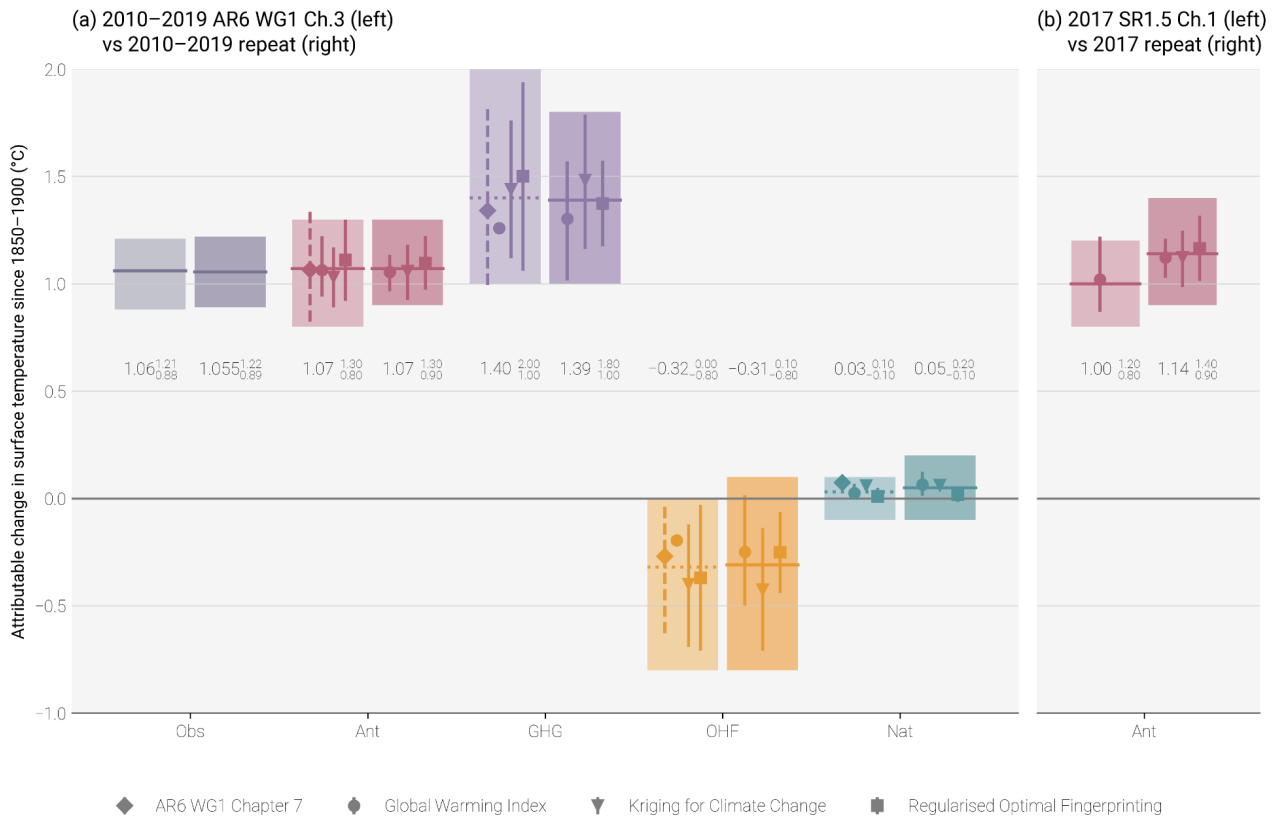


**Figure S8 Assessed contributions to observed warming and supporting lines of evidence; see AR6 WG1 Fig. 3.8. The shaded bands show the assessed *likely* ranges of temperature change, relative to the 1850-1900 baseline, attributable to total anthropogenic**

influence (Ant), well-mixed greenhouse gases (GHGs), other human forcings (OHFs), and natural forcings (Nat). The left of each pair of bands depicts the results quoted from AR6, and the right of each pair of bands depicts a repeat calculation for the same period as the IPCC assessment, using the revised datasets and methods, to validate the updated assessment of attributable warming. Panel (a) presents decade-average warming as used in AR6, with results quoted from AR6 WGI Chapter 3 on the left and the repeat assessment on the right. The solid horizontal bar in each band shows the best estimate for each warming component; if no best estimate was provided, it was retrospectively calculated using the AR6 method and depicted using a horizontal dotted line to facilitate comparison. In AR6, Global Warming Index results were reported as GMST, kriging for climate change results were calculated as GMST and scaled by 1.06 for reporting as GSAT, and regularised optimal fingerprinting was reported as GSAT; for the repeat, all methods are reported in terms of GMST (see Sect. S8.1 for discussion). Panel (b) presents single-year warming as used in SR1.5, with results quoted from SR1.5 Chapter 1 on the left (which was based only on the Global Warming Index) and the repeat assessment on the right, which now includes all of the attribution methods and the multi-method assessment approach used in AR6, as discussed in Sect. S8.4. Both bars are reported in GMST. No assessment was provided for components other than Ant in SR1.5.

Timeseries for each attribution method used in the assessment of contributions to observed warming

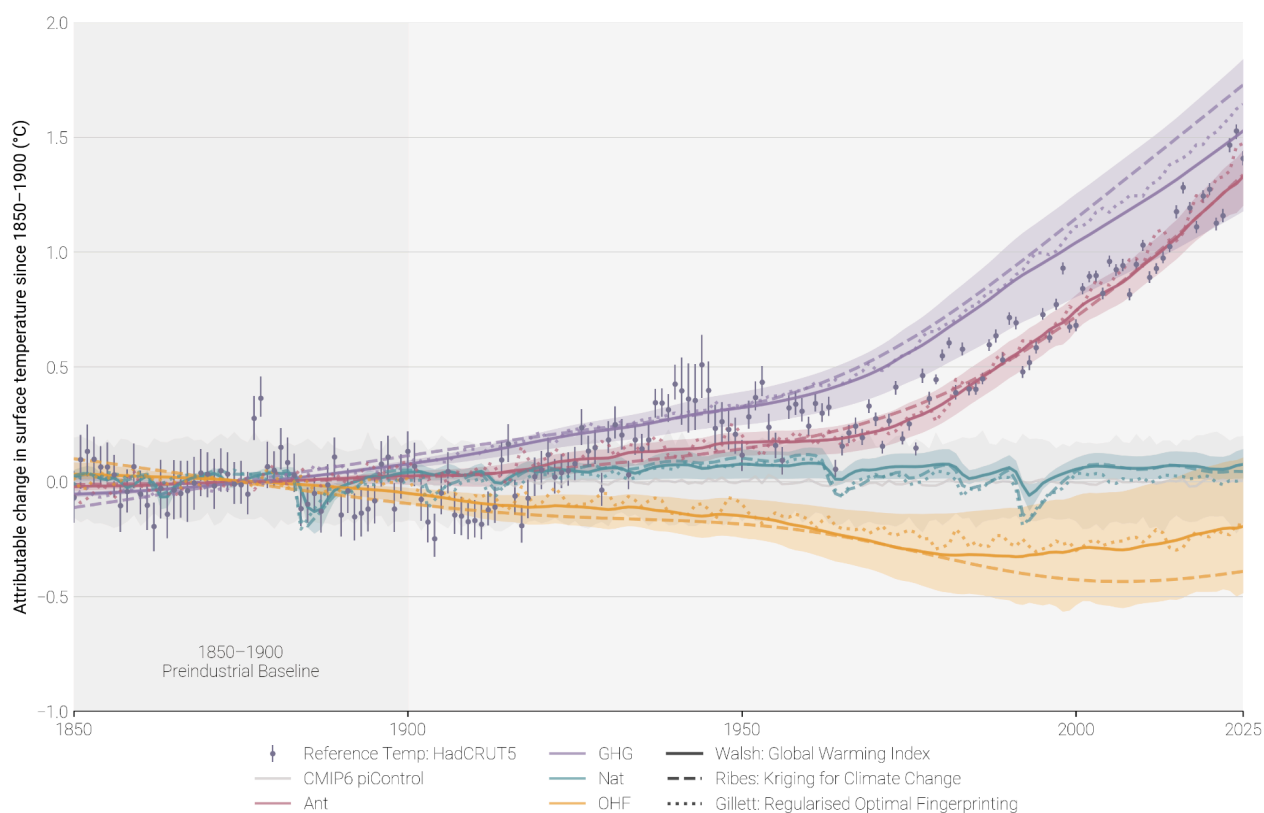


**Figure S9** Time series for each attribution method used in the updated assessment of warming contributions, expressed in terms of global mean surface temperature (GMST). Coloured plumes correspond to warming contributions broken down by natural forcings (Nat), well-mixed greenhouse gases (GHGs) and other human forcings (OHFs). Total human-induced warming (Ant) is therefore the sum of contributions from GHG and OHF. The plume range is given by the 5-95% range of the Global Warming Index (GWI), with the GWI best estimate given by the solid lines. The dashed line presents the best estimate from the kriging for climate change (KCC) method, and the dotted line presents the best estimate from the regularised optimal fingerprinting (ROF) method. GWI and KCC are given as annual values based on infilled GMST from HadCRUT5; ROF is given as annual values of globally complete GMST. The CMIP6 pre-industrial control (piControl) simulations are used as a proxy for multiple samplings of internal variability and are used to account for attribution uncertainty resulting from internal variability in the GWI method (see Sect. S8.2.1).

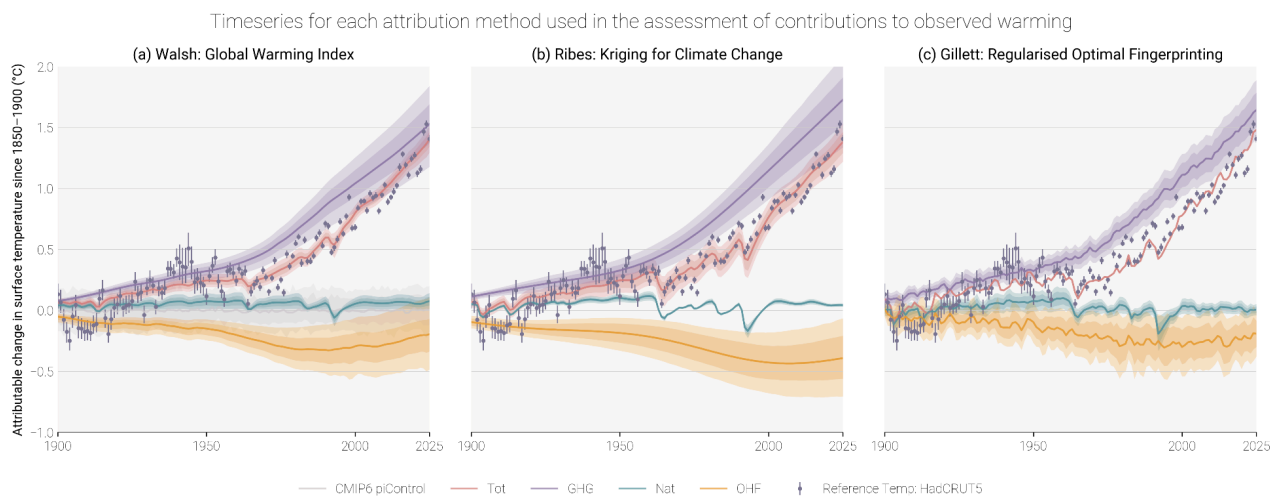


**Figure S10** Time series for each attribution method used in the updated assessment of warming contributions, expressed in terms of global mean surface temperature (GMST). Coloured plumes are given for both 17-83% and 5-95% ranges and correspond to warming contributions to observed warming broken down by natural forcings (Nat), well-mixed greenhouse gases (GHGs) and other human forcings (OHFs). Total warming (Tot) is the total attributable warming and therefore the sum of contributions from GHG, OHF and Nat. Observation data from (infilled) HadCRUT5 are presented with 9-95% uncertainty bars. Panel (a) presents results from the Global Warming Index method (Sect. S8.2.1); the CMIP6 pre-industrial control (piControl) simulations are used as a proxy for multiple samplings of internal variability and used to account for uncertainty in the attribution resulting from internal variability (see Sect. S8.2.1). Panel (b) presents results from the kriging for climate change methods (Sect. S8.2.2). Panel (c) presents results from regularised optimal fingerprinting (Sect. S8.2.3), with the time series for Tot being approximated by the sum of the Ant and Nat medians; note that this is different from GWI and KCC, where Tot is a directly attributed quantity.

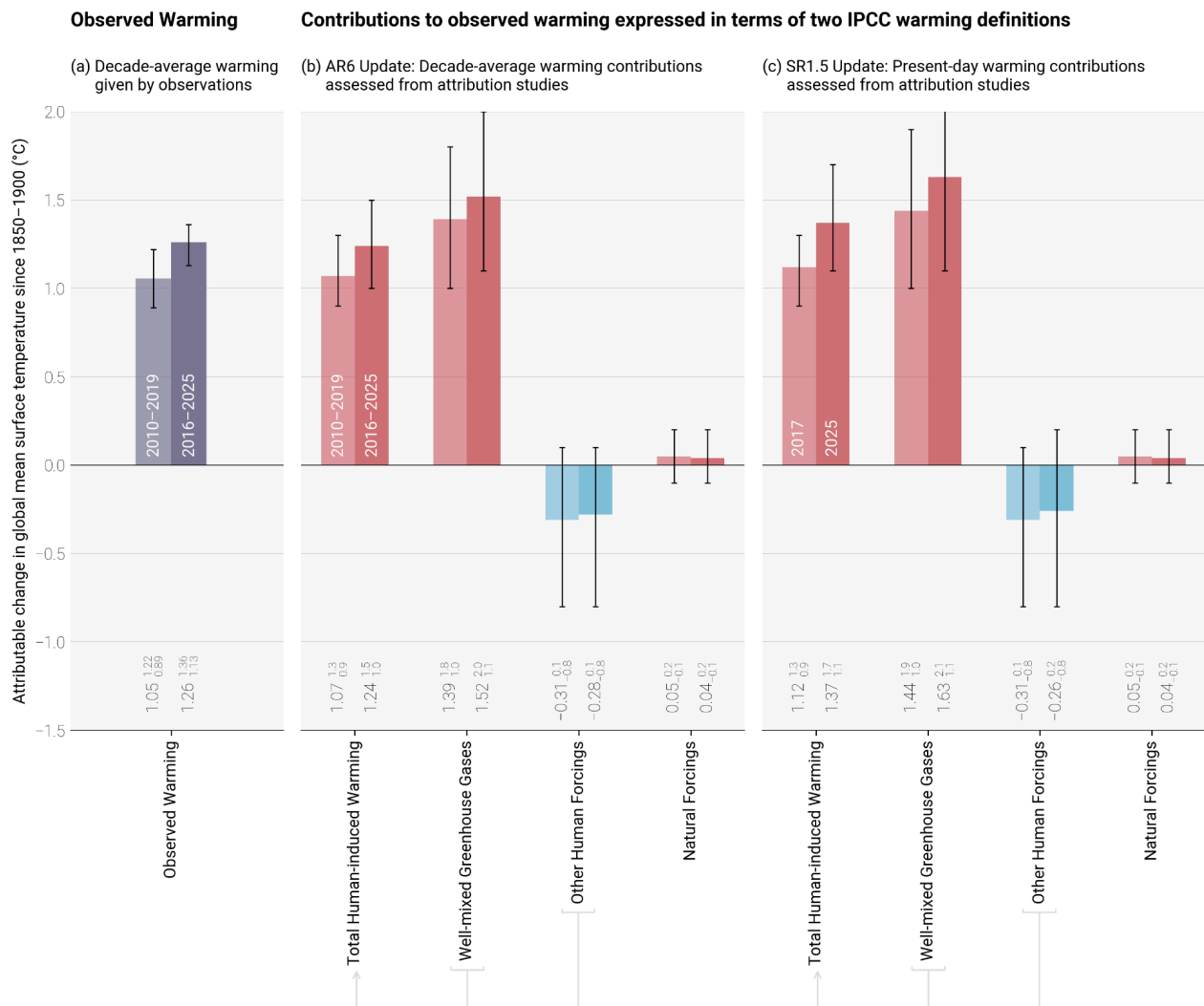


Figure S11 A repeat of Fig. 9 depicting changes to the assessed levels of warming since the sixth assessment cycle. Updated assessed contributions to observed warming relative to 1850–1900; see AR6 WGI SPM.2. Results for all time periods in this figure are calculated using updated datasets and methods. To show how these updates have affected the previous assessments, the 2010–2019 average assessed results repeat the AR6 2010–2019 assessment, and the 2017 assessed results repeat the SR1.5 2017 assessment. The 2016–2025 average and 2025 results are this year’s updated assessments for AR6 and SR1.5, respectively. For each double bar, the lighter and darker shading refers to the earlier and later period, respectively. Panel (a) shows updated observed global warming from Sect. 7, expressed as total global mean surface temperature (GMST), due to both anthropogenic and natural influences. Whiskers give the “very likely” range. Panels (b) and (c) show updated assessed contributions to warming, expressed as

global mean surface temperature (GMST), from natural forcings and total human-induced forcings, which in turn consist of contributions from well-mixed greenhouse gases and other human forcings. Whiskers give the “*likely*” range.

## **S8.4 Updated IPCC assessment approach of attributed global warming**

### **S8.4.1 Updated estimate using the AR6 WGI methodology**

Factoring in results from each of the three attribution methods (see Sect. S8.2), AR6 WGI Chap. 3 (Eyring et al., 2021) defined the *likely* range for each warming component as the smallest 0.1 °C precision range that enveloped the 5th to 95th percentile ranges of each method. In addition, a best estimate was provided for the human-induced (Ant) warming component, calculated as the mean of the 50th percentile values for each method. Best estimates were not provided in AR6 for the other components (well-mixed greenhouse gases (GHGs), other human forcings (OHFs) and natural forcings (Nat)), with their values in AR6 WGI Fig. SPM.2(b) simply being given as the midpoint between the lower and upper bound of the *likely* range and therefore not directly comparable with the central values given for human-induced and observed warming. In order to make a meaningful and consistent comparison, and provide insight into interannual changes, an improvement is made in this update: the multi-method-mean best-estimate approach is extended for all warming components.

Note that in IPCC assessments, *likely* statements typically correspond to 66–100% probability, whereas *very likely* statements correspond to 90–100% probability. Despite deriving the overall multi-method uncertainty ranges from the 5-95<sup>th</sup> percentile ranges for each method, the overall uncertainty was conservatively assessed in AR6 to be *likely* rather than *very likely*, which noted that the methods may “underestimate the importance of the structural limitations of climate models, which probably do not represent all possible sources of internal variability; use too simple climate models, which may underestimate the role of internal variability; or underestimate model uncertainty, especially when using model ensembles of limited size and inter-dependent models, for example through common errors in forcings across models” (Eyring et al., 2021). We maintain this choice of *likely* in these updates. The *likely* confidence of the AR6 assessment is also consistent with the *likely* confidence given in SR1.5 assessment - see Supplement Sect. S8.4.2.

### **S8.4.2 Updated estimate using the SR1.5 methodology applied to the AR6 WGI datasets**

While a variety of literature was drawn upon for the assessment of human-induced warming in SR1.5 Chap. 1 (Allen et al., 2018), only one method, the Global Warming Index (GWI), was used to provide a quantitative assessment of the 2017, “current”, level of human-induced warming. The latest results for this method were provided by Haustein et al. (2017), who

gave a central estimate for human-induced warming in 2017 of 1.01 °C with a 5%–95% range of (0.87 to 1.22 °C). SR1.5 then accounted for methodological uncertainty by rounding this value to 0.1 °C precision for its final assessment of 1.0 °C and assessing the 0.8 to 1.2 °C range as a *likely* range. No assessment of the contributions from other components was provided due to limitations in the GWI approach at the time.

While it is possible to continue the SR1.5 assessment approach of using a single method (GWI) rounded to 0.1 °C precision, for the purpose of providing annual updates this is insufficient; (i) 0.1 °C precision is too coarse to capture meaningful inter-annual changes to the level of current warming, (ii) using different selections of methods prevents meaningful comparison between the results for decadal mean and current single-year warming calculations, and (iii) using the mean of multiple methods increases the robustness of the results. These points are simultaneously addressed in this update by adopting the latest multi-method assessment approach, as established in WGI AR6, for both the AR6 decadal mean warming update and the SR1.5 current single-year warming update. Further, where SR1.5 only provided an assessment for human-induced warming, updates in available attribution methods since SR1.5 mean that it is now also possible to provide a fully consistent assessment for all warming components. This update reports values in Table 6b of the main paper for the current single-year attributable warming calculated using the full SR1.5 trend-based definition (as discussed in Sect. 8.1), with a comparison to results for the current single-year attributable warming calculated using the simple annual mean definition provided in Table S6.

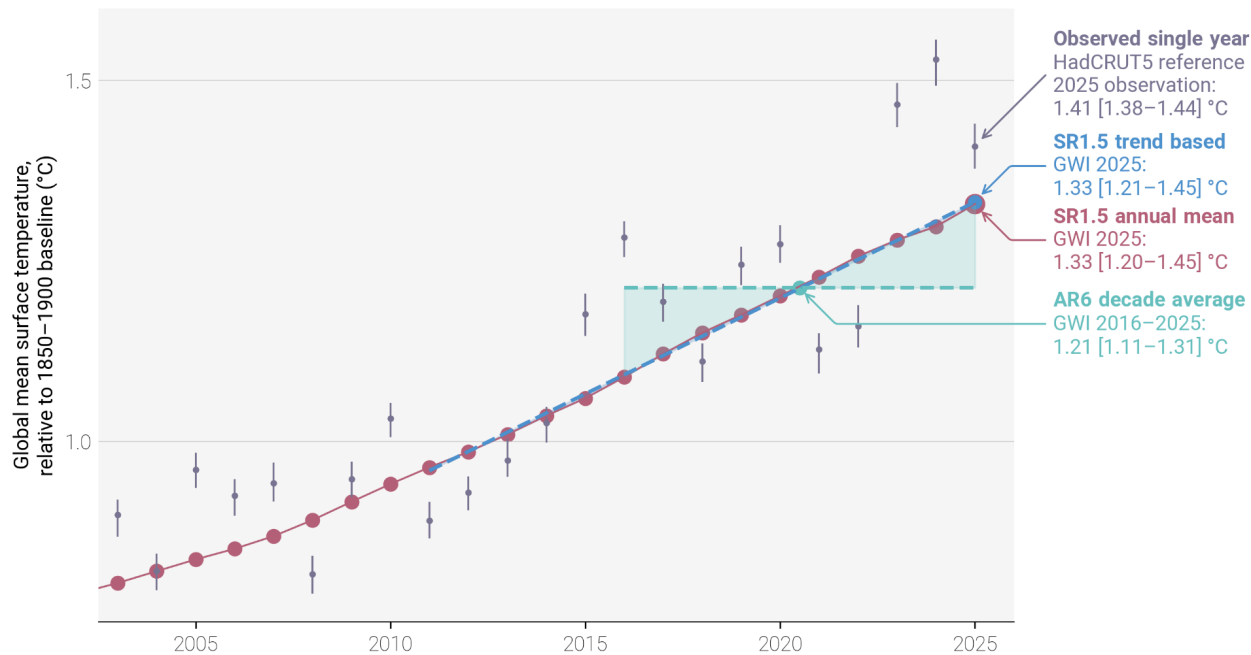


**Figure S12 Anthropogenic warming period definitions adopted in the IPCC sixth assessment cycle.** A single sampled time series of anthropogenic warming is shown in red (in this case from the GWI method – see Sect. S8.2.1). Annual-mean warming is given by the annual values of the GWI time series. The AR6 decade-average warming is given by the average of the 10 most recent annual-mean anthropogenic warming values; this is depicted by the dashed green line with shading between this and the red annual-mean values. The decade-average value for 2016–2025 is given by the green dot. SR1.5 trend-based warming is given by the end point of the linear trend line through the 15 most recent annual-mean anthropogenic warming values; this is depicted by the dashed blue line with shading between this and the red annual-mean values; the trend-based value for 2025 is given by the blue dot. Reference observations of GMST are provided from HadCRUT5, with 5%–95% uncertainty range. In practice, the annual-mean, trend-based, and decade-average calculations are applied at the level of the individual ensemble members for each of the three attribution methods; percentiles of those ensemble results provide central estimates and uncertainty ranges for each method, and the multi-method assessment combines those into the final assessment results with uncertainty (as described in Sect. S8.4). For reference, the GWI results for 2025 (provided in Sect. 8.3) are annotated in the figure.

## **S8.5 Rate of human-induced warming**

### **S8.5.1 SR1.5 and AR6 definitions of warming rate**

Following the approach from previous years' assessments, we use recent IPCC definitions of anthropogenic warming rate. In SR1.5 a number of separate studies were considered, with each study defining the rate of warming in a separate way. SR1.5 concluded that the rate of anthropogenic warming in 2017 was 0.2 °C per decade (likely range spanning 0.1 °C to 0.3 °C per decade). AR6 WGI utilised three methods (GWI, KCC, ROF; see definitions in Section S8.2), with the rate defined as the linear trend over the preceding decade of attributed warming. While AR6's best-estimate trends were all higher than in SR1.5's assessment, Eyring et al. (2021) concluded that there was insufficient evidence to change the assessed anthropogenic warming trend, which remained at 0.2 °C per decade (likely range spanning 0.1 °C to 0.3 °C per decade).

### **S8.5.2 Methods**

Here, we use AR6's definition for rate of warming, calculated using ordinary least-squares linear regression. As noted in previous assessments, this means the rate of warming in a given year is the trend centred on the preceding decade (i.e. it lags 5 years behind present day). We calculate the warming rate for each attribution method separately.

Only the GWI methodology relies on the updated historical forcing timeseries presented in Sect. 5, with the other two methods (ROF and KCC) relying on CMIP6 SSP2-4.5 simulations, which are out of date, having decoupled from historical trends in 2017 (see Sect. S8.2). As discussed in previous years, very recent changes in anthropogenic forcing are not captured fully in the decade-average trend estimated from these attribution methods. Further, the anthropogenic forcing record used for attributing warming contains small contributions from biomass burning in the natural environment, because of difficulty separating this in estimates of anthropogenic aerosol emissions. It is not expected that either of these effects will substantially bias the globally-averaged rate of warming estimated here.

## S8.5.3 Results

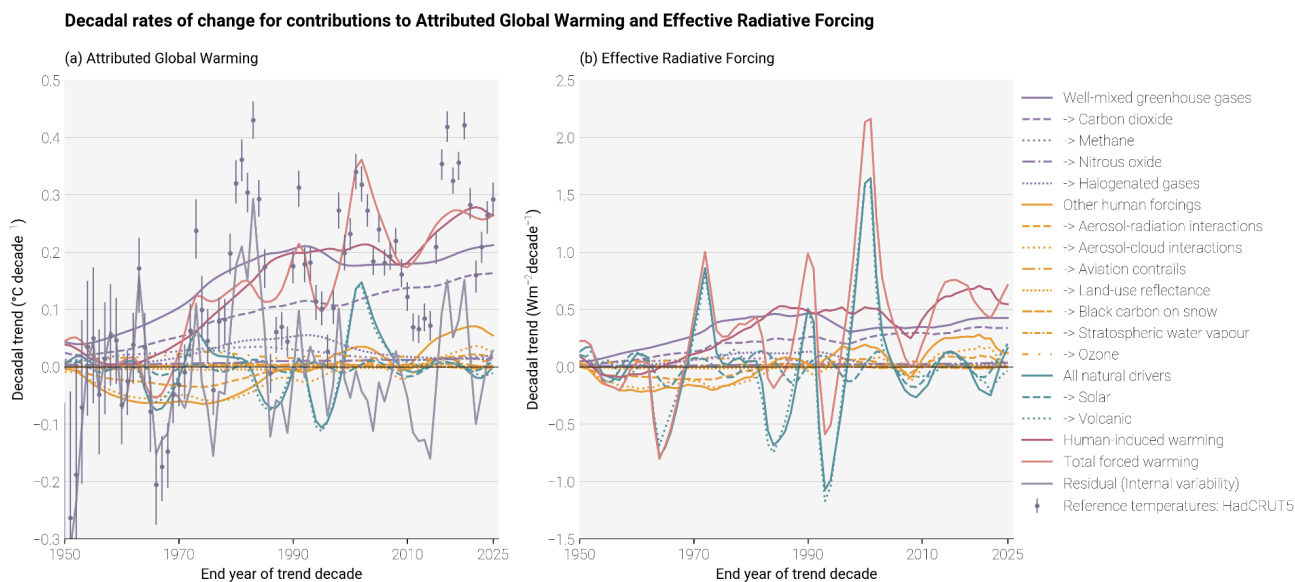


**Figure S13 Rates of (a) attributable warming (global mean surface temperature (GMST)) and (b) effective radiative forcing. The attributable warming rate time-series are calculated using the Global Warming Index method with full ensemble uncertainty. The observed GMST rates included for reference are also calculated with uncertainty from the HadCRUT5 ensemble. This is an extension of Figure 10 in the main text, showing a component-wise breakdown of the aggregate variables, presented here without uncertainty plumes for visual clarity.**

Individual warming rate attributions are revised upwards slightly from previous years (see Table 7 in main text and Table S7 below). For the decade 2016–2025 relative to 2015–2024, both KCC and GWI remained the same as the previous year’s rate, while ROF decreased by 0.03 °C/decade. This decrease in the ROF method’s rate returns the rate estimate closer to the 2024 paper’s rate estimate, with the 2025 paper’s estimate having previously increased by 0.04 °C/decade. These variations principally reflect the fact that the methodology, based on a linear regression of CMIP ensemble member’s historical (plus SSP scenario projection to present day) warming onto observed GMST anomaly, is strongly influenced by residual internal variability that remains in the anthropogenic warming signal due to the limitations in size of the CMIP ensemble, particularly given that the number of CMIP ensemble members which project ensemble members forward to 2025 is reduced compared to those running the full historical experiment.

The full uncertainty ranges of the three methodologies are also revised in table S7, reflecting new information on the warming rate implied by the 2025 observed GMST anomaly, the update of HadCRUT from 5.0.2 to 5.1.0, and additional information on the recent radiative forcing rate in the case of GWI. KCC’s 5th-percentile warming rate is decreased to 0.22°C/decade, and ROF’s 95th-percentile warming rate is decreased to 0.54°C/decade. The GWI method – which incorporates updated historical forcing estimates described in section S5 – have both decreased 5th-percentile warming rate (0.18°C/decade) and increased 95th-percentile warming rate (0.32°C/decade). Following the approach in SR1.5 and AR6, and previous assessments here, the assessed warming rate is estimated excluding the ROF methodology, deemed an outlier strongly influenced by internal variability in historical GMST and SSP2-45 GSAT anomalies calculated from CMIP6 model outputs. Although the GWI method has a 5th-percentile warming rate which is below 0.2°C/decade, we choose here to maintain the overall assessed warming rate range at the previously-assessed 0.2–0.4°C/decade.

**Table S7 Estimates of the rate of anthropogenic warming (in °C per decade), provided for each warming attribution method and the overall multi-method assessment. Values for individual attribution methods are calculated as defined in Sect. S8.5 (least squares fit through most recent 10-year period), with best estimates provided as the median, with the 5-95 percentile range in brackets, provided to 0.01 °C precision.**

Variable	Method	2010-2019 AR6 Quote	2010-2019 Repeat	2016-2025
<i>Rate of human-induced warming</i>	<i>GWI</i>	0.23 [0.19 to 0.35]	0.27 [0.22 to 0.32] GMST	0.26 [0.18 to 0.32] GMST
	<i>KCC</i>	0.23 [0.19 to 0.29]	0.25 [0.21 to 0.30] GMST	0.27 [0.22 to 0.32] GMST
	<i>ROF</i>	0.35 [0.30 to 0.41]	0.27 [0.16 to 0.37] GMST	0.39 [0.25 to 0.54] GMST
	<i>Assessment</i>	0.2 [0.1 to 0.3]	0.26 [0.2 to 0.4]	0.27 [0.2 to 0.4]

## S9. Remaining carbon budget

The remaining carbon budget is tabulated below for all decimals between 1.5 °C and 2 °C. In Table S8 we present results directly comparable to Table 8 of the main paper except using the total warming instead of anthropogenic warming. In Table S9 we average the non-CO<sub>2</sub> impacts as estimated by MAGICC (as in other tables) and the simple climate model FaIR. We also include an uncertainty of ±0.19 °C in the post-net zero warming (ZEC) in Table S9. This corresponds to the “default

update” in Lamboll et al. (2023), using the updated values for recent temperatures and emissions. Finally, these numbers are calculated using the most recent, human-attributable warming S10.

**Table S8 remaining carbon budgets, using observed warming (2016-2025) instead of anthropogenic warming as in the main case, using only MAGICC.**

Temperature (°C)	Estimated remaining carbon budgets from the beginning of 2026 base year (GtCO <sub>2</sub> )						
Avoidance probability (TCRE uncertainty only):	10%	17%	33%	50%	67%	83%	90%
1.5	410	280	160	100	50	10	-10
1.6	770	570	380	280	210	140	100
1.7	1130	870	610	460	360	270	220
1.8	1500	1160	830	650	520	400	340
1.9	1860	1450	1050	830	670	530	460
2	2220	1740	1270	1010	830	660	580

**Table S9 remaining carbon budgets, including uncertainty in ZEC and averaging results from MAGICC and FaIR for non-CO<sub>2</sub> warming.**

Temperature (°C)	Estimated remaining carbon budgets from the beginning of 2026 base year (GtCO <sub>2</sub> )						
Avoidance probability (TCRE and ZEC uncertainty):	10%	17%	33%	50%	67%	83%	90%

1.5	1000	720	400	190	0	-220	-360
1.6	1290	960	600	370	170	-40	-180
1.7	1600	1220	810	550	340	120	-10
1.8	1920	1480	1010	730	500	280	140
1.9	2250	1740	1220	910	670	430	290
2	2580	2020	1430	1090	830	580	440

**Table S10 years that a linear path would take to get to net zero, assuming an immediate start and meeting the remaining carbon budgets in the main paper (table 8).**

Temperature (°C)	Years after 2026						
	10%	17%	33%	50%	67%	83%	90%
Avoidance probability (TCRE uncertainty only):							
1.5	22	16	10	6	4	2	0
1.6	39	29	20	15	11	8	6
1.7	56	43	30	23	18	14	11
1.8	73	57	41	32	25	20	17
1.9	90	70	51	40	33	26	23
2	107	84	61	49	40	32	28

Estimating the remaining carbon budget (RCB) requires an estimate of future non-CO<sub>2</sub> warming. The latter estimate is derived from the emissions trajectories as modelled by internally consistent emissions scenarios. While RCB estimates are for CO<sub>2</sub> emissions only, the consideration of non-CO<sub>2</sub> warming implies that assumptions are also made about reductions in other anthropogenic forcings (Rogelj and Lamboll, 2024). These reductions have to be kept in mind, as a shortfall in non-CO<sub>2</sub> greenhouse gas emissions would result in a smaller RCB estimate. For instance, as reported in Rogelj and Lamboll (2024), the estimate of RCBs consistent with limiting warming to 1.5 °C assumes a median reduction in CH<sub>4</sub> emissions between 2020 and 2050 of 51% (while the interquartile range across available scenarios is 47–60%), a 22% reduction between 2020 and 2050 in N<sub>2</sub>O emissions (interquartile range: 7–35%), and a 78% reduction between 2020 and 2050 in SO<sub>2</sub> emissions (interquartile range: 74–78%). Assumed reductions consistent with other levels of warming are reproduced from Rogelj and Lamboll (2024) and provided in Table S10. The estimates reported in Table 8 of the main paper are based on the median non-CO<sub>2</sub> emission reductions. Falling short of achieving the assumed non-CO<sub>2</sub> greenhouse gas emissions reductions would further reduce the RCB. Sulphur dioxide emissions are more tightly co-controlled with CO<sub>2</sub> reduction because of the phase-out of unabated fossil fuel combustion and air pollution control measures (Rogelj et al., 2014a, 2014b). A shortfall in their reductions would therefore be less conceivable in a net-zero CO<sub>2</sub> world.

**Table S11 Non-CO<sub>2</sub> reductions implied in Remaining Carbon Budget (RCB) estimates, adapted from Rogelj and Lamboll (2024). Values represent the changes in non-CO<sub>2</sub> emissions between 2020 and 2050 consistent with the RCB estimates for 1.5°C, 1.7°C and 2.0°C. The median changes are the default and marked in light blue. Any deviation from this median assumption results in an increase or decrease of the RCB estimate.**

Temperature level for which RCB was estimated	Percentile	Implied non-CO <sub>2</sub> change between 2020 and 2050 [%]		
		CH <sub>4</sub>	N <sub>2</sub> O	SO <sub>2</sub>
1.5°C	10 <sup>th</sup>	-69	-47	-80
	25 <sup>th</sup>	-60	-35	-78
	50 <sup>th</sup>	-51	-22	-78
	75 <sup>th</sup>	-47	-7	-74
	90 <sup>th</sup>	-39	+2	-66

1.7°C	10 <sup>th</sup>	-62	-42	-78
	25 <sup>th</sup>	-53	-30	-76
	50 <sup>th</sup>	-44	-18	-73
	75 <sup>th</sup>	-39	-3	-68
	90 <sup>th</sup>	-31	+6	-60
2.0°C	10 <sup>th</sup>	-51	-35	-75
	25 <sup>th</sup>	-43	-23	-72
	50 <sup>th</sup>	-34	-11	-66
	75 <sup>th</sup>	-27	+2	-59
	90 <sup>th</sup>	-20	+12	-51

## **S10. Indicator of climate and weather extremes: land average maximum temperatures and number of marine heatwave days**

### **S10.1 Land average annual maximum temperature (TXx) – Methods**

The choice of datasets for the analysis of land average TXx is based on a trade-off between record length, data availability, near real-time updates, and long-term support. As the indicator averages over all available land grid points, the spatial coverage should be high to obtain a meaningful average, which further limits the choice of datasets. The HadEX3 dataset (Dunn et al., 2020), which is used for Fig. 11.2 in Seneviratne et al. (2021), is static and does not cover years after 2018. We therefore additionally include the Berkeley Earth Surface Temperature dataset (building off Rohde et al., 2013) and the fifth-generation ECMWF atmospheric reanalysis of the global climate (ERA5; Hersbach et al., 2020). Berkeley Earth data currently enable an analysis of annual indices up to 2023, while ERA5 covers the whole of 2025 as it is updated daily with a latency of about 5 d (and the final release occurs after 2–3 months).

For HadEX3, we select the years 1961–2018, to exclude years with insufficient data coverage, and require at least 90 % temporal completeness, thus applying the same criteria as for Fig. 11.2 in Seneviratne et al. (2021). Berkeley Earth provides daily maximum temperatures, and we require more than 99 % data availability for each individual year and grid point, such that years with more than 4 missing days are removed. Based on this criterion, Berkeley Earth covers at least 95 % of the global land area from 1955 onwards. ERA5, on the other hand, has full spatio-temporal coverage by design, and hence the entire currently available period of 1950–2025 is used. The annual maximum temperature is then computed for each grid point, and a global area-weighted average is calculated for all grid points with at least 90 % temporal completeness in the respective available period (1955–2023 and 1961–2018 for Berkeley Earth and HadEX3, while ERA5 is again not affected by this criterion). We thus enforce high data availability to adequately calculate global land averaged TXx across all three datasets, but their coverage is not identical, which introduces minor deviations in the estimated global land averages. The resulting TXx time series are then computed as anomalies with respect to a baseline period of 1961–1990.

To express the TXx as anomalies with respect to 1850–1900, we add an offset to all three datasets. The offset is based on the Berkeley Earth data and is derived from the linear regression of land mean TXx to the annual mean global mean air temperature over the period 1955–2020. The offset is then calculated as the slope of the linear regression times the global mean temperature difference between the reference periods 1850–1900 and 1961–1990 (see Fig. S14).

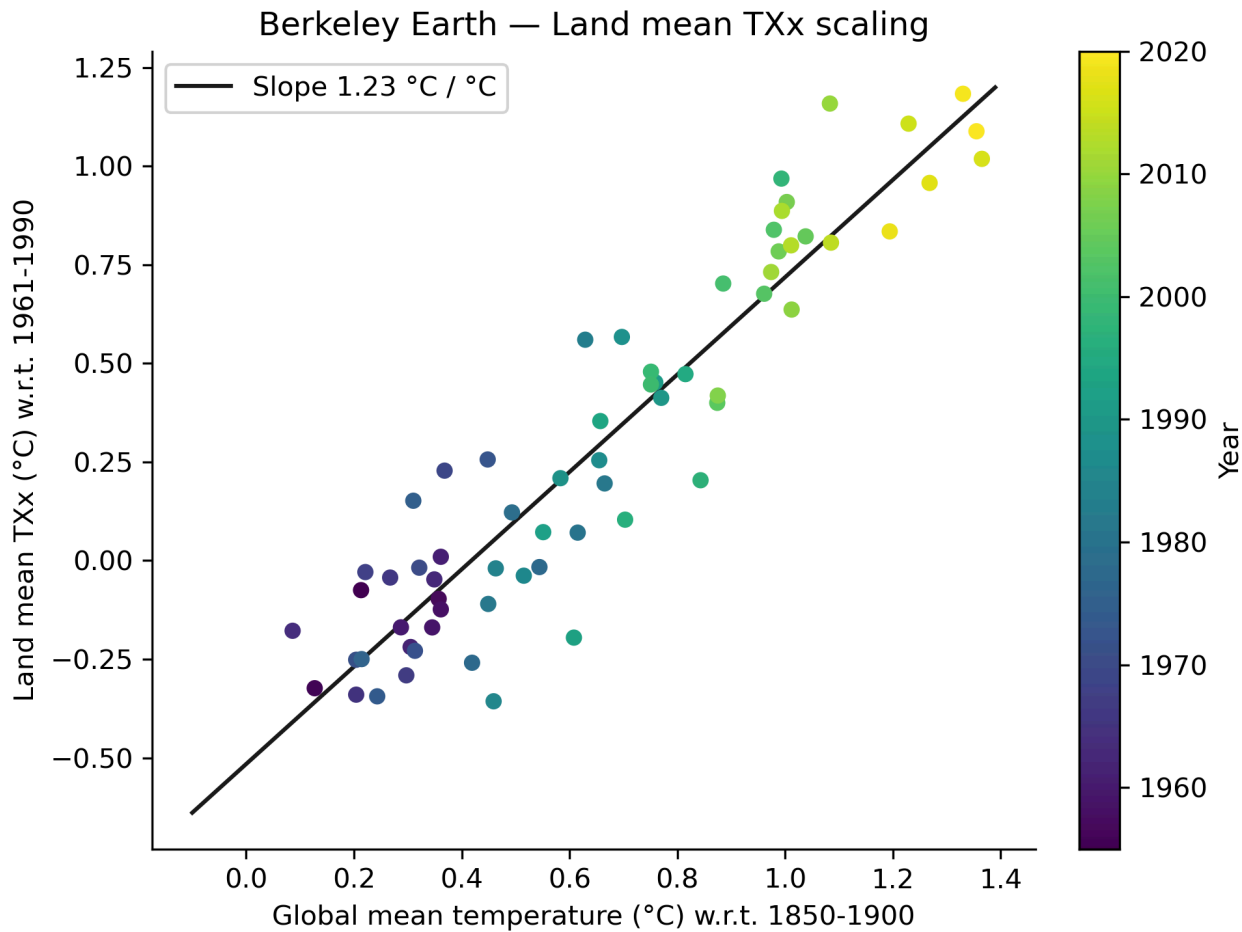


**Figure S14** Calculation of relationship between land mean annual maximum temperature (TXx) and global mean temperature. This is used to determine the TXx offset between 1850–1900 and 1961–1990. A linear regression of TXx as a function of global mean temperature from Berkeley Earth is fitted to data from 1955–2020. The TXx offset of 0.51 °C is then obtained by multiplying the slope of the linear regression (1.23 °C / °C) with the global mean temperature difference between 1850–1900 and 1961–1990 (0.42°C).

### S10.2 Number of marine heatwave days : methods

Daily sea surface temperature (SST) data were used from globally available datasets extending through 2025. The datasets used include NOAA OISST and ERA5, both provided at a spatial resolution of 0.25°, as well as higher-resolution products

including OSTIA and NOAA Coral Reef Watch (CRW) at 0.05°. To ensure consistency across datasets and to facilitate intercomparison, all SST products were regridded to a common 0.25° spatial resolution.

Marine heatwave (MHW) days were identified following the methodology outlined in the IPCC SROCC and AR6 WGI (Fox-Kemper et al. 2021; Collins et al., 2019). Specifically, at each ocean grid cell, a MHW day was defined as a day on which SST exceeds the 99th percentile threshold within an 11-day moving window relative to a climatological baseline. The climatological reference period used here is 1985–2014, from which daily percentile thresholds were computed separately for each grid cell. Annual MHW days were then calculated at each grid cell and subsequently averaged spatially to produce a global mean annual MHW day metric

To place MHW days in a preindustrial context, an offset correction was applied to the climatology. This adjustment follows established approaches to align modern climatological baselines with preindustrial conditions (e.g., Laufkötter et al. 2020). The offset was calculated using ERSST v6 by estimating the mean SST difference between the climatological period (1985–2014) and the preindustrial baseline (1850–1900). This difference was then subtracted from the climatological thresholds, effectively shifting them to approximate preindustrial conditions (see Fig. S15).

This framework enables consistent detection of MHW days across datasets while accounting for long-term warming, thereby providing a robust basis for assessing changes in extreme SST events relative to both present-day and preindustrial baselines.

**Table S12 Trend factors of the global annual number of MHW days from OISST, OSTIA, ERA5, CRW, and their mean.**

	OISST	OSTIA	ERA5	CRW	Mean
1982-2016	2.4	2.2	1.7	-	2.1
1983-2017	2.2	1.8	1.6	-	1.9
1984-2018	2.6	3.1	2.0	-	2.6
1985-2019	4.1	3.1	2.5	2.4	3.0
1986-2020	3.7	3.0	2.5	2.5	2.9
1987-2021	2.7	2.2	1.9	2.0	2.2
1988-2022	3.1	2.6	2.3	2.5	2.6
1989-2023	4.4	3.3	3.2	3.4	3.6
1990-2024	4.3	2.7	2.9	3.2	3.3

1991-2025	3.8	3.6	2.7	3.1	3.3
-----------	-----	-----	-----	-----	-----

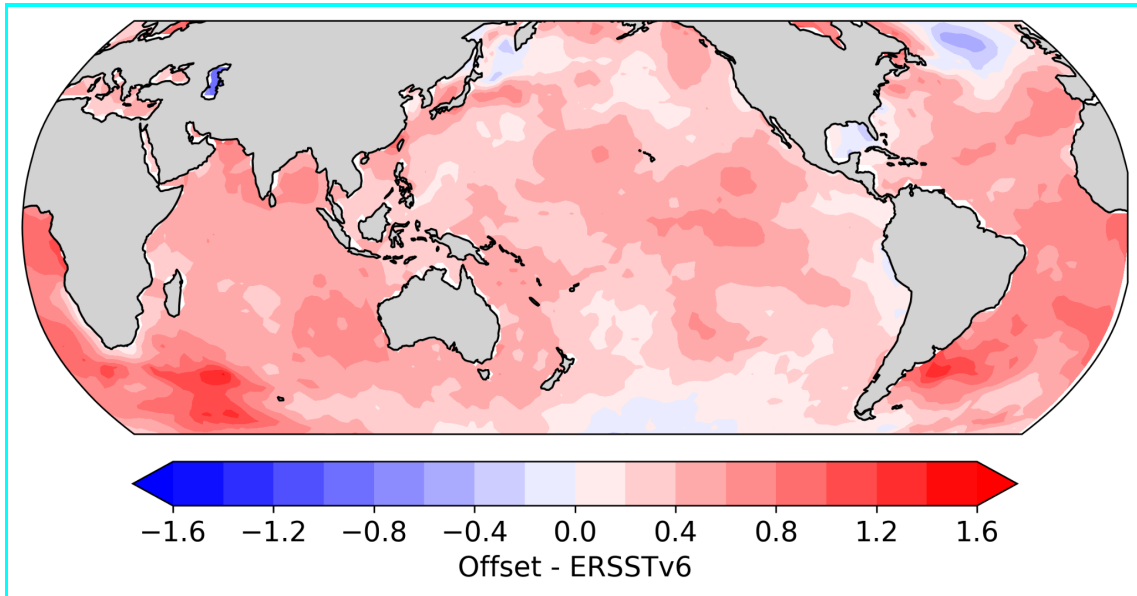


**Figure S15** Global map showing the offsetting used to adjust the climatology to a preindustrial baseline. The figure shows the difference between average SSTs from 1985-2014 to 1850-1900 from ERSST v6.

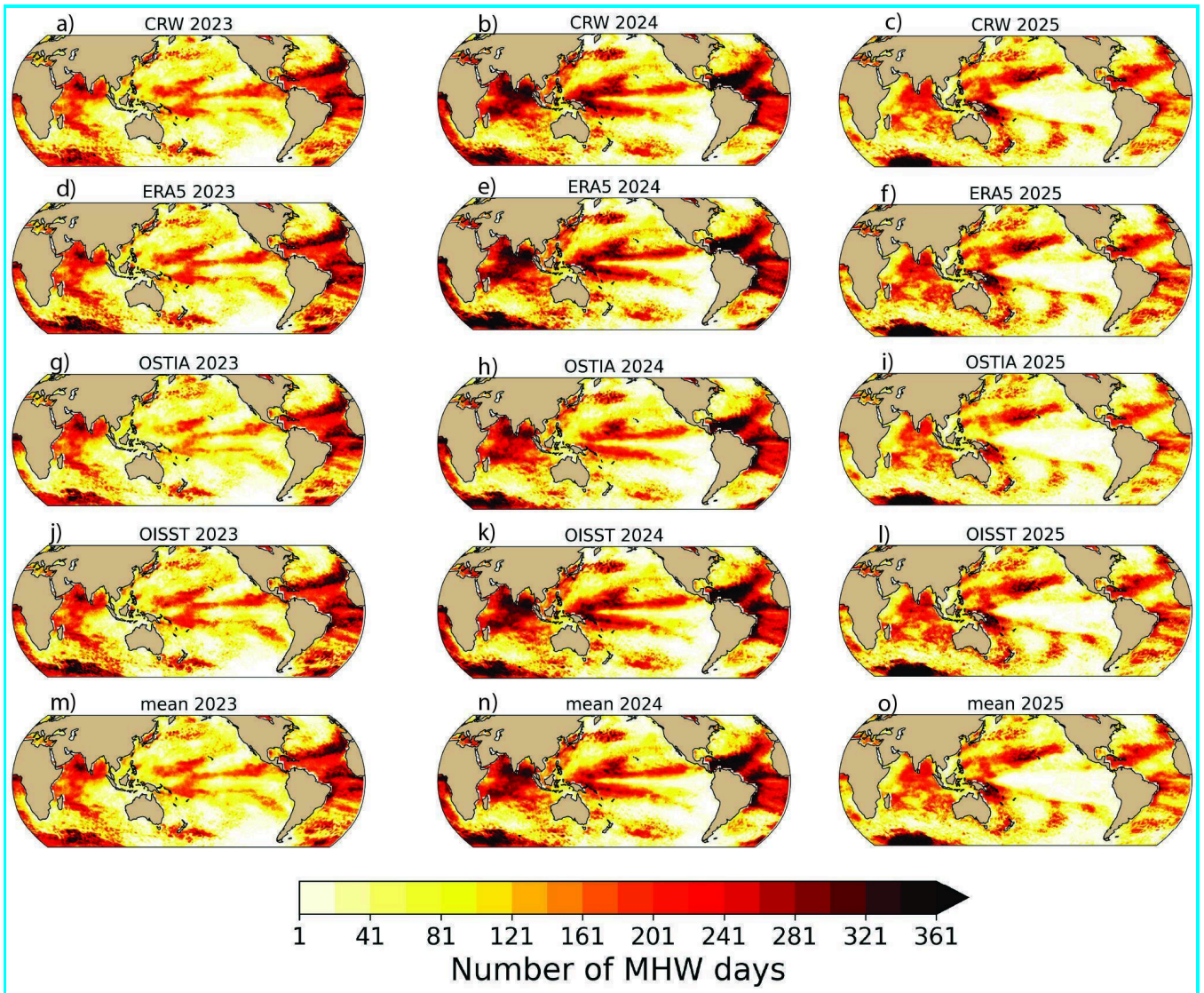


Figure S16 Annual number of MHW days in 2023, 2024 and 2025 from the four datasets: (a-c) NOAA's CRW, (d-f) ERA5, (g-i) OSTIA and (k-l) NOAA's OISST v2.1 , and (m-o) the mean of these.

## S11. Global land precipitation

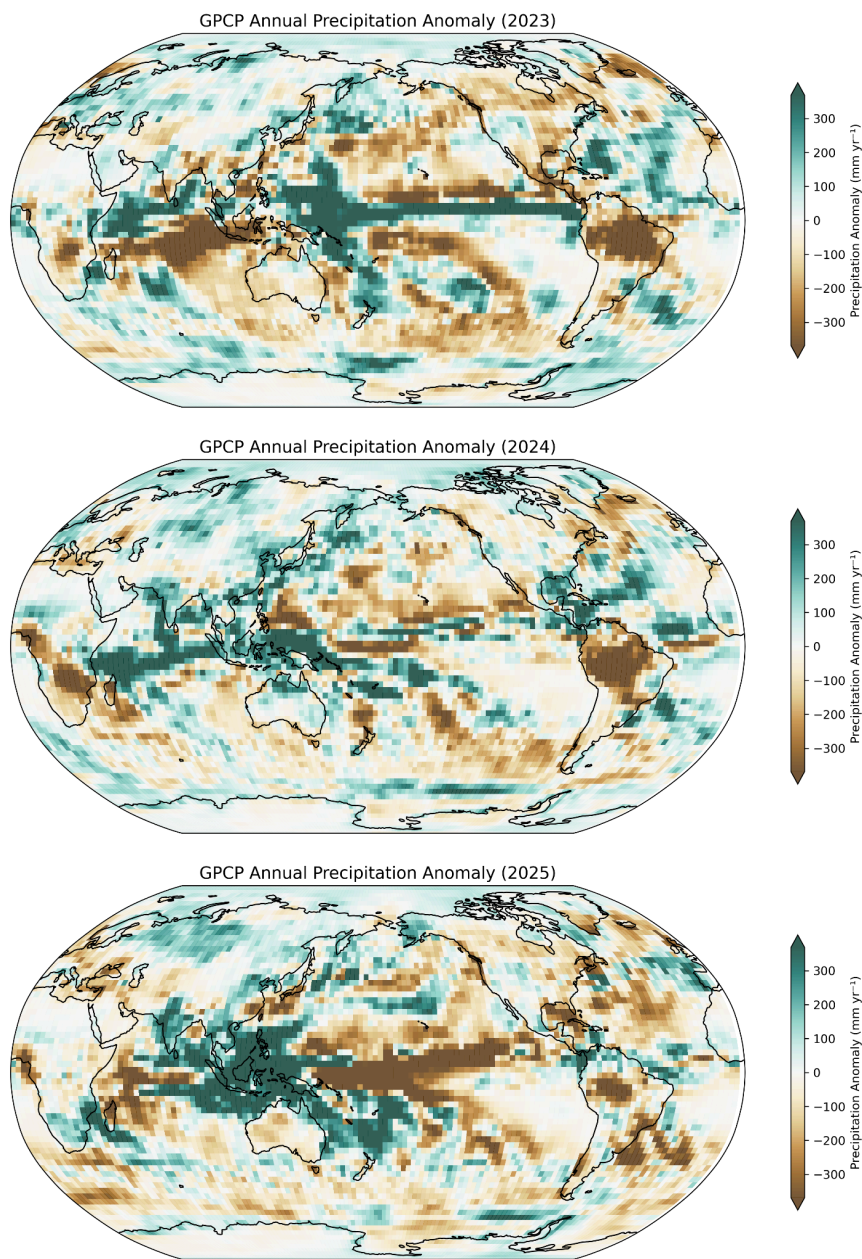


Figure S17 Anomaly of annual precipitation in 2023, 2024, and 2025 relative to 1990-2010 climatology, obtained from GPCP V2.3.

## S14. Discussion

**Table S13 Participants at GCOS February 2026 expert meeting on observational data risks.**

Experts group			
GCOS	Germany	Stephan	Bojinski
GCOS	UK	Richard	Cornes
GCOS	Spain	Carmen	García Izquierdo
GCOS	United States	Steven J.	Goodman
GCOS	Japan	Hironobu	Iwabuchi
GCOS	UK	Elizabeth	Kent
GCOS	South Korea	Meehye	Lee
GCOS	South Africa	Charlotte	Mc Bride
GCOS	UK	Colin	Morice
GCOS	Germany	Paul	Poli
GCOS	Sweden	Martin	Ridal
GCOS	Germany	Elke	Rustemeier
GCOS	Austria	Andreas	Steiner
GCOS	Australia	Blair	Trewin
GCOS	Brazil	Ronald	Buss de Souza
GCOS	China	Lijing	Cheng
GCOS	United Stated	Meghan	Cronin
GCOS	Spain	Mélanie	Juza
GCOS	Germany	Stefan	Kern
GCOS	United States	Tony	Lee
GCOS	South Africa	Tamaryn	Morris
GCOS	Fiji	Bipendra	Prakash
GCOS	Italy	Katrin	Schroeder
GCOS	France	Sabrina	Speich
GCOS	France	Karina	Von Schuckmann
GCOS	China	Weidong	Yu
GCOS	UK	Hao	Zuo

GCOS	United Republic of Tanzania	Nyambilila Abdallah	Amuri
GCOS	Spain	Emilio	Chuvieco
GCOS	Austria	Wöuter	Dorigo
GCOS	Italy	Claudia	Giardino
GCOS	Italy	Nadine	Gobron
GCOS	Germany	Andreas	Güntner
GCOS	Italy	Matieu	Henry
GCOS	Germany	Martin	Herold
GCOS	New Zealand	Christina	Hulbe
GCOS	China	Li	Jia
GCOS	Germany	Simon	Mischel
GCOS	The Netherlands	Claudia Andrea	Ruz Vargas
Others	Germany	Ulrich	Bundke
Others	Netherlands	Marta	Gutiérrez David
Others	Finland	Anca	Hienola
Others	Norway	Cathrine	Lund Myhre
Others	Sweden	Alex	Vermeulen
Others	Netherlands	Tomislav	Hengl
Others	France	Lionel	Menard
Others	Poland	Artur	Palacz
Others	England	Nicholas	Pepin
Others	Denmark	Jose Miguel	Rubio Iglesias
Others	England	Maria	Shahgedanova
GCOS Secretariat			
Director	Switzerland	Albert	Fischer
Officer	Switzerland	Caterina	Tassone
Officer	Switzerland	Antonio	Bombelli
Officer	Switzerland	Belén	Martín Míguez
Network Manager	United Kingdom	Tim	Oakley

## References

- Adusumilli, S., Straneo, F., Hendricks, S., Korosov, A., Lavergne, T., Lawrence, I., Marzeion, B., Otosaka, I., Schweiger, A., Shepherd, A., Slater, D., Slater, T., Timmermanns, M.-L., and Zemp, M.: GCOS EHI 1960-2020 Cryosphere Heat Content, [https://doi.org/10.26050/WDCC/GCOS\\_EHI\\_1960-2020\\_CRHC](https://doi.org/10.26050/WDCC/GCOS_EHI_1960-2020_CRHC), 2022.
- Allan ,R.P. and Merchant, C.J.: Reconciling Earth's growing energy imbalance with ocean warming, *Environ. Res. Lett*, 20 04402, <https://doi.org/10.1088/1748-9326/adb448>, 2025.
- Allen, M. R. and Stott, P. A.: Estimating signal amplitudes in optimal fingerprinting, part I: theory, *Climate Dynamics*, 21, 477–491, <https://doi.org/10.1007/s00382-003-0313-9>, 2003.
- Allen, M. R., O. P. Dube, W. Solecki, F. Aragón-Durand, W. Cramer, S. Humphreys, M. Kainuma, J. Kala, N. Mahowald, Y. Mulugetta, R. Perez, M. Wairiu, and K. Zickfeld, 2018: Framing and Context. In: *Global Warming of 1.5°C. An IPCC Special Report on the impacts of global warming of 1.5°C above pre-industrial levels and related global greenhouse gas emission pathways, in the context of strengthening the global response to the threat of climate change, sustainable development, and efforts to eradicate poverty* [Masson-Delmotte, V., P. Zhai, H.-O. Pörtner, D. Roberts, J. Skea, P.R. Shukla, A. Pirani, W. Moufouma-Okia, C. Péan, R. Pidcock, S. Connors, J.B.R. Matthews, Y. Chen, X. Zhou, M.I. Gomis, E. Lonnoy, T. Maycock, M. Tignor, and T. Waterfield (eds.)], Cambridge University Press, Cambridge, UK and New York, NY, USA, 49-92, <https://doi.org/10.1017/9781009157940.003>, 2018.
- Angelakis, A.N.; Zaccaria, D.; Krasilnikoff, J.; Salgot, M.; Bazza, M.; Roccaro, P.; Jimenez, B.; Kumar, A.; Yinghua, W.; Baba, A.; et al. Irrigation of World Agricultural Lands: Evolution through the Millennia. *Water*, 12, 1285. <https://doi.org/10.3390/w12051285>, 2020
- APARC: The Hunga Volcanic Eruption Atmospheric Impacts Report. Yunqian Zhu, Graham Mann, Paul A. Newman, and William Randel (Eds.), APARC Report No. 11, WCRP-10/2025, doi: 10.34734/FZJ-2025-05237, available at [www.aparc-climate.org/publications/](http://www.aparc-climate.org/publications/), 2025
- Bednarz, E. M., Butler, A. H., Wang, X., Zhuo, Z., Yu, W., Stenchikov, G., Toohey, M., and Zhu, Y.: Indirect climate impacts of the Hunga eruption, *Atmos. Chem. Phys.*, 26, 197–215, <https://doi.org/10.5194/acp-26-197-2026>, 2026.
- Beusch, L., Gudmundsson, L., and Seneviratne, S. I.: Emulating Earth system model temperatures with MESMER: from global mean temperature trajectories to grid-point-level realizations on land, *Earth Syst. Dynam.*, 11, 139–159, <https://doi.org/10.5194/esd-11-139-2020>, 2020.

Cattiaux, J., Ribes, A., and Cariou, E.: How Extreme Were Daily Global Temperatures in 2023 and Early 2024?, *Geophysical Research Letters*, 51, e2024GL110531, <https://doi.org/10.1029/2024GL110531>, 2024.

Chan, D., Chan, S. C., Siddons, J. T., Cable, A., Faulkner, A., Cornes, R. C., Kent, E. C., Gebbie, G., and Huybers, P.: DCENT-I: A Globally Infilled Extension of the Dynamically Consistent ENsemble of Temperature Dataset, *Geoscience Data Journal*, 13, e70054, <https://doi.org/10.1002/gdj3.70054>, 2026.

Chen, L., Xu, W., Zhou, Z., Cao, L., Yang, S., and Xu, C.: A new global land–ocean merged surface temperature dataset since the 1850s: the CMA-GMST dataset, *Climate Dynamics*, 63, 187, <https://doi.org/10.1007/s00382-025-07614-x>, 2025.

Chen, D., M. Rojas, B. H. Samset, K. Cobb, A. Diongue Niang, P. Edwards, S. Emori, S. H. Faria, E. Hawkins, P. Hope, P. Huybrechts, M. Meinshausen, S. K. Mustafa, G.-K. Plattner, and A.-M. Tréguier, 2021: Framing, Context, and Methods. In *Climate Change 2021: The Physical Science Basis. Contribution of Working Group I to the Sixth Assessment Report of the Intergovernmental Panel on Climate Change* [Masson-Delmotte, V., P. Zhai, A. Pirani, S. L. Connors, C. Péan, S. Berger, N. Caud, Y. Chen, L. Goldfarb, M. I. Gomis, M. Huang, K. Leitzell, E. Lonnoy, J. B. R. Matthews, T. K. Maycock, T. Waterfield, O. Yelekçi, R. Yu, and B. Zhou (eds.)]. Cambridge University Press, Cambridge, United Kingdom and New York, NY, USA, pp. 147–286, <https://doi.org/10.1017/9781009157896.003>, 2021.

Cheng, L., Trenberth, K. E., Fasullo, J., Boyer, T., Abraham, J., and Zhu, J.: Improved estimates of ocean heat content from 1960 to 2015, *Sci. Adv.*, 3, e1601545, <https://doi.org/10.1126/sciadv.1601545>, 2017.

Chini, L., Hurtt, G., Sahajpal, R., Frohking, S., Klein Goldewijk, K., Sitch, S., Ganzenmüller, R., Ma, L., Ott, L., Pongratz, J., and Poulter, B.: Land-use harmonization datasets for annual global carbon budgets, *Earth Syst. Sci. Data*, 13, 4175–4189, <https://doi.org/10.5194/essd-13-4175-2021>, 2021.

Cowtan, K. and Way, R. G.: Coverage bias in the HadCRUT4 temperature series and its impact on recent temperature trends, *Q.J.R. Meteorol. Soc.*, 140, 1935–1944, <https://doi.org/10.1002/qj.2297>, 2014.

Collins M., M. Sutherland, L. Bouwer, S.-M. Cheong, T. Frölicher, H. Jacot Des Combes, M. Koll Roxy, I. Losada, K. McInnes, B. Ratter, E. Rivera-Arriaga, R.D. Susanto, D. Swingedouw, and L. Tibig, 2019: Extremes, Abrupt Changes and Managing Risk. In: *IPCC Special Report on the Ocean and Cryosphere in a Changing Climate* [H.-O. Pörtner, D.C. Roberts, V. Masson-Delmotte, P. Zhai, M. Tignor, E. Poloczanska, K. Mintenbeck, A. Alegría, M. Nicolai, A. Okem, J. Petzold, B. Rama, N.M. Weyer (eds.)]. Cambridge University Press, Cambridge, UK and New York, NY, USA, pp. 589–655. <https://doi.org/10.1017/9781009157964.008>, 2019.

Cowtan, K., Hausfather, Z., Hawkins, E., Jacobs, P., Mann, M. E., Miller, S. K., Steinman, B. A., Stolpe, M. B., and Way, R. G.: Robust comparison of climate models with observations using blended land air and ocean sea surface temperatures, *Geophys. Res. Lett.*, 42, 6526–6534, <https://doi.org/10.1002/2015GL064888>, 2015.

Crippa, M., Guizzardi, D., Pagani, F., Banja, M., Muntean, M., Schaaf, E., Becker, W., Monforti-Ferrario, F., Quadrelli, R., Risquez Martin, A., Taghavi-Moharamli, P., Grassi, G., Rossi, S., Brandao De Melo, J., Oom, D., Branco, A., San-Miguel, J., and Vignati, E.: GHG emissions of all world countries, Publications Office of the European Union, <https://doi:10.2760/9816914> [data set], 2025.

Cuesta-Valero, F. J., García-García, A., Beltrami, H., González-Rouco, J. F., and García-Bustamante, E.: Long-term global ground heat flux and continental heat storage from geothermal data, *Clim. Past*, 17, 451–468, <https://doi.org/10.5194/cp-17-451-2021>, 2021.

Cuesta-Valero, F. J., Beltrami, H., García-García, A., Krinner, G., Langer, M., MacDougall, A. H., Nitzbon, J., Peng, J., von Schuckmann, K., Seneviratne, S. I., Smith, N., Thiery, W., Vanderkelen, I., and Wu, T.: Continental heat storage: Contributions from ground, inland waters, and permafrost thawing, *Earth Syst. Dynam. Discuss.* [preprint], <https://doi.org/10.5194/esd-2022-32>, 2023.

Dessler, A. E., Schoeberl, M. R., Wang, T., Davis, S. M., Rosenlof, K. H., and Vernier, J.-P.: Variations of stratospheric water vapor over the past three decades, *J. Geophys. Res.-Atmos.*, 119, 12588–12598, <https://doi.org/10.1002/2014JD021712>, 2014.

Dhomse, S. S., Mann, G. W., Antuña Marrero, J. C., Shallcross, S. E., Chipperfield, M. P., Carslaw, K. S., Marshall, L., Abraham, N. L., and Johnson, C. E.: Evaluating the simulated radiative forcings, aerosol properties, and stratospheric warmings from the 1963 Mt Agung, 1982 El Chichón, and 1991 Mt Pinatubo volcanic aerosol clouds, *Atmos. Chem. Phys.*, 20, 13627–13654, <https://doi.org/10.5194/acp-20-13627-2020>, 2020.

Domingues, C. M., Church, J. A., White, N. J., Gleckler, P. J., Wijffels, S. E., Barker, P. M., and Dunn, J. R.: Improved estimates of upper-ocean warming and multi-decadal sea-level rise, *Nature*, 453, 1090–1093, <https://doi.org/10.1038/nature07080>, 2008.

Dorgeist, L., Schwingshackl, C., Bultan, S., Pongratz, J. : A consistent budgeting of terrestrial carbon fluxes. *Nat Commun* 15, 7426 (2024). <https://doi.org/10.1038/s41467-024-51126-x>

Dunn, R. J. H., Alexander, L. V., Donat, M. G., Zhang, X., Bador, M., Herold, N., et al. Development of an updated global land in situ-based dataset of temperature and precipitation extremes: HadEX3, *J. Geophys. Res.-Atmos.*, 125, e2019JD032263, <https://doi.org/10.1029/2019JD032263R>, 2020.

Durack, P. J., Naik, V., Nicholls, Z., O'Rourke, E., Turner, B., Buontempo, C., Brookshaw, A., Goddard, C., MacIntosh, C., Hewitt, H., & Dunne, J. P. : Earth system forcing for CMIP7 and beyond (1.1). Zenodo. <https://doi.org/10.5281/zenodo.15469219>. 2025.

Dutton, G.S., B. D. Hall, S.A. Montzka, J. D. Nance, S. D. Clingan, K. M. Petersen, Combined Atmospheric Chlorofluorocarbon-12 Dry Air Mole Fractions from the NOAA GML Halocarbons Sampling Network, 1977-2024, Version: 2024-03-07, <https://doi.org/10.15138/PJ63-H440>, 2024.

Etminan, M., Myhre, G., Highwood, E. J., and Shine, K. P.: Radiative forcing of carbon dioxide, methane, and nitrous oxide: A significant revision of the methane radiative forcing, *Geophys. Res. Lett.*, 43, 12614-12623, <https://doi.org/10.1002/2016GL071930>, 2016.

Eyring, V., N. P. Gillett, K.M. Achuta Rao, R. Barimalala, M. Barreiro Parrillo, N. Bellouin, C. Cassou, P. J. Durack, Y. Kosaka, S. McGregor, S. Min, O. Morgenstern, and Y. Sun: Human Influence on the Climate System. In *Climate Change 2021: The Physical Science Basis. Contribution of Working Group I to the Sixth Assessment Report of the Intergovernmental Panel on Climate Change* [Masson-Delmotte, V., P. Zhai, A. Pirani, S.L. Connors, C. Péan, S. Berger, N. Caud, Y. Chen, L. Goldfarb, M.I. Gomis, M. Huang, K. Leitzell, E. Lonnoy, J.B.R. Matthews, T.K. Maycock, T. Waterfield, O. Yelekçi, R. Yu, and B. Zhou (eds.)]. Cambridge University Press, Cambridge, United Kingdom and New York, NY, USA, pp. 423–552, <http://doi:10.1017/9781009157896.005>, 2021.

FAO: FAOSTAT: Land Use. <https://www.fao.org/faostat/en/#data/RL>. Licence: CC-BY-4.0. Download: <https://doi.org/10.4060/cd2971en-fig08>, 2025

Fiore, A. M., Dentener, F. J., Wild, O., Cuvelier, C., Schultz, M. G., Hess, P., Textor, C., Schulz, M., Doherty, R. M., Horowitz, L. W., MacKenzie, I. A., Sanderson, M. G., Shindell, D. T., Stevenson, D. S., Szopa, S., Van Dingenen, R., Zeng, G., Atherton, C., Bergmann, D., Bey, I., Carmichael, G., Collins, W. J., Duncan, B. N., Faluvegi, G., Folberth, G., Gauss, M., Gong, S., Hauglustaine, D., Holloway, T., Isaksen, I. S. A., Jacob, D. J., Jonson, J. E., Kamber, J. W., Keating, T. J., Lupu, A., Marmer, E., Montanaro, V., Park, R. J., Pitari, G., Pringle, K. J., Pyle, J. A., Schroeder, S., Vivanco, M. G., Wind, P., Wojcik, G., Wu, S., and Zuber, A.: Multimodel estimates of intercontinental source-receptor relationships for ozone pollution, *J. Geophys. Res.*, 114, D04301, <https://doi.org/10.1029/2008JD010816>, 2009.

Forster, P., T. Storelvmo, K. Armour, W. Collins, J.-L. Dufresne, D. Frame, D.J. Lunt, T. Mauritsen, M.D. Palmer, M. Watanabe, M. Wild, and H. Zhang, 2021: The Earth's Energy Budget, Climate Feedbacks, and Climate Sensitivity. In *Climate Change 2021: The Physical Science Basis. Contribution of Working Group I to the Sixth Assessment Report of the Intergovernmental Panel on Climate Change* [Masson-Delmotte, V., P. Zhai, A. Pirani, S.L. Connors, C. Péan, S. Berger, N. Caud, Y. Chen, L. Goldfarb, M.I. Gomis, M. Huang, K. Leitzell, E. Lonnoy, J.B.R. Matthews, T.K. Maycock, T. Waterfield, O. Yelekçi, R. Yu, and B. Zhou (eds.)]. Cambridge University Press, Cambridge, United Kingdom and New York, NY, USA, pp. 923–1054, <https://doi.org/10.1017/9781009157896.009>, 2021.

Forster, P. M., Smith, C. J., Walsh, T., Lamb, W. F., Lamboll, R., Hauser, M., Ribes, A., Rosen, D., Gillett, N., Palmer, M. D., Rogelj, J., von Schuckmann, K., Seneviratne, S. I., Trewin, B., Zhang, X., Allen, M., Andrew, R., Birt, A., Borger, A., Boyer, T., Broersma, J. A., Cheng, L., Dentener, F., Friedlingstein, P., Gutiérrez, J. M., Gütschow, J., Hall, B., Ishii, M., Jenkins, S., Lan, X., Lee, J.-Y., Morice, C., Kadow, C., Kennedy, J., Killick, R., Minx, J. C., Naik, V., Peters, G. P., Pirani, A., Pongratz, J., Schleussner, C.-F., Szopa, S., Thorne, P., Rohde, R., Rojas Corradi, M., Schumacher, D., Vose, R., Zickfeld, K., Masson-Delmotte, V., and Zhai, P.: Indicators of Global Climate Change 2022: annual update of large-scale indicators of the state of the climate system and human influence, *Earth Syst. Sci. Data*, 15, 2295–2327, <https://doi.org/10.5194/essd-15-2295-2023>, 2023.

Forster, P. M., Smith, C., Walsh, T., Lamb, W. F., Lamboll, R., Hall, B., Hauser, M., Ribes, A., Rosen, D., Gillett, N. P., Palmer, M. D., Rogelj, J., Von Schuckmann, K., Trewin, B., Allen, M., Andrew, R., Betts, R. A., Borger, A., Boyer, T., Broersma, J. A., Buontempo, C., Burgess, S., Cagnazzo, C., Cheng, L., Friedlingstein, P., Gettelman, A., Gütschow, J., Ishii, M., Jenkins, S., Lan, X., Morice, C., Mühle, J., Kadow, C., Kennedy, J., Killick, R. E., Krummel, P. B., Minx, J. C., Myhre, G., Naik, V., Peters, G. P., Pirani, A., Pongratz, J., Schleussner, C.-F., Seneviratne, S. I., Szopa, S., Thorne, P., Kovilakam, M. V. M., Majamäki, E., Jalkanen, J.-P., Van Marle, M., Hoesly, R. M., Rohde, R., Schumacher, D., Van Der Werf, G., Vose, R., Zickfeld, K., Zhang, X., Masson-Delmotte, V., and Zhai, P.: Indicators of Global Climate Change 2023: annual update of key indicators of the state of the climate system and human influence, *Earth Syst. Sci. Data*, 16, 2625–2658, <https://doi.org/10.5194/essd-16-2625-2024>, 2024.

Forster, P. M., Smith, C., Walsh, T., Lamb, W. F., Lamboll, R., Cassou, C., Hauser, M., Hausfather, Z., Lee, J.-Y., Palmer, M. D., von Schuckmann, K., Slangen, A. B. A., Szopa, S., Trewin, B., Yun, J., Gillett, N. P., Jenkins, S., Matthews, H. D., Raghavan, K., Ribes, A., Rogelj, J., Rosen, D., Zhang, X., Allen, M., Aleluia Reis, L., Andrew, R. M., Betts, R. A., Borger, A., Broersma, J. A., Burgess, S. N., Cheng, L., Friedlingstein, P., Domingues, C. M., Gambarini, M., Gasser, T., Gütschow, J., Ishii, M., Kadow, C., Kennedy, J., Killick, R. E., Krummel, P. B., Liné, A., Monselesan, D. P., Morice, C., Mühle, J., Naik, V., Peters, G. P., Pirani, A., Pongratz, J., Minx, J. C., Rigby, M., Rohde, R., Savita, A., Seneviratne, S. I., Thorne, P., Wells, C., Western, L. M., van der Werf, G. R., Wijffels, S. E., Masson-Delmotte, V., and Zhai, P.: Indicators of Global Climate Change 2024: annual update of key indicators of the state of the climate system and human influence, *Earth Syst. Sci. Data*, 17, 2641–2680, <https://doi.org/10.5194/essd-17-2641-2025>, 2025.

Foster, G., & Rahmstorf, S.: Global warming has accelerated significantly. *Geophysical Research Letters*, 53, e2025GL118804. <https://doi.org/10.1029/2025GL118804>, 2026

Fox-Kemper, B., Fox-Kemper, B., H. T. Hewitt, C. Xiao, G. Aðalgeirsdóttir, S.S. Drijfhout, T. L. Edwards, N. R. Golledge, M. Hemer, R. E. Kopp, G. Krinner, A. Mix, D. Notz, S. Nowicki, I. S. Nurhati, L. Ruiz, J.-B. Sallée, A. B. A. Slangen, and

Y. Yu: Ocean, Cryosphere and Sea Level Change. In *Climate Change 2021: The Physical Science Basis. Contribution of Working Group I to the Sixth Assessment Report of the Intergovernmental Panel on Climate Change* [Masson-Delmotte, V., P. Zhai, A. Pirani, S.L. Connors, C. Péan, S. Berger, N. Caud, Y. Chen, L. Goldfarb, M.I. Gomis, M. Huang, K. Leitzell, E. Lonnoy, J. B. R. Matthews, T. K. Maycock, T. Waterfield, O. Yelekçi, R. Yu, and B. Zhou (eds.)]. Cambridge University Press, Cambridge, United Kingdom and New York, NY, USA, pp. 1211–1362, <https://doi.org/10.1017/9781009157896.011>, 2021.

Fox-Kemper, B., Fox-Kemper, B., H. T. Hewitt, C. Xiao, G. Aðalgeirsdóttir, S.S. Drijfhout, T. L. Edwards, N. R. Golledge, M. Hemer, R. E. Kopp, G. Krinner, A. Mix, D. Notz, S. Nowicki, I. S. Nurhati, L. Ruiz, J.-B. Sallée, A. B. A. Slangen, and Y. Yu: Ocean, Cryosphere and Sea Level Change. In *Climate Change 2021: The Physical Science Basis. Contribution of Working Group I to the Sixth Assessment Report of the Intergovernmental Panel on Climate Change* [Masson-Delmotte, V., P. Zhai, A. Pirani, S.L. Connors, C. Péan, S. Berger, N. Caud, Y. Chen, L. Goldfarb, M.I. Gomis, M. Huang, K. Leitzell, E. Lonnoy, J. B. R. Matthews, T. K. Maycock, T. Waterfield, O. Yelekçi, R. Yu, and B. Zhou (eds.)]. Cambridge University Press, Cambridge, United Kingdom and New York, NY, USA, pp. 1211–1362, <https://doi.org/10.1017/9781009157896.011>, 2021.

Friedlingstein, P., O'Sullivan, M., Jones, M. W., Andrew, R. M., Hauck, J., Landschützer, P., Le Quéré, C., Li, H., Luijckx, I. T., Olsen, A., Peters, G. P., Peters, W., Pongratz, J., Schwingshackl, C., Sitch, S., Canadell, J. G., Ciais, P., Jackson, R. B., Alin, S. R., Arneeth, A., Arora, V., Bates, N. R., Becker, M., Bellouin, N., Berghoff, C. F., Bittig, H. C., Bopp, L., Cadule, P., Campbell, K., Chamberlain, M. A., Chandra, N., Chevallier, F., Chini, L. P., Colligan, T., Decayeux, J., Djeutchouang, L. M., Dou, X., Duran Rojas, C., Enyo, K., Evans, W., Fay, A. R., Feely, R. A., Ford, D. J., Foster, A., Gasser, T., Gehlen, M., Gkritzalis, T., Grassi, G., Gregor, L., Gruber, N., Gürses, Ö., Harris, I., Hefner, M., Heinke, J., Hurtt, G. C., Iida, Y., Ilyina, T., Jacobson, A. R., Jain, A. K., Jarníková, T., Jersild, A., Jiang, F., Jin, Z., Kato, E., Keeling, R. F., Klein Goldewijk, K., Knauer, J., Korsbakken, J. I., Lan, X., Lauvset, S. K., Lefèvre, N., Liu, Z., Liu, J., Ma, L., Maksyutov, S., Marland, G., Mayot, N., McGuire, P. C., Metzl, N., Monacchi, N. M., Morgan, E. J., Nakaoka, S.-I., Neill, C., Niwa, Y., Nützel, T., Olivier, L., Ono, T., Palmer, P. I., Pierrot, D., Qin, Z., Resplandy, L., Roobaert, A., Rosan, T. M., Rödenbeck, C., Schwinger, J., Smallman, T. L., Smith, S. M., Sospedra-Alfonso, R., Steinhoff, T., Sun, Q., Sutton, A. J., Séférian, R., Takao, S., Tatebe, H., Tian, H., Tilbrook, B., Torres, O., Tourigny, E., Tsujino, H., Tubiello, F., van der Werf, G., Wanninkhof, R., Wang, X., Yang, D., Yang, X., Yu, Z., Yuan, W., Yue, X., Zaehle, S., Zeng, N., and Zeng, J.: Global Carbon Budget 2024, *Earth Syst. Sci. Data*, 17, 965–1039, <https://doi.org/10.5194/essd-17-965-2025>, 2025.

Fueglistaler, S. and Haynes, P. H.: Control of interannual and longer-term variability of stratospheric water vapor, *J. Geophys. Res.*, 110, D24108, <https://doi.org/10.1029/2005JD006019>, 2005.

Funke, B., Dudok de Wit, T., Ermolli, I., Haberreiter, M., Kinnison, D., Marsh, D., Nesse, H., Seppälä, A., Sinnhuber, M., and Usoskin, I.: Towards the definition of a solar forcing dataset for CMIP7, *Geosci. Model Dev.*, 17, 1217–1227, <https://doi.org/10.5194/gmd-17-1217-2024>, 2024.

Gasser, T., Crepin, L., Quilcaille, Y., Houghton, R. A., Ciais, P., and Obersteiner, M.: Historical CO<sub>2</sub> emissions from land use and land cover change and their uncertainty, *Biogeosciences*, 17, 4075–4101, <https://doi.org/10.5194/bg-17-4075-2020>, 2020.

Gettelman, A., Christensen, M. A., Diamond, M. S., Gryspeerdt, E., Manshausen, P., Sieir, P., Watson-Parris, D., Yang, M., Yoshioka, M., and Yuan, T.: Has Reducing Ship Emissions Brought Forward Global Warming?, *Geophys. Res. Lett.*, 2024.

Ghimire, B., C. A. Williams, J. Masek, F. Gao, Z. Wang, C. Schaaf, and T. He: Global albedo change and radiative cooling from anthropogenic land cover change, 1700 to 2005 based on MODIS, land use harmonization, radiative kernels, and reanalysis, *Geophys. Res. Lett.*, 41, 9087–9096, doi:10.1002/2014GL061671, 2014.

Gillett, N. P., Shiogama, H., Funke, B., Hegerl, G., Knutti, R., Matthes, K., Santer, B. D., Stone, D., and Tebaldi, C.: The Detection and Attribution Model Intercomparison Project (DAMIP v1.0) contribution to CMIP6, *Geosci. Model Dev.*, 9, 3685–3697, <https://doi.org/10.5194/gmd-9-3685-2016>, 2016.

Gillett, N.P., Kirchmeier-Young, M., Ribes, A., Shiogama, H., Hegerl, G.C., Knutti, R., Gastineau, G., John, J.G., Li, L., Nazarenko, L., Rosenbloom, N., Seland, Ø., Wu, T., Yukimoto, S., and Ziehn, T.: Constraining human contributions to observed warming since the pre-industrial period, *Nat. Clim. Chang.*, 11, 207–212, <https://doi.org/10.1038/s41558-020-00965-9>, 2021.

Goessling, H. F., Rackow, T., and Jung, T.: Recent global temperature surge intensified by record-low planetary albedo, *Science*, 387, 68–73, <https://doi.org/10.1126/science.adq7280>, 2025.

Good, S. A., Martin, M. J., and Rayner, N. A.: EN4: Quality controlled ocean temperature and salinity profiles and monthly objective analyses with uncertainty estimates, THE EN4 DATA SET, *J. Geophys. Res.-Oceans*, 118, 6704–6716, <https://doi.org/10.1002/2013JC009067>, 2013.

Gulev, S. K., P. W. Thorne, J. Ahn, F. J. Dentener, C. M. Domingues, S. Gerland, D. Gong, D. S. Kaufman, H. C. Nnamchi, J. Quaas, J.A. Rivera, S. Sathyendranath, S.L. Smith, B. Trewin, K. von Schuckmann, and R. S. Vose: Changing State of the

Climate System. In *Climate Change 2021: The Physical Science Basis. Contribution of Working Group I to the Sixth Assessment Report of the Intergovernmental Panel on Climate Change*[Masson-Delmotte, V., P. Zhai, A. Pirani, S.L. Connors, C. Péan, S. Berger, N. Caud, Y. Chen, L. Goldfarb, M.I. Gomis, M. Huang, K. Leitzell, E. Lonnoy, J.B.R. Matthews, T.K. Maycock, T. Waterfield, O. Yelekçi, R. Yu, and B. Zhou (eds.)]. Cambridge University Press, Cambridge, United Kingdom and New York, NY, USA, pp. 287–422, <https://doi.org/10.1017/9781009157896.004>, 2021.

Granier, C., Darras, S., Denier van der Gon, H., Doubalova, J., Elguindi, N., Galle, B., Gauss, M., Guevara, M., Jalkanen, J.-P., Kuenen, J., Liousse, C., Quack, B., Simpson, D., and Sindelarova, K.: The Copernicus Atmosphere Monitoring Service global and regional emissions (April 2019 version), <https://doi.org/10.24380/D0BN-KX16>, n.d, 2019.

Guinaldo, T., Cassou, C., Sallée, J.-B., and Liné, A.: Internal variability effect doped by climate change drove the 2023 marine heat extreme in the North Atlantic, *Commun Earth Environ*, 6, 291, <https://doi.org/10.1038/s43247-025-02197-1>, 2025.

Gupta, A. K., Mittal, T., Fauria, K. E., Bennartz, R., and Kok, J. F.: The January 2022 Hunga eruption cooled the southern hemisphere in 2022 and 2023, *Commun Earth Environ*, 6, 240, <https://doi.org/10.1038/s43247-025-02181-9>, 2025.

Gütschow, J., Busch, D., and Pflüger, M.: The PRIMAP-hist national historical emissions time series (1750-2024) v2.7, Zenodo [data set], <https://doi.org/10.5281/zenodo.17090760>, 2025.

Jalkanen, J.-P., Johansson, L., Kukkonen, J., Brink, A., Kalli, J., and Stipa, T.: Extension of an assessment model of ship traffic exhaust emissions for particulate matter and carbon monoxide, *Atmospheric Chemistry and Physics*, 12, 2641–2659, <https://doi.org/10.5194/acp-12-2641-2012>, 2012.

Jalkanen, J.-P., Johansson, L., and Kukkonen, J.: A comprehensive inventory of ship traffic exhaust emissions in the European sea areas in 2011, *Atmos. Chem. Phys.*, 16, 71–84, <https://doi.org/10.5194/acp-16-71-2016>, 2016.

Johansson, L., Jalkanen, J.-P., and Kukkonen, J.: Global assessment of shipping emissions in 2015 on a high spatial and temporal resolution, *Atmospheric Environment*, 167, 403–415, <https://doi.org/10.1016/j.atmosenv.2017.08.042>, 2017

Hansen, J. E., Kharecha, P., Sato, M., Tselioudis, G., Kelly, J., Bauer, S. E., ... Pokela, A.: Global Warming Has Accelerated: Are the United Nations and the Public Well-Informed? *Environment: Science and Policy for Sustainable Development*, 67(1), 6–44. <https://doi.org/10.1080/00139157.2025.2434494>, 2025

.

Hansis, E., Davis, S. J., and Pongratz, J.: Relevance of methodological choices for accounting of land use change carbon fluxes, *Global Biogeochemical Cycles*, 29, 1230–1246, <https://doi.org/10.1002/2014GB004997>, 2015.

Haustein, K., Allen, M. R., Forster, P. M., Otto, F. E. L., Mitchell, D. M., Matthews, H. D., and Frame, D. J.: A real-time Global Warming Index, *Sci Rep*, 7, 15417, <https://doi.org/10.1038/s41598-017-14828-5>, 2017.

Hersbach H., Bell, B., Berrisford, P. et al.: The ERA5 global reanalysis, *Quat. Jour. R. Met. Soc.*, 146:1999–2049, <https://doi.org/10.1002/qj.3803>, 2020.

Hodnebrog, Ø., Myhre, G., Kramer, R. J., Shine, K. P., Andrews, T., Faluvegi, G., Kasoar, M., Kirkevåg, A., Lamarque, J.-F., Mülmenstädt, J., Olivie, D., Samset, B. H., Shindell, D., Smith, C. J., Takemura, T., and Voulgarakis, A.: The effect of rapid adjustments to halocarbons and N<sub>2</sub>O on radiative forcing, *npj Clim. Atmos. Sci.*, 3, 43, <https://doi.org/10.1038/s41612-020-00150-x>, 2020a.

Hodnebrog, Ø., Aamaas, B., Fuglestedt, J. S., Marston, G., Myhre, G., Nielsen, C. J., et al.: Updated global warming potentials and radiative efficiencies of halocarbons and other weak atmospheric absorbers, *Rev. Geophys.*, 58, e2019RG000691, <https://doi.org/10.1029/2019RG000691>, 2020b.

Hodnebrog, Ø., Myhre, G., Jouan, C., Andrews, T., Forster, P. M., Jia, H., Loeb, N. G., Olivie, D. J. L., Paynter, D., Quaas, J., Raghuraman, S. P., and Schulz, M.: Recent reductions in aerosol emissions have increased Earth's energy imbalance, *Communications Earth & Environment*, 5, 166, <https://doi.org/10.1038/s43247-024-01324-8>, 2024.

Huang, B., Yin, X., Menne, M. J., Vose, R., & Zhang, H. (2022). Improvements to the Land Surface Air Temperature Reconstruction in NOAA GlobalTemp: An Artificial Neural Network Approach. *Artificial Intelligence for the Earth Systems*, 1(4), Article e220032, e220032. <https://doi.org/10.1175/AIES-D-22-0032.1>

Huang, B., Yin, X., Boyer, T., Liu, C., Menne, M., Rao, Y. D., Smith, T., Vose, R., and Zhang, H.-M.: Extended Reconstructed Sea Surface Temperature, Version 6 (ERSSTv6). Part I: An Artificial Neural Network Approach, *Journal of Climate*, 38, 1105–1121, <https://doi.org/10.1175/JCLI-D-23-0707.1>, 2025.

Hurst, D. F., Oltmans, S. J., Vömel, H., Rosenlof, K. H., Davis, S. M., Ray, E. A., Hall, E. G., and Jordan, A. F.: Stratospheric water vapor trends over Boulder, Colorado: Analysis of the 30 year Boulder record, *J. Geophys. Res.-Atmos.*, 116, <https://doi.org/10.1029/2010JD015065>, 2011.

Hurt, G. C., Chini, L., Sahajpal, R., Frohking, S., Bodirsky, B. L., Calvin, K., Doelman, J. C., Fisk, J., Fujimori, S., Klein Goldewijk, K., Hasegawa, T., Havlik, P., Heinemann, A., Humpenöder, F., Jungclaus, J., Kaplan, J. O., Kennedy, J., Krisztin, T., Lawrence, D., Lawrence, P., Ma, L., Mertz, O., Pongratz, J., Popp, A., Poulter, B., Riahi, K., Shevliakova, E., Stehfest, E., Thornton, P., Tubiello, F. N., van Vuuren, D. P., and Zhang, X.: Harmonization of global land use change and management for the period 850–2100 (LUH2) for CMIP6, *Geosci. Model Dev.*, 13, 5425–5464, <https://doi.org/10.5194/gmd-13-5425-2020>, 2020.

IATA: Global Outlook for Air Transport: Times of Turbulence, IATA, <http://www.iata.org/en/iata-repository/publications/economic-reports/global-outlook-for-air-transport-december-2024/>, 2024.

IEA: World oil statistics (Edition 2024), IEA Oil Information Statistics (database), <https://doi.org/10.1787/558987b9-en>, 2024 (accessed on 24 April 2024).

Ishii, M., Fukuda, Y., Hirahara, S., Yasui, S., Suzuki, T., and Sato, K.: Accuracy of Global Upper Ocean Heat Content Estimation Expected from Present Observational Data Sets, SOLA, 13, 163–167, <https://doi.org/10.2151/sola.2017-030>, 2017.

Jenkins, S., Smith, C., Allen, M., and Grainger, R.: Tonga eruption increases chance of temporary surface temperature anomaly above 1.5 °C, Nature Clim. Chang., 13, 127–129, <https://doi.org/10.1038/s41558-022-01568-2>, 2023.

Joshi, M. M. and Jones, G. S.: The climatic effects of the direct injection of water vapour into the stratosphere by large volcanic eruptions, Atmos. Chem. Phys., 9, 6109–6118, <https://doi.org/10.5194/acp-9-6109-2009>, 2009.

Jordan, G., & Henry, M.: IMO2020 regulations accelerate global warming by up to 3 years in UKESM1. Earth's Future, 12, e2024EF005011. <https://doi.org/10.1029/2024EF005011>, 2024.

Jungclaus, J. H., Bard, E., Baroni, M., Braconnot, P., Cao, J., Chini, L. P., Egorova, T., Evans, M., González-Rouco, J. F., Goosse, H., Hurrell, G. C., Joos, F., Kaplan, J. O., Khodri, M., Klein Goldewijk, K., Krivova, N., LeGrande, A. N., Lorenz, S. J., Luterbacher, J., Man, W., Maycock, A. C., Meinshausen, M., Moberg, A., Muscheler, R., Nehrbass-Ahles, C., Otto-Bliesner, B. I., Phipps, S. J., Pongratz, J., Rozanov, E., Schmidt, G. A., Schmidt, H., Schmutz, W., Schurer, A., Shapiro, A. I., Sigl, M., Smerdon, J. E., Solanki, S. K., Timmreck, C., Toohey, M., Usoskin, I. G., Wagner, S., Wu, C.-J., Yeo, K. L., Zanchettin, D., Zhang, Q., and Zorita, E.: The PMIP4 contribution to CMIP6 – Part 3: The last millennium, scientific objective, and experimental design for the PMIP4 past1000 simulations, Geosci. Model Dev., 10, 4005–4033, <https://doi.org/10.5194/gmd-10-4005-2017>, 2017.

Kadow, C., Hall, D. M., and Ulbrich, U.: Artificial intelligence reconstructs missing climate information, Nat. Geosci., 13, 408–413, <https://doi.org/10.1038/s41561-020-0582-5>, 2020.

Kadow, C., Plésiat, É., and Lenssen, N.: Annual update of Climate Reconstruction AI (CRAI) infilled HadCRUT5 of near-surface temperature change 1850 to 2024 [Data set]. Zenodo. <https://doi.org/10.5281/zenodo.15622091>, 2025.

Keeble, J., Hassler, B., Banerjee, A., Checa-Garcia, R., Chiodo, G., Davis, S., Eyring, V., Griffiths, P. T., Morgenstern, O., Nowack, P., Zeng, G., Zhang, J., Bodeker, G., Burrows, S., Cameron-Smith, P., Cugnet, D., Danek, C., Deushi, M., Horowitz, L. W., Kubin, A., Li, L., Lohmann, G., Michou, M., Mills, M. J., Nabat, P., Olivié, D., Park, S., Seland, Ø., Stoll,

J., Wieners, K.-H., and Wu, T.: Evaluating stratospheric ozone and water vapour changes in CMIP6 models from 1850 to 2100, *Atmos. Chem. Phys.*, 21, 5015–5061, <https://doi.org/10.5194/acp-21-5015-2021>, 2021.

Klein Goldewijk, K., Beusen, A., Doelman, J., and Stehfest, E.: Anthropogenic land-use estimates for the Holocene; HYDE 3.2, *Earth Syst. Sci. Data*, 9, 927–953, 2017. <https://doi.org/10.5194/essd-9-1-2017>, 2017.

Kovilakam, M., Thomason, L. W., Ernest, N., Rieger, L., Bourassa, A., and Millán, L.: The Global Space-based Stratospheric Aerosol Climatology (version 2.0): 1979–2018, *Earth Syst. Sci. Data*, 12, 2607–2634, <https://doi.org/10.5194/essd-12-2607-2020>, 2020.

Lamb, W. F., Andrew, R. M., Jones, M., Nicholls, Z., Peters, G. P., Smith, C., Saunio, M., Grassi, G., Pongratz, J., Smith, S. J., Tubiello, F. N., Crippa, M., Gidden, M., Friedlingstein, P., Minx, J., and Forster, P. M.: Differences in anthropogenic greenhouse gas emissions estimates explained, *Earth System Science Data*, 18, 2549–2572, <https://doi.org/10.5194/essd-18-2549-2026>, 2026.

Lamboll, R. D., Nicholls, Z. R. J., Smith, C. J., Kikstra, J. S., Byers, E., and Rogelj, J.: Assessing the size and uncertainty of remaining carbon budgets, *Nature Climate Change*, 13, 1360–1367, <https://doi.org/10.1038/s41558-023-01848-5>, 2023.

Lan, X., Tans, P. and Thoning, K.W.: Trends in globally-averaged CO<sub>2</sub> determined from NOAA Global Monitoring Laboratory measurements, Version Monday, 14-Apr-2025 09:08:57 MDT <https://doi.org/10.15138/9N0H-ZH07>, 2025.

Laufkötter, C., Zscheischler, J., and Frölicher, T. L.: High-impact marine heatwaves attributable to human-induced global warming, *Science*, 369, 6511, <https://doi.org/10.1126/science.aba0690>, 2020.

Leach, N. J., Jenkins, S., Nicholls, Z., Smith, C. J., Lynch, J., Cain, M., Walsh, T., Wu, B., Tsutsui, J., and Allen, M. R.: FalRv2.0.0: a generalized impulse response model for climate uncertainty and future scenario exploration, *Geosci. Model Dev.*, 14, 3007–3036, <https://doi.org/10.5194/gmd-14-3007-2021>, 2021.

Lee, D. S., Fahey, D. W., Skowron, A., Allen, M. R., Burkhardt, U., Chen, Q., Doherty, S. J., Freeman, S., Forster, P. M., Fuglestedt, J., Gettelman, A., León, R. R. D., Lim, L. L., Lund, M. T., Millar, R. J., Owen, B., Penner, J. E., Pitari, G., Prather, M. J., Sausen, R., and Wilcox, L. J.: The contribution of global aviation to anthropogenic climate forcing for 2000 to 2018, *Atmos. Environ.*, 244, 117834, <https://doi.org/10.1016/j.atmosenv.2020.117834>, 2021.

Lee, J.-Y., J. Marotzke, G. Bala, L. Cao, S. Corti, J.P. Dunne, F. Engelbrecht, E. Fischer, J.C. Fyfe, C. Jones, A. Maycock, J. Mutemi, O. Ndiaye, S. Panickal, and T. Zhou: Future Global Climate: Scenario-Based Projections and Near-Term Information. In *Climate Change 2021: The Physical Science Basis. Contribution of Working Group I to the Sixth Assessment Report of the Intergovernmental Panel on Climate Change*[Masson-Delmotte, V., P. Zhai, A. Pirani, S.L. Connors, C. Péan, S. Berger, N. Caud, Y. Chen, L. Goldfarb, M.I. Gomis, M. Huang, K. Leitzell, E. Lonnoy, J.B.R.

Matthews, T.K. Maycock, T. Waterfield, O. Yelekçi, R. Yu, and B. Zhou (eds.)). Cambridge University Press, Cambridge, United Kingdom and New York, NY, USA, pp. 553–672, <https://doi.org/10.1017/9781009157896.006>, 2021.

Lee, H., K. Calvin, D. Dasgupta, G. Krinner, A. Mukherji, P. Thorne, C. Trisos, J. Romero, P. Aldunce, K. Barrett, G. Blanco, W.W.L. Cheung, S.L. Connors, F. Denton, A. Diongue-Niang, D. Dodman, M. Garschagen, O. Geden, B. Hayward, C. Jones, F. Jotzo, T. Krug, R. Lasco, J.-Y. Lee, V. Masson-Delmotte, M. Meinshausen, K. Mintenbeck, A. Mokssit, F.E.L. Otto, M. Pathak, A. Pirani, E. Poloczanska, H.-O. Pörtner, A. Revi, D.C. Roberts, J. Roy, A.C. Ruane, J. Skea, P.R. Shukla, R. Slade, A. Slangen, Y. Sokona, A.A. Sörensson, M. Tignor, D. van Vuuren, Y.-M. Wei, H. Winkler, P. Zhai, and Z. Zommers: Synthesis Report of the IPCC Sixth Assessment Report (AR6): Summary for Policymakers. Intergovernmental Panel on Climate Change [accepted], available at <https://www.ipcc.ch/report/ar6/syr/>, 2023.

Lenssen, N. J. L., Schmidt, G. A., Hansen, J. E., Menne, M. J., Persin, A., Ruedy, R., and Zyss, D.: Improvements in the GISTEMP Uncertainty Model, *J. Geophys. Res.-Atmos.*, 124, 6307–6326, <https://doi.org/10.1029/2018JD029522>, 2019.

Levitus, S., Antonov, J. I., Boyer, T. P., Baranova, O. K., Garcia, H. E., Locarnini, R. A., Mishonov, A. V., Reagan, J. R., Seidov, D., Yarosh, E. S., and Zweng, M. M.: World ocean heat content and thermosteric sea level change (0–2000 m), 1955–2010, *Geophys. Res. Lett.*, 39, <https://doi.org/10.1029/2012GL051106>, 2012.

Matthes, K., Funke, B., Andersson, M. E., Barnard, L., Beer, J., Charbonneau, P., Clilverd, M. A., Dudok de Wit, T., Haberleiter, M., Hendry, A., Jackman, C. H., Kretzschmar, M., Kruschke, T., Kunze, M., Langematz, U., Marsh, D. R., Maycock, A. C., Misios, S., Rodger, C. J., Scaife, A. A., Seppälä, A., Shangguan, M., Sinnhuber, M., Tourpali, K., Usoskin, I., van de Kamp, M., Verronen, P. T., and Versick, S.: Solar forcing for CMIP6 (v3.2), *Geosci. Model Dev.*, 10, 2247–2302, <https://doi.org/10.5194/gmd-10-2247-2017>, 2017.

Melo, J., Rossi, S., Achard, F., Alkama, R., Canadell, J. G., Friedlingstein, P., Gibbs, D., Harris, N., Heinrich, V., O’Sullivan, M., Peters, G., Pongratz, J., Rose, M., Roman-Cuesta, R., Sanz Sanchez, M. J., Schwingshackl, C., Sitch, S., and Grassi, G.: The LULUCF data hub: translating global land use emissions estimates into the national GHG inventory framework (Version 3.0, 2025 NGHGI release) (3.0), Zenodo [data set], <https://doi.org/10.5281/zenodo.17153438>, 2025.

Meinshausen, M., Nicholls, Z. R. J., Lewis, J., Gidden, M. J., Vogel, E., Freund, M., Beyerle, U., Gessner, C., Nauels, A., Bauer, N., Canadell, J. G., Daniel, J. S., John, A., Krummel, P. B., Luderer, G., Meinshausen, N., Montzka, S. A., Rayner, P. J., Reimann, S., Smith, S. J., van den Berg, M., Velders, G. J. M., Vollmer, M. K., and Wang, R. H. J.: The shared socio-economic pathway (SSP) greenhouse gas concentrations and their extensions to 2500, *Geosci. Model Dev.*, 13, 3571–3605, <https://doi.org/10.5194/gmd-13-3571-2020>, 2020.

Mex, J., Cassou, C., Jézéquel, A., Dese, C.: Physical understanding of the extreme global temperature jump in 2023. *Commun Earth Environ* 7, 406. <https://doi.org/10.1038/s43247-026-03382-6>, 2026

Millán, L., Santee, M. L., Lambert, A., Livesey, N. J., Werner, F., Schwartz, M. J., Pumphrey, H. C., Manney, G. L., Wang, Y., Su, H., Wu, L., Read, W. G., and Froidevaux, L.: The Hunga Tonga-Hunga Ha'apai Hydration of the Stratosphere, *Geophys. Res. Lett.*, 49, e2022GL099381, <https://doi.org/10.1029/2022GL099381>, 2022.

Millar, R. J., Nicholls, Z. R., Friedlingstein, P., and Allen, M. R.: A modified impulse-response representation of the global near-surface air temperature and atmospheric concentration response to carbon dioxide emissions, *Atmos. Chem. Phys.*, 17, 7213–7228, <https://doi.org/10.5194/acp-17-7213-2017>, 2017.

Minobe, S., Behrens, E., Findell, K. L., Loeb, N. G., Meyssignac, B., and Sutton, R.: Global and regional drivers for exceptional climate extremes in 2023-2024: beyond the new normal, *npj Clim Atmos Sci*, 8, 138, <https://doi.org/10.1038/s41612-025-00996-z>, 2025.

Minx, J. C., Lamb, W. F., Andrew, R. M., Canadell, J. G., Crippa, M., Döbbeling, N., Forster, P. M., Guizzardi, D., Olivier, J., Peters, G. P., Pongratz, J., Reisinger, A., Rigby, M., Saunio, M., Smith, S. J., Solazzo, E., and Tian, H.: A comprehensive and synthetic dataset for global, regional, and national greenhouse gas emissions by sector 1970–2018 with an extension to 2019, *Earth Syst. Sci. Data*, 13, 5213–5252, <https://doi.org/10.5194/essd-13-5213-2021>, 2021.

Morice, C. P., Kennedy, J. J., Rayner, N. A., Winn, J. P., Hogan, E., Killick, R. E., Dunn, R. J. H., Osborn, T. J., Jones, P. D., and Simpson, I. R.: An Updated Assessment of Near-Surface Temperature Change From 1850: The HadCRUT5 Data Set, *J. Geophys. Res.-Atmos.*, 126, e2019JD032361, <https://doi.org/10.1029/2019JD032361>, 2021.

Myhre, G., Samset, B. H., Schulz, M., Balkanski, Y., Bauer, S., Berntsen, T. K., Bian, H., Bellouin, N., Chin, M., Diehl, T., Easter, R. C., Feichter, J., Ghan, S. J., Hauglustaine, D., Iversen, T., Kinne, S., Kirkevåg, A., Lamarque, J.-F., Lin, G., Liu, X., Lund, M. T., Luo, G., Ma, X., van Noije, T., Penner, J. E., Rasch, P. J., Ruiz, A., Seland, Ø., Skeie, R. B., Stier, P., Takemura, T., Tsigaridis, K., Wang, P., Wang, Z., Xu, L., Yu, H., Yu, F., Yoon, J.-H., Zhang, K., Zhang, H., and Zhou, C.: Radiative forcing of the direct aerosol effect from AeroCom Phase II simulations, *Atmos. Chem. Phys.*, 13, 1853–1877, <https://doi.org/10.5194/acp-13-1853-2013>, 2013a.

Myhre, G., D. Shindell, F.-M. Bréon, W. Collins, J. Fuglestedt, J. Huang, D. Koch, J.-F. Lamarque, D. Lee, B. Mendoza, T. Nakajima, A. Robock, G. Stephens, T. Takemura and H. Zhang: Anthropogenic and Natural Radiative Forcing. In: *Climate Change 2013: The Physical Science Basis. Contribution of Working Group I to the Fifth Assessment Report of the Intergovernmental Panel on Climate Change*, edited by Stocker, T.F., D. Qin, G.-K. Plattner, M. Tignor, S.K. Allen, J. Boschung, A. Nauels, Y. Xia, V. Bex and P.M. Midgley (eds.)). Cambridge University Press, Cambridge, United Kingdom and New York, NY, USA, <https://doi.org/10.1017/CBO9781107415324.018>, 2013b.

Nicholls Z., Lewis J., Makin M., et al. Regionally aggregated, stitched and de-drifted CMIP-climate data, processed with netCDF-SCM v2.0.0. *Geosci Data J.*, 8, 154–198, <https://doi.org/10.1002/gdj3.113>, 2021.

Nitzbon, J., Krinner, G., Langer, M.: GCOS EHI 1960-2020 Permafrost Heat Content, World Data Center for Climate (WDCC) at DKRZ, [https://doi.org/10.26050/WDCC/GCOS\\_EHI\\_1960-2020\\_PHC](https://doi.org/10.26050/WDCC/GCOS_EHI_1960-2020_PHC), 2022.

Otto, F. E. L., Frame, D. J., Otto, A., and Allen, M. R.: Embracing uncertainty in climate change policy, *Nature Clim. Chang.*, 5, 917–920, <https://doi.org/10.1038/nclimate2716>, 2015.

Ouyang, Z., Sciusco, P., Jiao, T., Feron, S., Lei, C., Li, F., John, R., Fan, P., Li, X., Williams, C.A., Chen, G., Wang, C., Chen, J. : Albedo changes caused by future urbanization contribute to global warming. *Nat Commun* 13, 3800. <https://doi.org/10.1038/s41467-022-31558-z>, 2022

Palmer, M. D., Domingues, C. M., Slangen, A. B. A., and Dias, F. B.: An ensemble approach to quantify global mean sea-level rise over the 20th century from tide gauge reconstructions, *Environ. Res. Lett.*, 16, 044043, <https://doi.org/10.1088/1748-9326/abdaec>, 2021.

Purich, A., Doddridge, E.W.: Record low Antarctic sea ice coverage indicates a new sea ice state. *Commun Earth Environ* 4, 314, <https://doi.org/10.1038/s43247-023-00961-9>, 2023

Purkey, S.G. and Johnson, G.C., Warming of Global Abyssal and Deep Southern Ocean Waters between the 1990s and 2000s: Contributions to Global Heat and Sea Level Rise Budgets, *J. Climate*, 23, 6336–6351, <https://doi.org/10.1175/2010JCLI3682.1>, 2010.

Prinn, R. G., Weiss, R. F., Arduini, J., Arnold, T., DeWitt, H. L., Fraser, P. J., Ganesan, A. L., Gasore, J., Harth, C. M., Hermansen, O., Kim, J., Krummel, P. B., Li, S., Loh, Z. M., Lunder, C. R., Maione, M., Manning, A. J., Miller, B. R., Mitrevski, B., Mühle, J., O'Doherty, S., Park, S., Reimann, S., Rigby, M., Saito, T., Salameh, P. K., Schmidt, R., Simmonds, P. G., Steele, L. P., Vollmer, M. K., Wang, R. H., Yao, B., Yokouchi, Y., Young, D., and Zhou, L.: History of chemically and radiatively important atmospheric gases from the Advanced Global Atmospheric Gases Experiment (AGAGE), *Earth Syst. Sci. Data*, 10, 985–1018, <https://doi.org/10.5194/essd-10-985-2018>, 2018.

Qasmi, S. and Ribes, A.: Reducing uncertainty in local temperature projections, *Sci. Adv.*, 8, eabo6872, <https://doi.org/10.1126/sciadv.abo6872>, 2022

Quaglia, I. and Visioni, D.: Modeling 2020 regulatory changes in international shipping emissions helps explain anomalous 2023 warming, *Earth Syst. Dynam.*, 15, 1527–1541, <https://doi.org/10.5194/esd-15-1527-2024>, 2024.

Raghuraman, S. P., Soden, B., Clement, A., Vecchi, G., Menemenlis, S., and Yang, W.: The 2023 global warming spike was driven by the El Niño–Southern Oscillation, *Atmos. Chem. Phys.*, 24, 11275–11283, <https://doi.org/10.5194/acp-24-11275-2024>, 2024.

Rantanen, M., Laaksonen, A.: Sherwood The jump in global temperatures in September 2023 is extremely unlikely due to internal climate variability alone. *npj Clim Atmos Sci* 7, 34. <https://doi.org/10.1038/s41612-024-00582-9>, 2024

Riahi, K., Schaeffer, J. Arango, K. Calvin, C. Guivarch, T. Hasegawa, K. Jiang, E. Kriegler, R. Matthews, G.P. Peters, A. Rao, S. Robertson, A.M. Sebbit, J. Steinberger, M. Tavoni, D.P. van Vuuren, 2022: Mitigation pathways compatible with long-term goals. In IPCC, 2022: Climate Change 2022: Mitigation of Climate Change. Contribution of Working Group III to the Sixth Assessment Report of the Intergovernmental Panel on Climate Change [P.R. Shukla, J. Skea, R. Slade, A. Al Khourdajie, R. van Diemen, D. McCollum, M. Pathak, S. Some, P. Vyas, R. Fradera, M. Belkacemi, A. Hasija, G. Lisboa, S. Luz, J. Malley, (eds.)]. Cambridge University Press, Cambridge, UK and New York, NY, USA, <https://doi.org/10.1017/9781009157926.005>, 2022.

Ribes, A., Planton, S., and Terray, L.: Application of regularised optimal fingerprinting to attribution. Part I: method, properties and idealised analysis, *Clim. Dyn.*, 41, 2817–2836, <https://doi.org/10.1007/s00382-013-1735-7>, 2013.

Ribes, A., Qasmi, S., and Gillett, N. P.: Making climate projections conditional on historical observations, *Sci. Adv.*, 7, eabc0671, <https://doi.org/10.1126/sciadv.abc0671>, 2021.

Richardson, M., Cowtan, K., and Millar, R. J.: Global temperature definition affects achievement of long-term climate goals, *Environ. Res. Lett.*, 13, 054004, <https://doi.org/10.1088/1748-9326/aab305>, 2018.

Rogelj, J., Schaeffer, M., Meinshausen, M., Shindell, D. T., Hare, W., Klimont, Z., Velders, G. J., Amann, M., and Schellnhuber, H. J.: Disentangling the effects of CO<sub>2</sub> and short-lived climate forcer mitigation, *Proc. Natl. Acad. Sci. USA*, 111 (46), 16325–16330, <https://doi.org/10.1073/pnas.1415631111>, 2014a.

Rogelj, J., D. Shindell, K. Jiang, S. Fifita, P. Forster, V. Ginzburg, C. Handa, H. Kheshgi, S. Kobayashi, E. Kriegler, L. Mundaca, R. Séférian, and M. V. Vilariño: Mitigation Pathways Compatible with 1.5°C in the Context of Sustainable Development. In: Global Warming of 1.5°C. An IPCC Special Report on the impacts of global warming of 1.5°C above pre-industrial levels and related global greenhouse gas emission pathways, in the context of strengthening the global response to the threat of climate change, sustainable development, and efforts to eradicate poverty [Masson-Delmotte, V., P. Zhai, H.-O. Pörtner, D. Roberts, J. Skea, P.R. Shukla, A. Pirani, W. Moufouma-Okia, C. Péan, R. Pidcock, S. Connors, J. B. R. Matthews, Y. Chen, X. Zhou, M. I. Gomis, E. Lonnoy, T. Maycock, M. Tignor, and T. Waterfield (eds.)]. Cambridge University Press, Cambridge, UK and New York, NY, USA, pp. 93-174, <https://doi.org/10.1017/9781009157940.004>, 2018.

Rogelj, J., Rao, S., McCollum, D. L., Pachauri, S., Klimont, Z., Krey, V., and Riahi, K: Air-pollution emission ranges consistent with the representative concentration pathways, *Nature Clim. Chang.*, 4 (6), 446–450, <https://doi.org/10.1038/nclimate2178>, 2014b.

Rogelj, J., Lamboll, R.D.: Substantial reductions in non-CO<sub>2</sub> greenhouse gas emissions reductions implied by IPCC estimates of the remaining carbon budget. *Communications Earth Environ* 5, 35. <https://doi.org/10.1038/s43247-023-01168-8>, 2024.

Rohde, R., Muller, R., Jacobsen, R., Perlmutter, S., Rosenfeld, A., Wurtele, J., Curry, J., Wickham, C., and Mosher, S.: Berkeley Earth temperature averaging process, *Geoinfor. Geostat.: An Overview*, 1, <https://doi.org/10.4172/2327-4581.1000103>, 2013.

Rohde, R. A. and Hausfather, Z.: The Berkeley Earth Land/Ocean Temperature Record, *Earth Syst. Sci. Data*, 12, 3469–3479, <https://doi.org/10.5194/essd-12-3469-2020>, 2020.

Schoeberl, M. R., Wang, Y., Taha, G., Zawada, D. J., Ueyama, R., and Dessler, A.: Evolution of the Climate Forcing During the Two Years After the Hunga Tonga-Hunga Ha’apai Eruption, *JGR Atmospheres*, 129, e2024JD041296, <https://doi.org/10.1029/2024JD041296>, 2024.

Sellitto, P., Podglajen, A., Belhadji, R., Boichu, M., Carboni, E., Cuesta, J., Duchamp, C., Kloss, C., Siddans, R., Bègue, N., Blarel, L., Jegou, F., Khaykin, S., Renard, J.B., Legras, B.: The unexpected radiative impact of the Hunga Tonga eruption of 15th January 2022, *Commun. Earth. Environ.*, 3, 288, <https://doi.org/10.1038/s43247-022-00618-z>, 2022.

Seneviratne, S.I., X. Zhang, M. Adnan, W. Badi, C. Dereczynski, A. Di Luca, S. Ghosh, I. Iskandar, J. Kossin, S. Lewis, F. Otto, I. Pinto, M. Satoh, S. M. Vicente-Serrano, M. Wehner, and B. Zhou: Weather and Climate Extreme Events in a Changing Climate. In *Climate Change 2021: The Physical Science Basis. Contribution of Working Group I to the Sixth Assessment Report of the Intergovernmental Panel on Climate Change* [Masson-Delmotte, V., P. Zhai, A. Pirani, S.L. Connors, C. Péan, S. Berger, N. Caud, Y. Chen, L. Goldfarb, M.I. Gomis, M. Huang, K. Leitzell, E. Lonnoy, J.B.R. Matthews, T.K. Maycock, T. Waterfield, O. Yelekçi, R. Yu, and B. Zhou (eds.)]. Cambridge University Press, Cambridge, United Kingdom and New York, NY, USA, pp. 1513–1766, doi:10.1017/9781009157896.013.1513–1766, <https://doi.org/10.1017/9781009157896.013>, 2021.

von Schuckmann, K., Cheng, L., Palmer, M. D., Hansen, J., Tassone, C., Aich, V., Adusumilli, S., Beltrami, H., Boyer, T., Cuesta-Valero, F. J., Desbruyères, D., Domingues, C., García-García, A., Gentine, P., Gilson, J., Gorfer, M., Haimberger, L., Ishii, M., Johnson, G. C., Killick, R., King, B. A., Kirchengast, G., Kolodziejczyk, N., Lyman, J., Marzeion, B., Mayer, M., Monier, M., Monselesan, D. P., Purkey, S., Roemmich, D., Schweiger, A., Seneviratne, S. I., Shepherd, A., Slater, D. A., Steiner, A. K., Straneo, F., Timmermans, M.-L., and Wijffels, S. E.: Heat stored in the Earth system: where does the energy go?, *Earth Syst. Sci. Data*, 12, 2013–2041, <https://doi.org/10.5194/essd-12-2013-2020>, 2020.

von Schuckmann, K., Minière, A., Gues, F., Cuesta-Valero, F. J., Kirchengast, G., Adusumilli, S., Straneo, F., Ablain, M., Allan, R. P., Barker, P. M., Beltrami, H., Blazquez, A., Boyer, T., Cheng, L., Church, J., Desbruyeres, D., Dolman, H., Domingues, C. M., García-García, A., Giglio, D., Gilson, J. E., Gorfer, M., Haimberger, L., Hakuba, M. Z., Hendricks, S., Hosoda, S., Johnson, G. C., Killick, R., King, B., Kolodziejczyk, N., Korosov, A., Krinner, G., Kuusela, M., Landerer, F. W., Langer, M., Lavergne, T., Lawrence, I., Li, Y., Lyman, J., Marti, F., Marzeion, B., Mayer, M., MacDougall, A. H., MacDougall, T., Monselesan, D. P., Nitzbon, J., Otsuka, I., Peng, J., Purkey, S., Roemmich, D., Sato, K., Sato, K., Savita, A., Schweiger, A., Shepherd, A., Seneviratne, S. I., Simons, L., Slater, D. A., Slater, T., Steiner, A. K., Suga, T., Szekely, T., Thiery, W., Timmermans, M.-L., Vanderkelen, I., Wjiffels, S. E., Wu, T., and Zemp, M.: Heat stored in the Earth system 1960–2020: where does the energy go?, *Earth System Science Data*, 15, 1675–1709, <https://doi.org/10.5194/essd-15-1675-2023>, 2023.

Sherwood, S. C., Dixit, V., Salomez, C.: The global warming potential of near-surface emitted water vapour, *Environ. Res. Lett.*, 13, 104006, [doi.org/10.1088/1748-9326/aae018](https://doi.org/10.1088/1748-9326/aae018), 2018.

Shine, K.P., Derwent, R.G., Wuebbles, D.J., and Morcrette, J.-J.: Radiative Forcing of Climate. In *Climate Change: The IPCC Scientific Assessment* (1990), J.T. Houghton, G.J. Jenkins and J.J. Ephraums (eds.). Cambridge University Press, Cambridge, Great Britain, New York, NY, USA and Melbourne, Australia, 1990.

Sigl, M., Toohey, M., McConnell, J. R., Cole-Dai, J., and Severi, M.: Volcanic stratospheric sulfur injections and aerosol optical depth during the Holocene (past 11,500 years) from a bipolar ice-core array, *Earth Syst. Sci. Data*, 14, 3167–3196, <https://doi.org/10.5194/essd-14-3167-2022>, 2022.

Skeie, R. B., Myhre, G., Hodnebrog, Ø., Cameron-Smith, P. J., Deushi, M., Hegglin, M. I., Horowitz, L. W., Kramer, R. J., Michou, M., Mills, M. J., Olivié, D. J. L., Connor, F. M. O., Paynter, D., Samset, B. H., Sellar, A., Shindell, D., Takemura, T., Tilmes, S., and Wu, T.: Historical total ozone radiative forcing derived from CMIP6 simulations, *npj Clim. Atmos. Sci.*, 3, 32, <https://doi.org/10.1038/s41612-020-00131-0>, 2020.

Skeie, R. B., Byrom, R., Hodnebrog, Ø., Jouan, C., and Myhre, G.: Multi-model effective radiative forcing of the 2020 sulfur cap for shipping, *Atmos. Chem. Phys.*, 24, 13361–13370, <https://doi.org/10.5194/acp-24-13361-2024>, 2024.

Smith, C. J., Kramer, R. J., Myhre, G., Forster, P. M., Soden, B. J., Andrews, T., Boucher, O., Faluvegi, G., Fläschner, D., Hodnebrog, Ø., Kasoar, M., Kharin, V., Kirkevåg, A., Lamarque, J.-F., Mülmenstädt, J., Olivié, D., Richardson, T., Samset, B. H., Shindell, D., Stier, P., Takemura, T., Voulgarakis, A., and Watson-Parris, D.: Understanding Rapid Adjustments to Diverse Forcing Agents, *Geophys. Res. Lett.*, 45, 12,023–12,031, <https://doi.org/10.1029/2018GL079826>, 2018a.

Smith, C. J., Forster, P. M., Allen, M., Leach, N., Millar, R. J., Passerello, G. A., and Regayre, L. A.: FAIR v1.3: A simple emissions-based impulse response and carbon cycle model, *Geoscientific Model Development*, 11, 2273–2297, <https://doi.org/10.5194/gmd-11-2273-2018>, 2018b.

Smith, C. J., Harris, G. R., Palmer, M. D., Bellouin, N., Collins, W., Myhre, G., Schulz, M., Golaz, J.-C., Ringer, M., Storelvmo, T., and Forster, P. M.: Energy Budget Constraints on the Time History of Aerosol Forcing and Climate Sensitivity, *Journal of Geophysical Research: Atmospheres*, 126, e2020JD033622, <https://doi.org/10.1029/2020JD033622>, 2021a.

Smith, C., Nicholls, Z. R. J., Armour, K., Collins, W., Forster, P., Meinshausen, M., Palmer, M. D., and Watanabe, M.: The Earth's Energy Budget, Climate Feedbacks, and Climate Sensitivity Supplementary Material, in: *Climate Change 2021: The Physical Science Basis. Contribution of Working Group I to the Sixth Assessment Report of the Intergovernmental Panel on Climate Change*, edited by: Masson-Delmotte, V., Zhai, P., Pirani, A., Connors, S. L., Péan, C., Berger, S., Caud, N., Chen, Y., Goldfarb, L., Gomis, M. I., Huang, M., Leitzell, K., Lonnoy, E., Matthews, J. B. R., Maycock, T. K., Waterfield, T., Yelekçi, O., Yu, R., and Zhou, B., 2021b.

Smith, C., Cummins, D. P., Fredriksen, H.-B., Nicholls, Z., Meinshausen, M., Allen, M., Jenkins, S., Leach, N., Mathison, C., and Partanen, A.-I.: fair-calibrate v1.4.1: calibration, constraining, and validation of the FaIR simple climate model for reliable future climate projections, *Geosci. Model Dev.*, 17, 8569–8592, <https://doi.org/10.5194/gmd-17-8569-2024>, 2024.

Stevenson, D. S., Young, P. J., Naik, V., Lamarque, J.-F., Shindell, D. T., Voulgarakis, A., Skeie, R. B., Dalsoren, S. B., Myhre, G., Berntsen, T. K., Folberth, G. A., Rumbold, S. T., Collins, W. J., MacKenzie, I. A., Doherty, R. M., Zeng, G., van Noije, T. P. C., Strunk, A., Bergmann, D., Cameron-Smith, P., Plummer, D. A., Strode, S. A., Horowitz, L., Lee, Y. H., Szopa, S., Sudo, K., Nagashima, T., Josse, B., Cionni, I., Righi, M., Eyring, V., Conley, A., Bowman, K. W., Wild, O., and Archibald, A.: Tropospheric ozone changes, radiative forcing and attribution to emissions in the Atmospheric Chemistry and Climate Model Intercomparison Project (ACCMIP), *Atmos. Chem. Phys.*, 13, 3063–3085, <https://doi.org/10.5194/acp-13-3063-2013>, 2013.

Souza, C. M., Jr., Z. Shimbo, J., Rosa, M. R., Parente, L. L., A. Alencar, A., Rudorff, B. F. T., Hasenack, H., Matsumoto, M., G. Ferreira, L., Souza-Filho, P. W. M., de Oliveira, S. W., Rocha, W. F., Fonseca, A. V., Marques, C. B., Diniz, C. G., Costa, D., Monteiro, D., Rosa, E. R., Vélez-Martin, E., ... Azevedo, T. (2020). Reconstructing Three Decades of Land Use and Land Cover Changes in Brazilian Biomes with Landsat Archive and Earth Engine. *Remote Sensing*, 12(17), 2735. <https://doi.org/10.3390/rs12172735>, 2020

Steiner, A. K., Ladstädter, F., Randel, W. J., Maycock, A. C., Fu, Q., Claud, C., Gleisner, H., Haimberger, L., Ho, S.-P., Keckhut, P., Leblanc, T., Mears, C., Polvani, L. M., Santer, B. D., Schmidt, T., Sofieva, V., Wing, R., and Zou, C.-Z.:

Observed Temperature Changes in the Troposphere and Stratosphere from 1979 to 2018, *J. Climate*, 33, 8165–8194, <https://doi.org/10.1175/JCLI-D-19-0998.1>, 2020.

Sun, W., Li, Q., Huang, B., Cheng, J., Song, Z., Li, H., Dong, W., Zhai, P., and Jones, P.: The Assessment of Global Surface Temperature Change from 1850s: The C-LSAT2.0 Ensemble and the CMST-Interim Datasets, *Advances in Atmospheric Sciences*, 38, 875–888, <https://doi.org/10.1007/s00376-021-1012-3>, 2021.

Szopa, S., V. Naik, B. Adhikary, P. Artaxo, T. Berntsen, W.D. Collins, S. Fuzzi, L. Gallardo, A. Kiendler-Scharr, Z. Klimont, H. Liao, N. Unger, and P. Zanis: Short-Lived Climate Forcers. In *Climate Change 2021: The Physical Science Basis. Contribution of Working Group I to the Sixth Assessment Report of the Intergovernmental Panel on Climate Change* [Masson-Delmotte, V., P. Zhai, A. Pirani, S.L. Connors, C. Péan, S. Berger, N. Caud, Y. Chen, L. Goldfarb, M.I. Gomis, M. Huang, K. Leitzell, E. Lonnoy, J.B.R. Matthews, T.K. Maycock, T. Waterfield, O. Yelekçi, R. Yu, and B. Zhou (eds.)]. Cambridge University Press, Cambridge, United Kingdom and New York, NY, USA, pp. 817–922, <https://doi:10.1017/9781009157896.008>, 2021.

Taha, G., Loughman, R., Zhu, T., Thomason, L., Kar, J., Rieger, L., and Bourassa, A.: OMPS LP Version 2.0 multi-wavelength aerosol extinction coefficient retrieval algorithm, *Atmos. Meas. Tech.*, 14, 1015–1036, <https://doi.org/10.5194/amt-14-1015-2021>, 2021.

Taylor, K. E., Crucifix, M., Braconnot, P., Hewitt, C. D., Doutriaux, C., Broccoli, A. J., Mitchell, J. F. B., and Webb, M. J.: Estimating Shortwave Radiative Forcing and Response in Climate Models, *J. Climate*, 20, 2530–2543, <https://doi.org/10.1175/JCLI4143.1>, 2007.

Terhaar, J., Burger, F.A., Vogt, L. et al.: Record sea surface temperature jump in 2023–2024 unlikely but not unexpected, *Nature* 639, 942–946, <https://doi.org/10.1038/s41586-025-08674-z>, 2025.

Thomason, L. W., Ernest, N., Millán, L., Rieger, L., Bourassa, A., Vernier, J.-P., Manney, G., Luo, B., Arfeuille, F., and Peter, T.: A global space-based stratospheric aerosol climatology: 1979–2016, *Earth Syst. Sci. Dat.*, 10, 469–492, <https://doi.org/10.5194/essd-10-469-2018>, 2018.

Thorne, P. W., Nicklas, J. M., Kennedy, J. J., Calvert, B., Fox-Kemper, B., Richardson, M. T., Simmons, A., Hawkins, E., Rhode, R., Cowtan, K., Abram, N. J., Andersson, A., Noone, S., Marbaix, P., Lenssen, N., Olonscheck, D., Walsh, T., Outten, S., Bethke, I., Samset, B. H., Smith, C., Pirani, A., Fuglested, J., Rajamani, L., Betts, R. A., Kent, E. C., Trewin, B., Morice, C., Osborn, T., Burgess, S. N., Geden, O., Parnell, A., Forster, P. M., Hewitt, C., Hausfather, Z., Masson-Delmotte, V., Marotzke, J., Gillett, N., Seneviratne, S. I., Schmidt, G. A., Chan, D., Brönnimann, S., Reisinger, A., Menne, M., Rojas Corradi, M., Kadow, C., Huybers, P., Stephenson, D. B., Wallis, E., Rogelj, J., Schurer, A., McKinnon, K., Zhai, P., Driouech, F., Moufouma Okia, W., Vazifekhhah, S., Szopa, S., Merchant, C. J., Hirahara, S., Ishii, M., Engelbrecht,

F. A., Li, Q., Lee, J.-Y., Cannon, A. J., Cassou, C., Von Schuckmann, K., Delju, A. H., and Murtagh, E.: How well can we quantify when 1.5 °C of global warming has been exceeded?, <https://doi.org/10.5194/essd-2025-825>, 28 January 2026.

Thornhill, G. D., Collins, W. J., Kramer, R. J., Olivie, D., Skeie, R. B., O'Connor, F. M., Abraham, N. L., Checa-Garcia, R., Bauer, S. E., Deushi, M., Emmons, L. K., Forster, P. M., Horowitz, L. W., Johnson, B., Keeble, J., Lamarque, J.-F., Michou, M., Mills, M. J., Mulcahy, J. P., Myhre, G., Nabat, P., Naik, V., Oshima, N., Schulz, M., Smith, C. J., Takemura, T., Tilmes, S., Wu, T., Zeng, G., and Zhang, J.: Effective radiative forcing from emissions of reactive gases and aerosols – a multi-model comparison, *Atmos. Chem. Phys.*, 21, 853–874, <https://doi.org/10.5194/acp-21-853-2021>, 2021a.

Thornhill, G., Collins, W., Olivie, D., Skeie, R. B., Archibald, A., Bauer, S., Checa-Garcia, R., Fiedler, S., Folberth, G., Gjermundsen, A., Horowitz, L., Lamarque, J.-F., Michou, M., Mulcahy, J., Nabat, P., Naik, V., O'Connor, F. M., Paulot, F., Schulz, M., Scott, C. E., Séférian, R., Smith, C., Takemura, T., Tilmes, S., Tsigaridis, K., and Weber, J.: Climate-driven chemistry and aerosol feedbacks in CMIP6 Earth system models, *Atmos. Chem. Phys.*, 21, 1105–1126, <https://doi.org/10.5194/acp-21-1105-2021>, 2021b.

Toohey, M. and Sigl, M.: Volcanic stratospheric sulfur injections and aerosol optical depth from 500\,BCE to 1900\,CE, *Earth Syst. Sci. Data*, 9, 809–831, <https://doi.org/10.5194/essd-9-809-2017>, 2017.

Trewin, B., Cazenave, A., Howell, S., Huss, M., Isensee, K., Palmer, M. D., Tarasova, O., and Vermeulen, A.: *Headline Indicators for Global Climate Monitoring*, *Bulletin of the American Meteorological Society*, 102, E20–E37, <https://doi.org/10.1175/BAMS-D-19-0196.1>, 2021.

Trewin, B.: Assessing Internal Variability of Global Mean Surface Temperature From Observational Data and Implications for Reaching Key Thresholds, *JGR Atmospheres*, 127, e2022JD036747, <https://doi.org/10.1029/2022JD036747>, 2022.

Tselioudis, G., W.B. Rossow, F. Bender, L. Oreopoulos, and J. Rémillard: Oceanic cloud trends during the satellite era and their radiative signatures. *Clim. Dyn.*, 62, no. 9, 9319-9332, doi:10.1007/s00382-024-07396-8, 2024

Vanderkelen, I., van Lipzig, N. P. M., Lawrence, D. M., Droppers, B., Golub, M., Gosling, S. N., Janssen, A. B. G., Marcé, R., Schmied, H. M., Perroud, M., Pierson, D., Pokhrel, Y., Satoh, Y., Schewe, J., Seneviratne, S. I., Stepanenko, V. M., Tan, Z., Woolway, R. I., and Thiery, W.: Global Heat Uptake by Inland Waters, *Geophysical Research Letters*, 47, e2020GL087867, <https://doi.org/10.1029/2020GL087867>, 2020.

Vose, R. S., Huang, B., Yin, X., Arndt, D., Easterling, D. R., Lawrimore, J. H., Menne, M. J., Sanchez-Lugo, A., and Zhang, H. M.: Implementing Full Spatial Coverage in NOAA's Global Temperature Analysis, *Geophys. Res. Lett.*, 48, e2020GL090873, <https://doi.org/10.1029/2020GL090873>, 2021.

Watson-Parris, D., Christensen, M. W., Laurenson, A., Clewley, D., Gryspeerdt, E., and Stier, P.: Shipping regulations lead to large reduction in cloud perturbations, *Proc. Natl. Acad. Sci. U.S.A.*, 119, e2206885119, <https://doi.org/10.1073/pnas.2206885119>, 2022.

Watson-Parris, D., Wilcox, L. J., Stjern, C. W., Allen, R. J., Persad, G., Bollasina, M. A., Ekman, A. M. L., Iles, C. E., Joshi, M., Lund, M. T., McCoy, D., Westervelt, D., Williams, A., and Samset, B. H.: Weak surface temperature effects of recent reductions in shipping SO<sub>2</sub> emissions, with quantification confounded by internal variability, *EGUsphere* [preprint], <https://doi.org/10.5194/egusphere-2024-1946>, 2024.

van der Werf, G. R., Randerson, J. T., Giglio, L., van Leeuwen, T. T., Chen, Y., Rogers, B. M., Mu, M., van Marle, M. J. E., Morton, D. C., Collatz, G. J., Yokelson, R. J., and Kasibhatla, P. S.: Global fire emissions estimates during 1997–2016, *Earth System Science Data*, 9, 697–720, <https://doi.org/10.5194/essd-9-697-2017>, 2017.

van der Werf, G.R., Randerson, J.T., van Wees, D. et al. Landscape fire emissions from the 5th version of the Global Fire Emissions Database (GFED5). *Sci Data* 12, 1870, <https://doi-org.insu.bib.cnrs.fr/10.1038/s41597-025-06127-w>, 2025.

Wild, O., Prather, M. J., and Akimoto, H.: Indirect long-term global radiative cooling from NO<sub>x</sub> emissions, *Geophys. Res. Lett.*, 28, 1719–1722, <https://doi.org/10.1029/2000GL012573>, 2001.

World Meteorological Organization (WMO), 2025. State of the Global Climate 2024. WMO-No. 1368. World Meteorological Organization, <https://library.wmo.int/idurl/4/69455>, accessed 27 April 2025, 2025.

World Meteorological Organization (WMO): State of the Global Climate 2025. WMO-No. 1342. Geneva, <https://doi.org/10.59327/WMO/S/CRI/SOCL>, 2026.

Xu, Q., Wei, S., Li, Z., and Li, Q.: A New Evaluation of Observed Changes in Diurnal Temperature Range, *Geophysical Research Letters*, 52, e2024GL113406, <https://doi.org/10.1029/2024GL113406>, 2025.

Yao, Y., Ducharne, A., Cook, B. I., De Hertog, S. J., Schanke Aas, K., Arboleda-Obando, P. F., Buzan, J., Colin, J., Costantini, M., Decharme, B., Lawrence, D. M., Lawrence, P., Leung, L. R., Lo, M.-H., Devaraju, N., Wieder, W. R., Wu, R.-J., Zhou, T., Jägermeyr, J., McDermid, S., Pokhrel, Y., Elling, M., Hanasaki, N., Muñoz, P., Nazarenko, L. S., Otta, K., Satoh, Y., Yokohata, T., Jin, L., Wang, X., Mishra, V., Ghosh, S., and Thiery, W.: Impacts of irrigation expansion on moist-heat stress based on IRRMIP results. *Nat Commun* 16, 1045, <https://doi.org/10.1038/s41467-025-56356-1>, 2025.

Yin, X., Huang, B., Menne, M., Vose, R., Zhang, H.-M., Adeyeye, A., Applequist, S., Gleason, K., Liu, C., and Sanchez-Lugo, A.: NOAA GlobalTemp Version 6: An AI-Based Global Surface Temperature Dataset, *Bulletin of the American Meteorological Society*, 105, E2184–E2193, <https://doi.org/10.1175/BAMS-D-24-0012.1>, 2024.

Yoshioka, M., Grosvenor, D. P., Booth, B. B. B., Morice, C. P., and Carslaw, K. S.: Warming effects of reduced sulfur emissions from shipping, *Atmos. Chem. Phys.*, 24, 13681–13692, <https://doi.org/10.5194/acp-24-13681-2024>, 2024.

Yuan, T., Song, H., Wood, R., Wang, C., Oreopoulos, L., Platnick, S. E., Von Hippel, S., Meyer, K., Light, S., and Wilcox, E.: Global reduction in ship-tracks from sulfur regulations for shipping fuel, *Sci. Adv.*, 8, eabn7988, <https://doi.org/10.1126/sciadv.abn7988>, 2022.

Yuan, T., Song, H., Oreopoulos, L., Wood, R., Bian, H., Breen, K., Chin, M., Yu, H., Barahona, D., Meyer, K., Platnick, S. : Abrupt reduction in shipping emission as an inadvertent geoengineering termination shock produces substantial radiative warming. *Commun Earth Environ* 5, 281. <https://doi.org/10.1038/s43247-024-01442-3>, 2024

Zelinka, M. D., Andrews, T., Forster, P. M., and Taylor, K. E.: Quantifying components of aerosol-cloud-radiation interactions in climate models, *J. Geophys. Res.-Atmos.*, 119, 7599–7615, <https://doi.org/10.1002/2014JD021710>, 2014.

Zelinka, M. D., Smith, C. J., Qin, Y., and Taylor, K. E.: Aerosol Effective Radiative Forcings in CMIP Models, *EGUsphere*, <https://acp.copernicus.org/articles/23/8879/2023>, 2023.